

# **Doctoral Dissertation**

## **Tracking atmospheric chemical components in accordance with the Sustainable Development Goals (SDGs)**

Phan Anh

November 21, 2023

Graduate School of Engineering  
Chubu University

A Doctoral Dissertation  
submitted to Graduate School of Engineering,  
Chubu University  
in partial fulfillment of the requirements for the degree of  
Doctor of ENGINEERING

Phan Anh

Thesis Committee:

Professor Hiromichi Fukui (Supervisor)  
Professor Kiyoshi Honda (Chubu University)  
Professor Jun Izutsu (Chubu University)  
Professor Masao Takano (Nagoya University)

# **Tracking atmospheric chemical components in accordance with the Sustainable Development Goals (SDGs)\***

Phan Anh

## **Abstract**

Lorem ipsum dolor sit amet, consectetur adipisicing elit, sed do eiusmod tempor incididunt ut labore et dolore magna aliqua. Ut enim ad minim veniam, quis nostrud exercitation ullamco laboris nisi ut aliquip ex ea commodo consequat. Duis aute irure dolor in reprehenderit in voluptate velit esse cillum dolore eu fugiat nulla pariatur. Excepteur sint occaecat cupidatat non proident, sunt in culpa qui officia deserunt mollit anim id est laborum.

Lorem ipsum dolor sit amet, consectetur adipisicing elit, sed do eiusmod tempor incididunt ut labore et dolore magna aliqua. Ut enim ad minim veniam, quis nostrud exercitation ullamco laboris nisi ut aliquip ex ea commodo consequat. Duis aute irure dolor in reprehenderit in voluptate velit esse cillum dolore eu fugiat nulla pariatur. Excepteur sint occaecat cupidatat non proident, sunt in culpa qui officia deserunt mollit anim id est laborum.

## **Keywords:**

$\pi$ , astronomy, mathematics, computer, algorithm

---

\*Doctoral Dissertation, Graduate School of Information Science,  
Nara Institute of Science and Technology, November 21, 2023.

# Contents

<b>List of Figures</b>	<b>iii</b>
<b>List of Tables</b>	<b>iv</b>
<b>1 Introduction</b>	<b>1</b>
1.1 Background . . . . .	1
<b>2 Background</b>	<b>2</b>
2.1 Air pollution . . . . .	2
2.2 Greenhouse gas . . . . .	2
<b>AIR POLLUTION INDUCED BY INTERVENTION EVENTS</b>	<b>3</b>
<b>3 Ukraine's case study</b>	<b>4</b>
3.1 Introduction . . . . .	4
3.2 Data . . . . .	7
3.2.1 Selection of analysis periods . . . . .	7
3.2.2 TROPOMI NO <sub>2</sub> from Sentinel 5P . . . . .	8
3.2.3 Meteorological and surface NO <sub>2</sub> data . . . . .	11
3.2.4 Fire spots database and Ukraine crisis hub . . . . .	12
3.2.5 Population data . . . . .	13
3.3 Business-as-usual (BAU) modelling . . . . .	13
3.4 COVID-19 induced NO <sub>2</sub> changes . . . . .	17
3.4.1 Lockdown and pre-lockdown meteorological patterns . . . . .	18
3.4.2 NO <sub>2</sub> changes in populous Ukrainian cities . . . . .	18
3.5 NO <sub>2</sub> changes induced by the armed conflict . . . . .	23
3.5.1 S5P NO <sub>2</sub> level changes in conflict hotspots . . . . .	24
3.5.2 Changes of S5P NO <sub>2</sub> levels in other affected areas . . . . .	27

3.6 Conclusion . . . . .	32
<b>4 Japan's case study</b>	<b>35</b>
4.1 Introduction . . . . .	35
4.2 Data . . . . .	38
4.2.1 Study area . . . . .	38
4.2.2 Ground observation . . . . .	40
4.2.3 ERA5 reanalysis dataset . . . . .	40
4.2.4 Sentinel 5P TROPOMI . . . . .	41
4.2.5 Biogeochemical modelled CH <sub>4</sub> budget . . . . .	41
4.3 Method . . . . .	42
4.3.1 Business-as-usual (BAU) modelling . . . . .	42
4.3.2 Experiments design . . . . .	44
4.4 Results . . . . .	45
4.4.1 NO <sub>2</sub> level changes . . . . .	45
4.4.2 O <sub>3</sub> level changes . . . . .	47
4.4.3 CH <sub>4</sub> level changes . . . . .	52
4.5 Discussion . . . . .	56
4.5.1 Variations in spatial resolution of multisource data . . . . .	56
4.5.2 Limitations . . . . .	57
4.6 Conclusion . . . . .	57
<b>GREENHOUSE GAS ESTIMATION AND MONITORING</b>	<b>59</b>
<b>5 Plant functional types mapping</b>	<b>60</b>
5.1 Introduction . . . . .	60
5.2 Data . . . . .	61
5.2.1 Study area . . . . .	61
5.2.2 Data collection . . . . .	62
5.3 Methodology . . . . .	63
5.4 Experimental results . . . . .	69
5.5 Conclusion . . . . .	75
<b>6 Upscaling global carbon fluxes</b>	<b>76</b>
6.1 Background and summary . . . . .	76

6.2	Methods . . . . .	76
6.2.1	Input data . . . . .	76
6.2.2	Multivariate Time Series Transformer Framework . . . . .	78
6.2.3	Training setup . . . . .	79
6.2.4	Validation . . . . .	79
6.3	Data records . . . . .	81
6.4	Technical validation . . . . .	81
6.4.1	Validation with FLUXNET 2015 . . . . .	81
6.4.2	Validation with SIF . . . . .	86
6.4.3	Interannual variations between products . . . . .	86
6.5	Usage notes . . . . .	89
<b>7</b>	<b>CO<sub>2</sub> monitoring platform</b>	<b>91</b>
7.1	Introduction . . . . .	91
7.2	Method . . . . .	92
7.2.1	Data collection . . . . .	93
7.2.2	API development . . . . .	95
7.2.3	Web application . . . . .	98
7.3	Result and discussion . . . . .	99
7.3.1	Result . . . . .	99
7.3.2	Discussion . . . . .	102
<b>8</b>	<b>Conclusion</b>	<b>104</b>
<b>Bibliography</b>		<b>106</b>

# List of Figures

3.1	Monthly map of S5P NO <sub>2</sub> in Ukraine . . . . .	9
3.2	Monthly number of qualitfied S5P NO <sub>2</sub> observations in Ukraine . . . . .	10
3.3	Feature importance estimated using LightGBM split method. . . . .	14
3.4	Model performance evaluation . . . . .	15
3.5	Examples of OBS and BAU data in 2022 . . . . .	16
3.6	Meteorological variations during pre-lockdown and lockdown . . . . .	19
3.7	S5P NO <sub>2</sub> level changes for most populous cities . . . . .	21
3.8	Analyzed conflict hotspots using satellite and ACLED data . . . . .	25
3.9	NO <sub>2</sub> level changes estimates for conflict events . . . . .	26
3.10	OBS and BAU S5P NO <sub>2</sub> trends (2020-2022) in populous cities . . . . .	28
3.11	OBS and BAU S5P NO <sub>2</sub> trends (2020-2022) for selected CPPs . . . . .	31
4.1	Mobility changes for 6 prefectures in Japan . . . . .	37
4.2	Study area . . . . .	39
4.3	Model performance evaluation . . . . .	43
4.4	NO <sub>2</sub> reduction trends in 2020 . . . . .	46
4.5	NO <sub>2</sub> , O <sub>3</sub> , SR, T2M, FNR, and HCHO variations in 2020 . . . . .	49
4.6	2020 O <sub>3</sub> mean trends (4 MAs) . . . . .	50
4.7	NO <sub>2</sub> , CO and CH <sub>4</sub> , and HCHO variations in 2020 . . . . .	54
4.8	2020 CO and CH <sub>4</sub> mean trends (4 MAs) . . . . .	55
5.1	National forest in Ena city . . . . .	62
5.2	Study area and annotated data . . . . .	64
5.3	Workflow and the proposed CNN architecture . . . . .	66
5.4	Inferred forest map in Ena City . . . . .	70
5.5	Study area and annotated data . . . . .	71
5.6	Inferred forest age map in Ena City . . . . .	72

5.7	Inferred PFTs map in Ena City . . . . .	73
5.8	PFTs mapping in other regions . . . . .	74
6.1	Schematic workflow of our FluxFormer methodology . . . . .	77
6.2	Validation with FLUXNET 2015 . . . . .	82
6.3	Validation with FLUXNET 2015 . . . . .	83
6.4	Seasonality validation with FLUXNET 2015 . . . . .	85
6.5	Validation with SIF products . . . . .	87
6.6	Seasonality validation with FLUXNET 2015 . . . . .	88
6.7	Interannual variations: GPP (a) RECO (b) . . . . .	90
7.1	Platform architecture . . . . .	93
7.2	APIs interfaces Emission Tracker APIs (a) Zero Emission APIs (b)	98
7.3	Emission Tracker interfaces . . . . .	99
7.4	Drawdown tab interfaces . . . . .	101
7.5	Additional platform interfaces . . . . .	101
7.6	Comparison with other platforms . . . . .	102

# List of Tables

3.1	Model performance evaluation . . . . .	14
3.2	The hyperparameters used to develop the LightGBM model . . . . .	17
3.3	S5P NO <sub>2</sub> level changes estimates for most populous cities . . . . .	20
3.4	Comparison of NO <sub>2</sub> changes during 2020 and 2022 lockdown period	29
3.5	S5P NO <sub>2</sub> variations in populous cities from February to July 2022	30
4.1	Model performance evaluation . . . . .	44
4.2	short . . . . .	47
4.3	short . . . . .	50
4.4	short . . . . .	53
5.1	Samples, weights for cross-entropy loss training . . . . .	67
5.2	The experimental results of UNET and our model. . . . .	69
6.1	Number of samples for training and validation . . . . .	80
6.2	Pearson correlation of seasonal trend with FLUXNET 2015 . . . . .	84
7.1	The dataset used for the GIS platform development . . . . .	94
7.2	APIs specifications . . . . .	95

# 1 Introduction

## 1.1 Background

## **2 Background**

### **2.1 Air pollution**

### **2.2 Greenhouse gas**

  Lorem ipsum dolor sit amet, consectetur adipisicing elit, sed do eiusmod tempor incididunt ut labore et dolore magna aliqua. Ut enim ad minim veniam, quis nostrud exercitation ullamco laboris nisi ut aliquip ex ea commodo consequat. Duis aute irure dolor in reprehenderit in voluptate velit esse cillum dolore eu fugiat nulla pariatur. Excepteur sint occaecat cupidatat non proident, sunt in culpa qui officia deserunt mollit anim id est laborum.

# **AIR POLLUTION INDUCED BY INTERVENTION EVENTS**

# 3 Ukraine's case study

## 3.1 Introduction

Nitrogen dioxide ( $\text{NO}_2$ ) is a key air pollutant that can have harmful effects on human health. An increase in nitrogen oxide ( $\text{NOx} = \text{NO} + \text{NO}_2$ ) concentrations contributes to global warming through a chemical reaction that leads to the formation of ozone ( $\text{O}_3$ ), a short-lived climate pollutant with a potent warming effect (Stocker et al., 2013). The lifetime of  $\text{NO}_2$  is strongly influenced by photochemical reactions and meteorological parameters (Barré et al., 2021) and varies seasonally (Dragomir et al., 2015; Kendrick et al., 2015). During winter, photochemical reaction activity is reduced, resulting in a longer lifetime of the  $\text{NO}_2$ . Additionally, seasonal variations in  $\text{NO}_2$  concentration are controlled by dispersion processes which are significantly affected by changes in boundary layer height (BLH), wind speed and direction patterns due to temperature inversions in summer and winter (Barré et al., 2021; Kendrick et al., 2015).  $\text{NO}_2$  concentration levels have been widely used to evaluate decreases in emissions associated with intervention events such as the COVID-19 pandemic lockdown and impacts on the air quality due to the short lifetime of  $\text{NO}_2$  in the atmosphere (Barré et al., 2021; Cooper et al., 2022). In Europe, anthropogenic  $\text{NOx}$  emissions are mainly attributed to combustion processes in transportation, as well as energy production and distribution.

In Ukraine, coal-fired power plants (CPPs) dominantly account for 80% of total  $\text{SO}_2$  and 25% of total  $\text{NOx}$  emissions, and some have been identified as the highest-emitting CPPs in the region and in the world (Lauri and Rosa, 2021). Since the pandemic started in March 2020, and now with the ongoing armed conflict with Russia, Ukraine has faced a series of threats to the economy, human security and the environment, as well as geopolitical tensions (Pereira et al.,

2022). During the pandemic response starting in 2020, many national and local lockdown restrictions were issued to prevent the spread of the virus, causing a sharp decrease in gross domestic product growth rate, as well as industrial and energy production (Danylyshyn, 2020). In 2021, Ukraine's economy started to recover from the pandemic but the recovery was eventually upended by an armed conflict with Russia that started on February 24, 2022. The conflict has been causing a multi-pronged crisis not only in Ukraine but also in Europe, with increased prices and exacerbated inflation among the many impacts. Many facilities and extensive areas of housing and other infrastructure, including some CPPs, have been reported destroyed or damaged in Ukraine. These impacts have consequently triggered an unprecedented refugee crisis in Ukraine, clogging border crossings between Ukraine and bordering European countries (Júlia et al., 2022). The many socio-economic changes that have occurred during the pandemic and the conflict could be expected to contribute to major variability in air quality in Ukraine, including NO<sub>2</sub> pollution levels, during the 2020–2022 period.

A report by the United Nations Development Programme (UNDP) (Dumitru et al., 2020), estimated the impacts of the pandemic lockdown on NO<sub>2</sub> levels in Ukraine by using Sentinel 5P (S5P) NO<sub>2</sub> column concentrations and Copernicus Atmosphere Monitoring Service (CAMS) surface NO<sub>2</sub> data (Marécal et al., 2015). However, meteorological variables were not acknowledged, although ignoring weather factors could strongly affect final estimates of changes in pollution concentration levels induced by the lockdown (Schiermeier, 2020). A more recent study (Zalakeviciute et al., 2022) utilized direct satellite observation from 2019 and early 2020 as business-as-usual data to evaluate the impact of the Russia-Ukraine conflict in 2022 on air quality, but again, without acknowledging weather effects. These two studies utilized estimates of year-to-year differences. However, such estimates can easily be affected and dominated by changes in meteorological parameters rather than emission sources (Grange et al., 2021; Shi et al., 2021). Therefore, a more sophisticated method is needed to measure the impacts of intervention events through better quantification of actual air quality.

In order to normalize the meteorological effects to accurately and reliably quantify the impact of intervention events, the use of machine learning is increasingly being adopted, but mostly applied for ground-based measurements following the

original idea proposed by (Grange et al., 2018) and (Grange and Carslaw, 2019). The objective of this approach is to construct a business-as-usual (BAU) model for predicting air pollution levels independently of the impacts of any intervention events. This is achieved by integrating meteorological, spatial, and temporal features into the model during the BAU period to accurately represent air pollution levels. An intervention event, in this context, refers to an occurrence that has caused changes in air quality. Recently, (Barré et al., 2021) have introduced their weather normalization approach to improve estimates of lockdown impacts not only on NO<sub>2</sub> levels from ground-based observations and CAMS simulations, but also in satellite measurements from S5P. The original method in (Grange et al., 2018; Grange and Carslaw, 2019) has been altered in order to work with satellite retrieval column NO<sub>2</sub> concentration levels from S5P by adopting a new feature, the forecast surface NO<sub>2</sub> level from CAMS data. Alternatively, gradient boosting machines (GBMs) (Friedman, 2001) have been also utilized instead of random forests (Grange et al., 2018) to develop weather-normalization models under the BAU conditions. (Barré et al., 2021) reported an overall reduction (ranging from 23% to 32%) in major European cities using the three datasets. Their study showed an average difference of 14% between satellite-based and ground-based estimates, and 11% between simulations from the CAMS regional ensemble of air quality models and ground-based estimates. These findings suggest that estimates of the impacts of the lockdown on NO<sub>2</sub> levels can vary depending on the source of the data.

This chapter aims to investigate the actual satellite-derived column NO<sub>2</sub> pollution levels induced by pandemic lockdown restrictions and the armed conflict with Russia, which have been two major changes in human activities in Ukraine since 2019. In order to do so, we developed a weather-normalization model under BAU scenarios for S5P column NO<sub>2</sub> levels to decouple the meteorological effects from the intervention effects. The BAU simulation NO<sub>2</sub> levels are then used to quantify changes in S5P column NO<sub>2</sub> concentrations during the lockdown and the armed conflict. We describe the data used in the study in section 3.2 and the methodology in section 3.3. The results and discussion on NO<sub>2</sub> level changes are summarized in section 3.4 for the lockdown, and section 3.5 for the armed conflict. Finally, we conclude the results of the study in section 3.6.

## 3.2 Data

### 3.2.1 Selection of analysis periods

In this study, we consider the three years 2019, 2020, and 2022 for our analysis. We assumed that in 2019, before the lockdown in 2020 and the armed conflict with Russia in 2022, there were no other significant factors impacting socio-economic activities. Hence, we used 2019 NO<sub>2</sub> pollution levels as the reference data for development of the BAU model.

Ukraine reported its first active case of COVID-19 on March 3, 2020, and began closing its borders to foreign citizens from March 15 onwards. Around the same time, the country also witnessed its first COVID-19 related death. On April 6, the government introduced a strict lockdown, imposing significant restrictions on movement and requiring the public to wear masks in public spaces. This lockdown was eventually extended until June, although certain restrictions were already lifted starting from May 11. For the lockdown component of our study, we focused on two specific periods: the pre-lockdown period, which ran from March 1 to 15, 2020, and the strict lockdown period, spanning from April 6 to May 10, 2020. The decision to count the pre-lockdown period from March 1 was based on the lack of qualified S5P data available for analysis before March, as indicated in 3.2. In 2021, even though COVID-19 vaccines had been developed and distributed to citizens of Ukraine (vaccinations started on February 24, 2021), many local lockdowns and restrictions continued to be issued to cope with growing numbers of daily COVID-19 active cases, while trying to keep socio-economic activities on track for recovery.

The Russia-Ukraine conflict began on February 24, 2022. We employed data for the period February 1 to July 31 each year from 2019 to 2022 for NO<sub>2</sub> variability analysis. This time frame covers the pre-lockdown and lockdown periods in 2020 and extends beyond the first five months (February 24 to July 31) of the armed conflict in 2022.

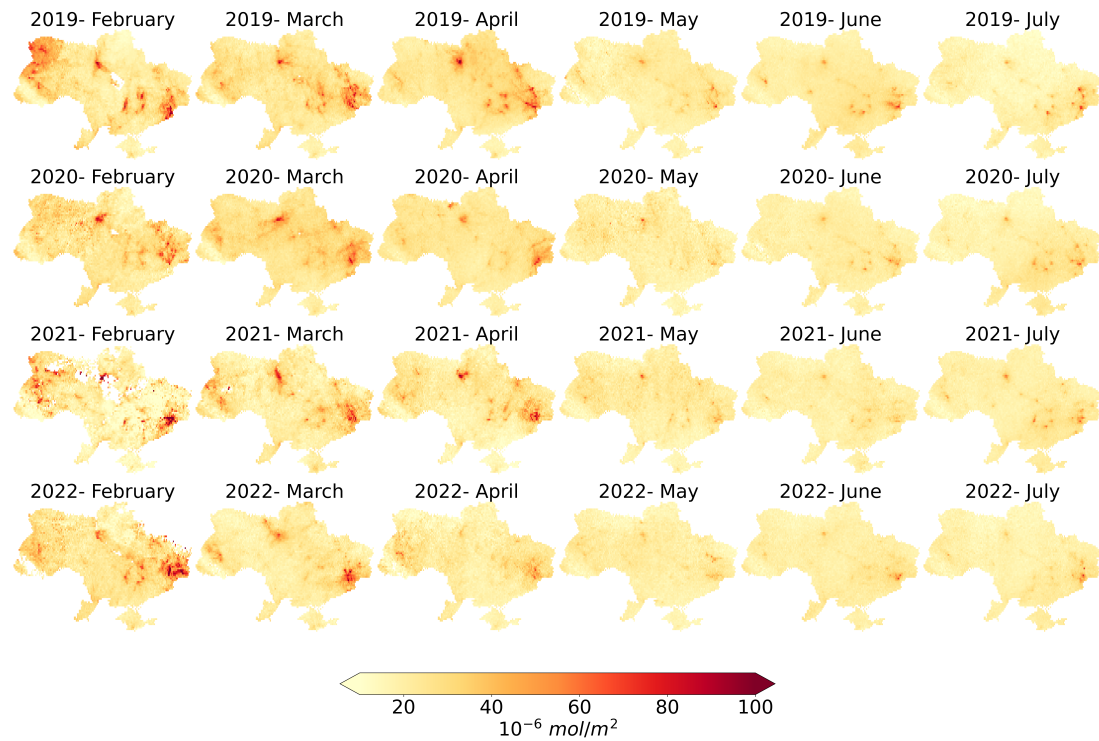
### 3.2.2 TROPOMI NO<sub>2</sub> from Sentinel 5P

Most previous studies assessing the impacts of intervention involved ground observations in their analysis. However, reliable ground measurement data was only available in Kyiv (capital of Ukraine) as other sites had been damaged or destroyed in the armed conflict and taken out of service (Savenets, 2021). Thus, open satellite data is considered the most efficient way to monitor air quality for all parts of Ukrainian territory (Shelestov et al., 2021).

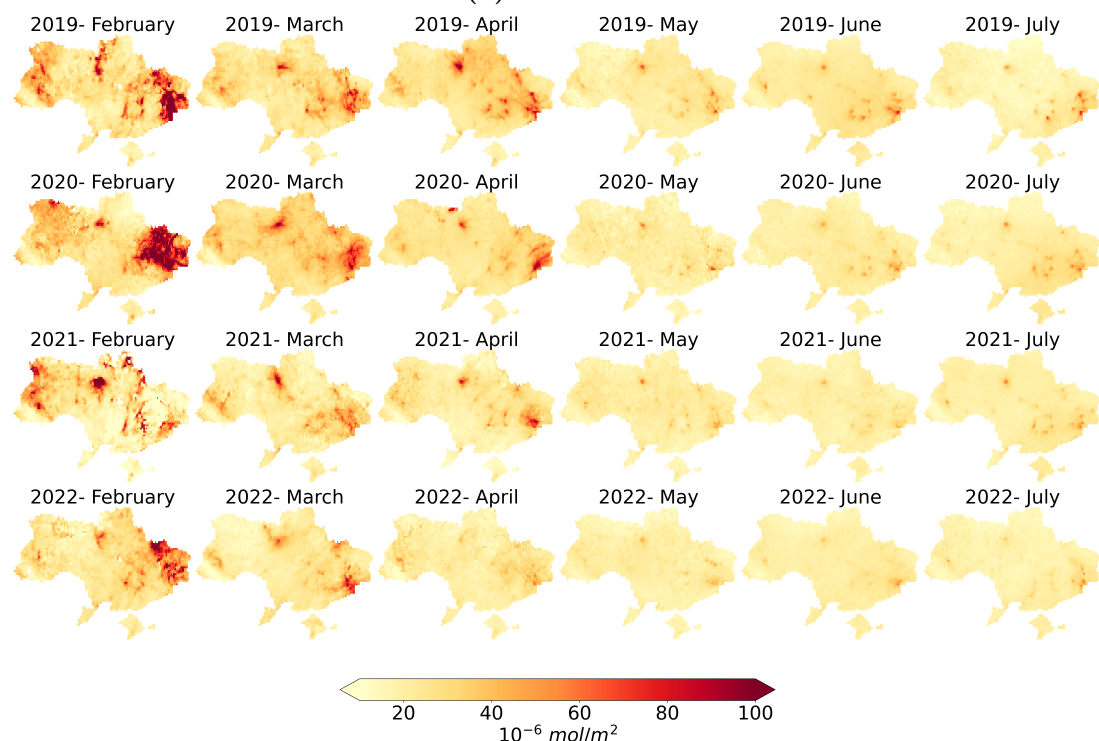
The S5P data has been distributed from 2018 to the present with two available options. The first is original data (ORG) processed with either of two versions of processor, v1.x (5/2018–6/2021) or v2.x (7/2021 onwards). The second is reprocessed datasets (RPRO) with the processor (v2.x) for the full mission. According to (Van Geffen et al., 2022), the S5P NO<sub>2</sub> v2.2 data has larger vertical column density (VCDs) than v1.x data, ranging from 10% to 40%, mostly found at mid and high latitudes in winter. Therefore, bias between S5P v1.x and v2.x could lead to overestimation and underestimation when comparing air pollution data in 2022 versus 2019, thereby affecting evaluations of the conflict's impacts on S5P NO<sub>2</sub> levels.

In this study, we conducted experiments using two versions of S5P NO<sub>2</sub> data. The first dataset is ORG data which was collected through level 3 (L3) offline processing (OFF) of the S5P product available on Google Earth Engine (Gorelick et al., 2017). This dataset comprises processed data from different processor versions for each year from 2019 to 2022 (v1.3.1 in 2019, v1.3.2 in 2020, and v2.3.1 in 2022). The second dataset, denoted as the RPRO product, employs processor version v2.4.0 for the full mission duration. This dataset was acquired from the Sentinel-5P Pre-Operations Data Hub ([s5phub.copernicus.eu](http://s5phub.copernicus.eu)) using the Sentinelsat API.

Regarding the RPRO data, we began by downloading the level 2 (L2) dataset. In order to generate the L3 NO<sub>2</sub> dataset, each operational L2 product underwent mosaicking and filtering of low-quality pixels, which involved removing items with quality assurance (QA) values less than 75% for the “tropospheric\_NO<sub>2</sub>\_column\_number\_density” band. The harpconvert tool was utilized to perform the conversion from L2 to L3 product. Subsequently, both datasets were linearly interpolated to a spatial resolution of 0.1×0.1 degree. At

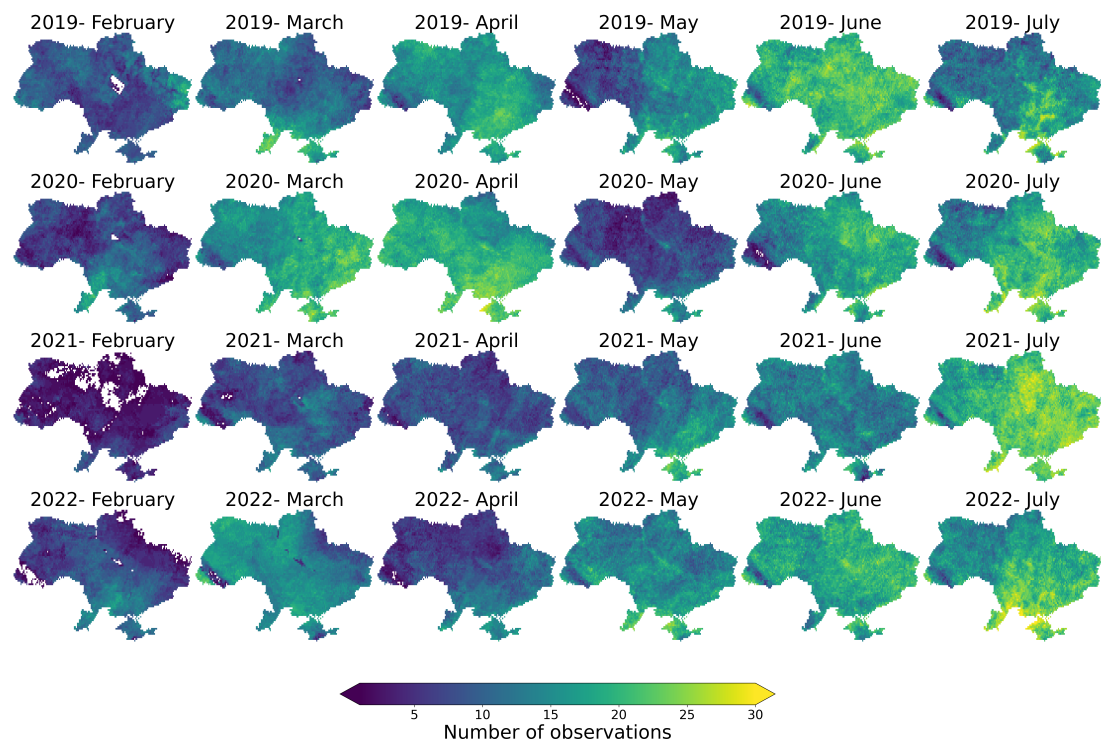


(a) ORG data

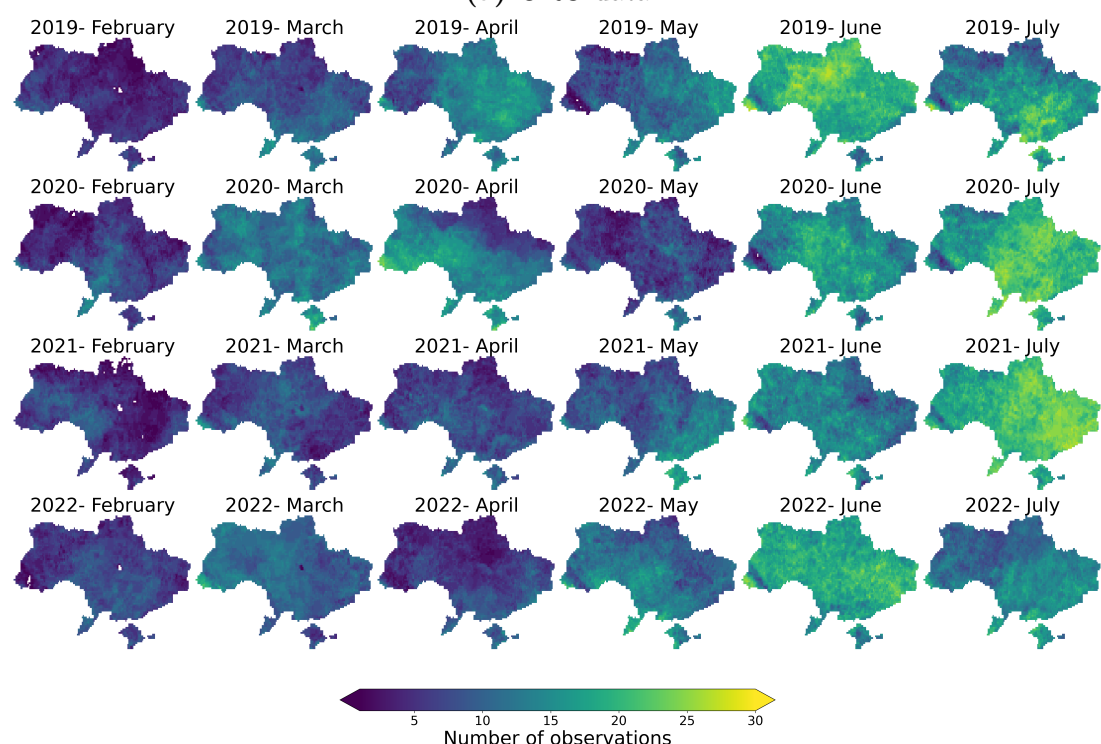


(b) RPRO data

**Figure 3.1.** Monthly (February to July) average map of TROPOMI S5P NO<sub>2</sub> tropospheric columns for Ukraine from 2019 to 2022



(a) ORG data



(b) RPRO data

**Figure 3.2.** Monthly (from February to July) number of TROPOMI S5P NO<sub>2</sub> tropospheric columns observations for Ukraine from 2019 to 2022

the time of the experiment, the RPRO data was only accessible until July 2022.

Plots presented in Figure 3.1 display the average monthly TROPOMI NO<sub>2</sub> tropospheric column over Ukraine from 2019 to 2022 (February to July) using the ORG data (Figure 3.1a) and RPRO data (Figure 3.1b), respectively. In 2020, a reduction of 4.8% (ORG data) and 8.3% (RPRO data) in mean NO<sub>2</sub> levels over the Ukrainian territory was observed from April to May, compared to levels recorded in 2019. In 2022, a reduction of 2.4% (ORG data) and 2.9% (RPRO data) was seen from March to July, compared to levels recorded in 2021. Additionally, during the same period, a reduction of 10.3% (ORG data) and 15% (RPRO data) was observed, compared to the NO<sub>2</sub> levels recorded in 2019. We observed that the reduction in NO<sub>2</sub> levels was more significant in the RPRO data compared to the ORG data, both during the lockdown in 2020 and the first five months (March–July) of the conflict in 2022 in Ukraine.

We summarize the number of qualified observations available for each month from 2019 to 2022 (February to July) in Ukraine using the ORG data (Figure 3.2a) and RPRO data (Figure 3.2b). The quantification of seasonal NO<sub>2</sub> levels can be challenging, particularly during the selected months in winter (February) and spring (March, April) of 2021 and 2022, due to the limited availability of qualified observations. This is further complicated when attempting to estimate changes before and after intervention events such as the lockdown and the armed conflict in Ukraine, as the before period falls within the winter months when observations are scarce.

### 3.2.3 Meteorological and surface NO<sub>2</sub> data

In this study, the meteorological and surface NO<sub>2</sub> data are utilized as the predictors for the estimation of NO<sub>2</sub> under BAU conditions as suggested by (Barré et al., 2021). The meteorological data is ERA5 reanalysis data which is collected from the Climate Data Store of the Copernicus Climate Change Service (Hersbach et al., 2018). We use the following weather variables: 10 m wind speed (u and v component, m/s) and direction (degrees), 2m air temperature (K), 2m dewpoint temperature (K), relative humidity (%), geopotential (m<sup>2</sup>/s<sup>2</sup>), and BLH (m). All the variables are downloaded at the original resolution of  $0.25 \times 0.25$  degree and then linearly interpolated to  $0.1 \times 0.1$  degree (about  $10\text{km} \times 10\text{km}$ ) resolution. The

utilized surface NO<sub>2</sub> data is collected from CAMS European air quality forecast and reanalyses and forecast (Marécal et al., 2015) by using the Atmosphere Data Store of the CAMS (<https://ads.atmosphere.copernicus.eu/>). Since the forecast data is a 3-year rolling archive from the present, we utilized the analysis data for 2019. The surface NO<sub>2</sub> forecast data served as the predictors under the BAU scenario for 2020 to 2022. As forecast predictions do not involve an assimilation process (Barré et al., 2021), we expect no effect of the pandemic lockdown, and the impact of the armed conflict related events on air pollution was included in the surface NO<sub>2</sub> pollution level. Both forecast and analysis data are available at the resolution of 0.1×0.1 degree. We calculated the mean values based on data from 13:00 and 14:00 hours local time to represent the surface NO<sub>2</sub> and meteorology value at the time the satellite S5P overpassed Ukraine.

### 3.2.4 Fire spots database and Ukraine crisis hub

In order to draw a detailed picture of the battle spots, we utilized data from Fire Information for Resource Management System (FIRMS) provided by National Aeronautics and Space Administration (NASA) and Ukraine Crisis Hub data from the Armed Conflict Location and Event Data Project (ACLED) (Raleigh et al., 2010). The NASA FIRMS portal provides active fire data at three-hour intervals based on satellite observations from products of the Moderate Resolution Imaging Spectroradiometer (MODIS) and Visible Infrared Imaging Radiometer Suite (VIIRS). For the study, data from the VIIRS product was employed to access the active fire spots due to its superior fire detection capabilities compared to the MODIS products (Csiszar et al., 2014; Schroeder et al., 2014).

Detailed data on conflict hotspot locations are extracted from the Ukraine Crisis Hub which is distributed by ACLED (Raleigh et al., 2010). Information regarding the conflict events is updated weekly and disaggregated to event type with time and location (latitude and longitude) in Ukraine and the Black Sea region available from 2018 until the present. As a result of the conflict, we expect to see and identify corresponding patterns between locations of active fire spots and the locations of conflict events.

### 3.2.5 Population data

As NO<sub>2</sub> pollution levels are closely related to human socio-economic activities and frequently high in populous urban areas, we downloaded 2020 population data for Ukraine from the WorldPop Global Project ([www.worldpop.org](http://www.worldpop.org)), available annually at the spatial resolution of 100m×100m as one of the features for the BAU NO<sub>2</sub> model. The population data was collected, clipped to the Ukrainian territory, and linearly interpolated to 0.1×0.1 degree (about 10km×10km).

## 3.3 Business-as-usual (BAU) modelling

When considering changes induced by the pandemic lockdown and the armed conflict, especially for before-after analysis, an important factor is the meteorology variations. In this study, we use a suggested list of predictors by (Barré et al., 2021), which consists of meteorological, spatial, and temporal features, population counts from WorldPop Global Project, and surface NO<sub>2</sub> pollution levels from CAMS European analysis data for 2019 and forecast data for 2020 to 2022 for BAU model development. The spatial and temporal features contain latitude, longitude, Julian date (number of the day from January 1), and day of the week, respectively. However, unlike the study cited (Barré et al., 2021), for machine learning model selection, instead of GBM we utilized LightGBM (Ke et al., 2017), which is a gradient boosting decision tree, to build the BAU model. During the training process, other than in studies that used the grid search with an n-fold cross-validation approach to tune the model's hyperparameters (Barré et al., 2021; Petetin et al., 2020), we employed the Fast Library for Automated Machine Learning (FLAML) (Wang et al., 2021), which is a new lightweight library for quickly determining the accurate model, to find the optimum hyperparameters for the LightGBM model in our case.

In order to assess the performance of the BAU simulation model, we randomly selected and used 80% of the data for the training set and 20% for the validation set. We used the following metrics: mean bias (MB), normalized mean bias (nMB), root mean square error (RMSE), normalized root mean square error (nRMSE) and Pearson correlation coefficient (R). As shown in the detailed results presented in Table 3.1, the model achieved high R on the validation set

**Table 3.1.** The performance of the BAU model on the validation set described using the following metrics: mean bias (MB), normalized mean bias (nMB), root mean square error (RMSE), normalized root mean square error (nRMSE) and Pearson correlation coefficient (R). N represents the number of points in both the training set and validation set, where each point is associated with unique latitude and longitude values. There are no duplicate points shared between the training and validation sets.

	MB	nMB	RMSE	nRMSE	R	n
Performance with S5P data version 1.x—ORG data						
Training set	$3.68 \times 10^{-5}$	$1.53 \times 10^{-4}$	7.80	7.40	0.87	5022
Validation set	0.03	0.10	9.53	10.98	0.80	1269
Performance with S5P data version 2.4—RPRO data						
Training set	$2.67 \times 10^{-4}$	$1.04 \times 10^{-3}$	6.97	5.12	0.91	5051
Validation set	0.07	0.26	8.47	7.75	0.86	1242

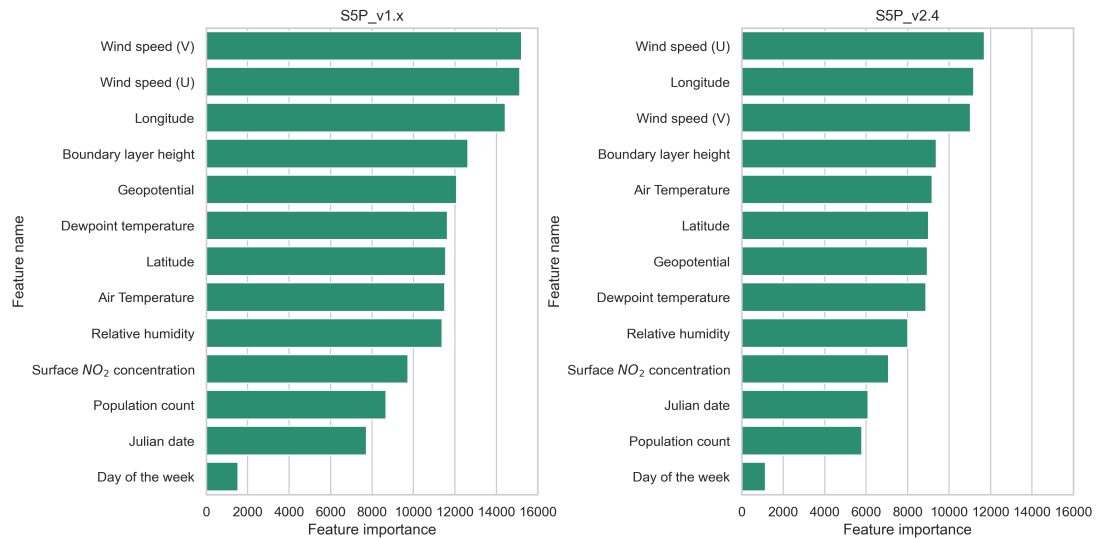


**Figure 3.3.** Feature importance estimated using LightGBM split method.

(0.8 for ORG data, 0.86 for RPRO data), with low MB and RMSE indicating that the column NO<sub>2</sub> levels are well represented by the input features. Based on the feature importance measure as shown in Figure 3.3, we found that the most

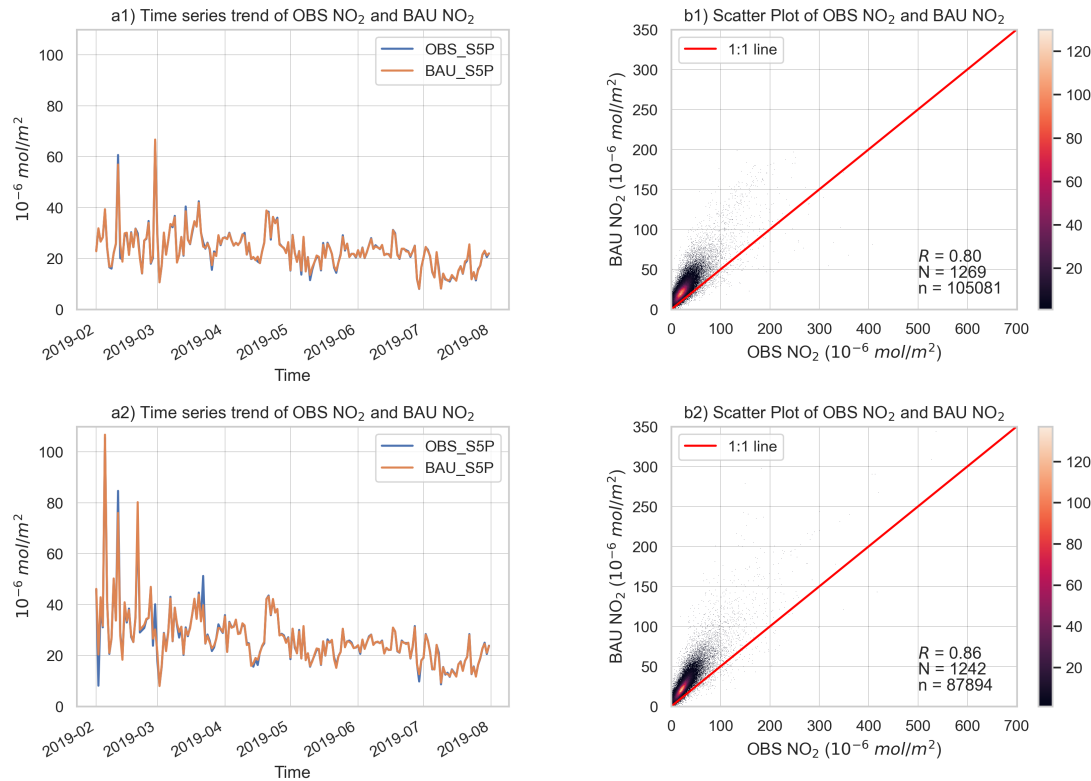
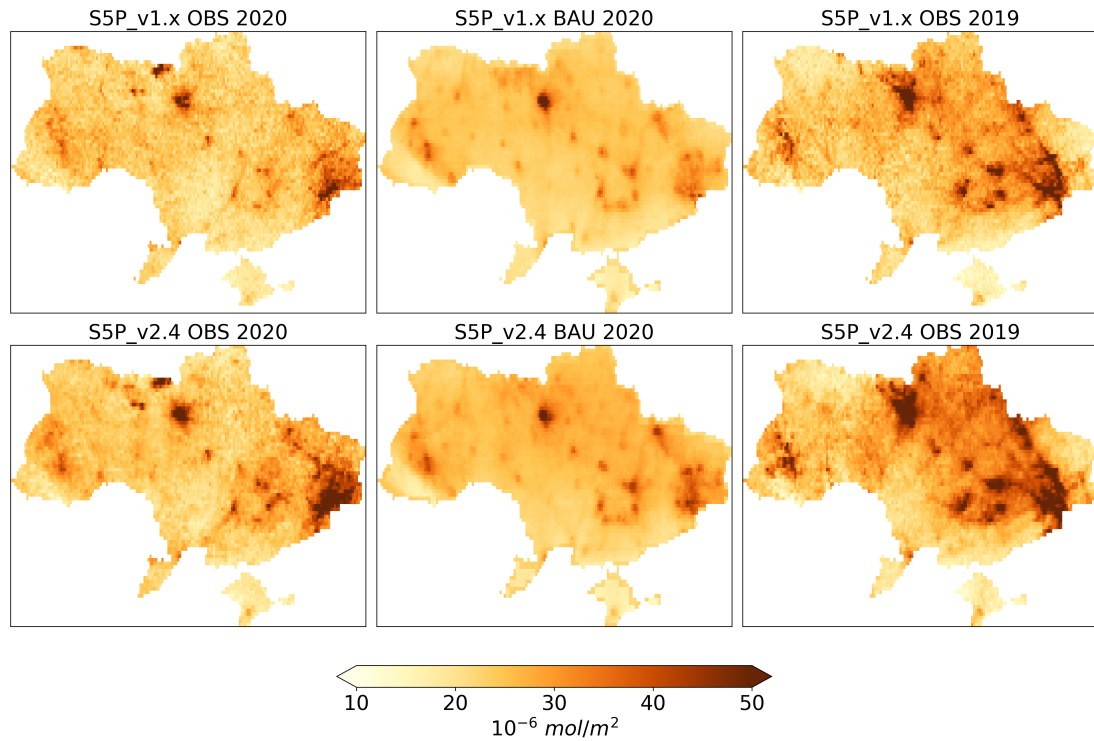
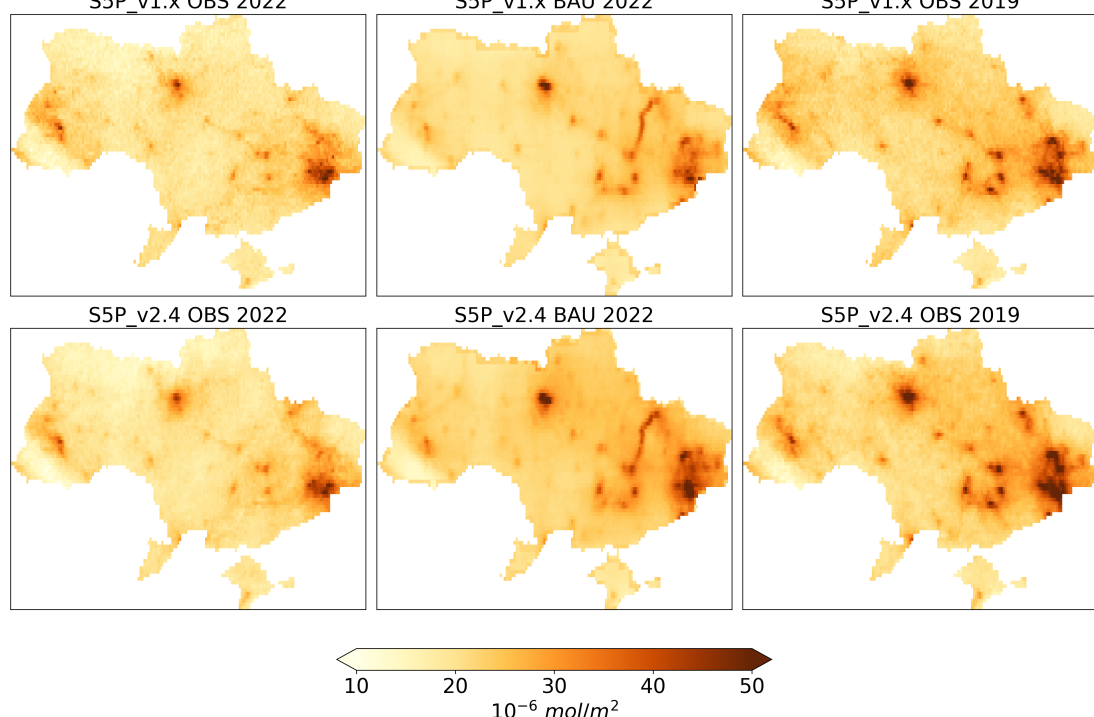


**Figure 3.4.** The timeseries trend lines (a1) and (a2) and scatter plots (b1) and (b2) depict the  $OBS_{NO_2}$  and  $BAU_{NO_2}$  on the validation set in 2019. Sub-figures (a1) and (b1) correspond to the S5P version 1.x data, while sub-figures (a2) and (b2) represent the S5P version 2.4 data. In the scatter plot, we showed the 1:1 line, Pearson correlation coefficient ( $R$ ),  $N$  represents the number of points in both the training set and validation set, where each point is associated with unique latitude and longitude values. At each point, we used the available daily data from February 1 to July 31, 2019, to make the training and validation set with total number samples is denoted as  $n$ . There are no duplicate points and samples shared between the training and validation sets.

important predictors are wind speed and direction, and BLH, which is also consistent with our hypothesis about the impact of the meteorological parameters on column  $NO_2$  levels mentioned above. In Figure 3.4, we present the performance of the BAU model on the validation set using trend lines and scatter plots to



(a) The OBS, BAU data in 2020 (April 6 to May 10) with reference data in 2019



(b) The OBS, BAU data in 2022 (February 24 to July 31) with reference data in 2019

**Figure 3.5.** The OBS (1st column), BAU (2nd column) data from April 6 to May 10, 2020 (a) and from February 24 to July 31, 2022 (b) with the corresponding reference data in 2019 (3rd column)

compare the predictions with the actual ground truth data. Furthermore, Figure 3.5 displays the OBS data, BAU model's predictions during the lockdown period in 2020, and more than five months of the conflict (February 24–July 31) in 2022. This data is accompanied by the reference NO<sub>2</sub> levels from 2019 which were utilized to train the BAU for corresponding periods. The hyperparameters used to develop the LightGBM model are listed in Table 3.2 for S5P data version 1.x and version 2.4.

**Table 3.2.** The hyperparameters used to develop the LightGBM model with S5P data version 1.x and version 2.4. We used FLAML library (Wang et al., 2021) for tuning these following parameters: shrinkage rate (learning\_rate), minimal number of data in one leaf (min\_data\_in\_leaf), minimal sum hessian in one leaf (min\_sum\_hessian\_in\_leaf), number of boosting iterations (num\_iterations), max number of leaves in one tree (num\_leaves).

Parameter	S5P v1.x	S5P v2.4
learning_rate	0.30775042929674906	0.3858774543125185
min_data_in_leaf	11	5
min_sum_hessian_in_leaf	0.001	0.001
num_iterations	907	3451
num_leaves	8604	4342

The main shortcoming of this method is the lack of qualified reference data to develop the weather normalization model under BAU conditions, as the S5P TROPOMI data has been only available since mid-2018. Only one year of training data in 2019 is considered relatively small, thus resulting in large errors in BAU simulations in winter months as during this time, limited qualified S5P observations are available and NO<sub>2</sub> pollution levels are quite unpredictable due to the inconsistency in heating activities and NO<sub>2</sub> intake from Poland.

### 3.4 COVID-19 induced NO<sub>2</sub> changes

The purpose of this section is to examine the effect of the lockdown on changes in NO<sub>2</sub> column levels in populous urban areas, namely the nine cities Kyiv, Kharkiv,

Odessa, Dnipro, Donetsk, Zaporizhzhia, Lviv, Kryvyi Rih, and Mykolaiv (listed in declining order of population). To begin, we analyse the meteorological patterns during the pre-lockdown and lockdown periods and discuss how these might influence the NO<sub>2</sub> levels, apart from the impacts of the lockdown measures. Next, we utilize two methods to estimate changes in NO<sub>2</sub> levels. The first method, known as the year-to-year approach suggested by (Barré et al., 2021), involves calculating the median value of the actual S5P observation data in 2020 and subtracting the observation data from 2019. The second method, OBS-BAU, utilizes the median value of the actual observation data (OBS) in 2020 and subtracts the simulated NO<sub>2</sub> levels that represent the BAU scenario, which are predicted by the S5P tropospheric NO<sub>2</sub> column levels without any lockdown measures. The BAU simulations are based on the representation of meteorological, spatial, and temporal parameters.

### 3.4.1 Lockdown and pre-lockdown meteorological patterns

Figure 3.6a and 3.6b display the probability density functions of the BLH, and Figure 3.6c and 3.6d display wind speed and direction during the pre-lockdown and lockdown periods of 2019 and 2020 based on data from the nine selected cities. In 2020, the BLH exhibited a similar distribution to that of 2019 during the pre-lockdown period, but with lower values. This decrease in BLH would have resulted in an increase in NO<sub>2</sub> levels in 2020 compared to 2019, as the reduced BLH restricts the dispersion of NO<sub>2</sub> emissions, leading to an increase in NO<sub>2</sub> concentration levels (see Figure 3.6a).

Conversely, during the lockdown period (see Figure 3.6b), we observed higher values of BLH in 2020 compared to 2019. This increase in BLH could have contributed to the dispersion of NO<sub>2</sub> concentration, resulting in a reduction of NO<sub>2</sub> levels during the lockdown in 2020. This phenomenon, in addition to the effects of the lockdown restrictions, may have also contributed to minimizing the NO<sub>2</sub> levels over major cities in Ukraine. Therefore, it is essential to consider the impacts of meteorological variables on NO<sub>2</sub> level variability analysis.

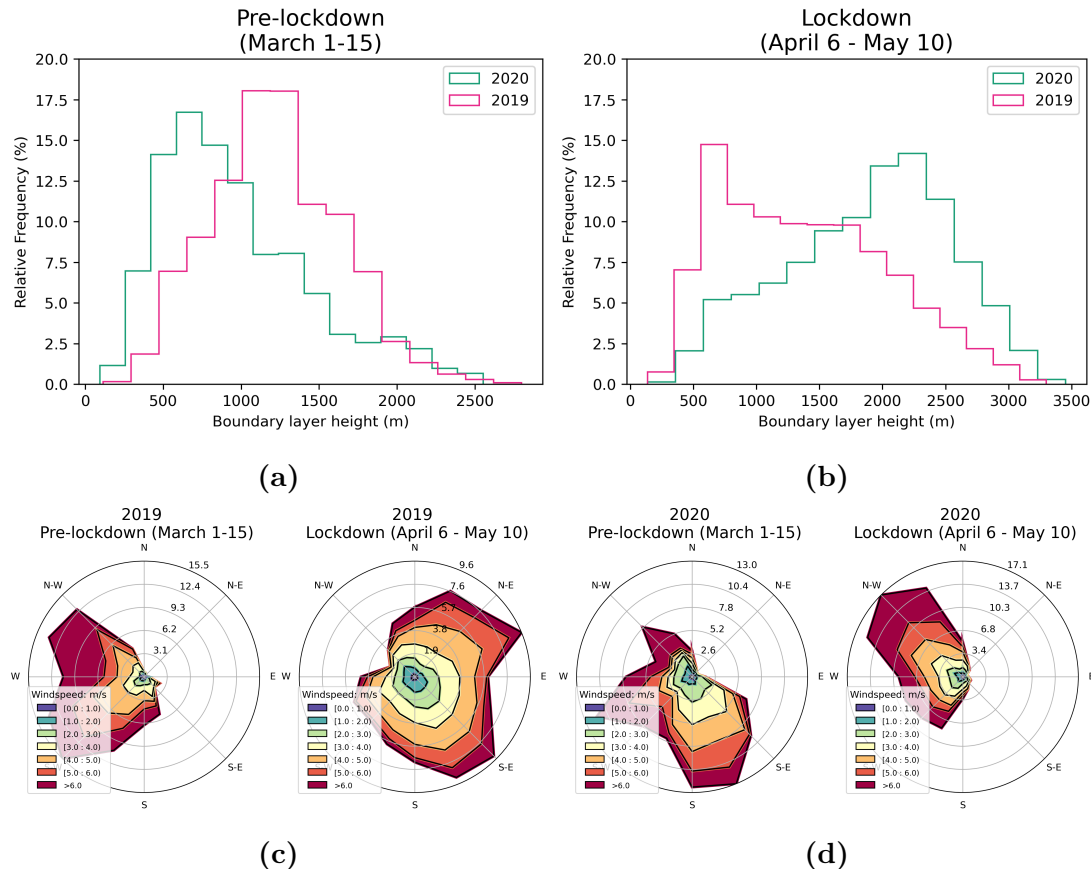


**Figure 3.6.** Probability density functions of BLH during (a) the pre-lockdown (March 1–15) and (b) the lockdown period (April 6–May 10) between 2019 and 2020 based on data from the nine most populous cities of Ukraine. Wind rose plots for wind speed and direction for pre-lockdown (March 1–15) and lockdown (April 6–May 10) periods in (c) 2019 and (d) 2020 based on data from the nine most populous cities of Ukraine

### 3.4.2 NO<sub>2</sub> changes in populous Ukrainian cities

In Figures (3.7a, 3.7b), and Table 3.3, we present the result of the year-to-year approach. We assumed that there would be a minimal change in NO<sub>2</sub> pollution levels during the pre-lockdown period, but a significant reduction during the lockdown when comparing the same time frame in 2019 and 2020 due to the implemented lockdown measures and social distancing practices. In Figure 3.7,

two different methods, namely the OBS-BAU and year-to-year approaches, were used for the analysis. The circle size in the figures corresponds to the population of each city. For each sub-figure (a) and (b), the first row (a1, a2, b1, b2) contains two plots showing the results based on the ORG data (S5P v1.x), while the second row (a3, a4, b3, b4) includes two plots presenting the results based on the RPRO data (S5P v2.4). The left column plots (a1, a3, b1, b3) of Figures (3.7a, 3.7b) display the year-to-year estimates, while the right column plots (a2, a4, b2, b4) display the OBS-BAU estimates. Figure 3.7a illustrates that the prevailing trend in the nine selected cities during the pre-lockdown period showed an increase, with an average of 5.2% (ORG data) and 13.9% (RPRO data) in NO<sub>2</sub> levels, while during the lockdown period (Figure 3.7b), a general reduction was observed in most cities with an average of 15.6% (ORG data) and 11.1% (RPRO data). This confirms that the lockdown measures reduced the NO<sub>2</sub> column concentrations in major urban areas of Ukraine, as we anticipated. It is worth noting that the year-to-year approach using the original satellite observations has been widely used in many studies and online resources. However, as mentioned in (Barré et al., 2021; Grange et al., 2021), it is heavily influenced by meteorological variables such as wind speed and direction, and BLH (Wallace and Kanaroglou, 2009).

In order to quantify the true improvement in air quality with respect to column NO<sub>2</sub> levels due to the lockdown restrictions, we calculated the difference between the actual observation data and the simulated data under BAU conditions with the meteorological effects decoupled. Like the year-to-year approach, we anticipate a slight variation between the OBS NO<sub>2</sub> levels and the BAU NO<sub>2</sub> levels during the pre-lockdown period. Furthermore, we expect to observe an overall reduction in the OBS data compared to the BAU data, or at least, a lesser increase during the lockdown when compared to the pre-lockdown levels, due to the impact of the lockdown measures. Figure 3.7((a2, a4) and (b2, b4)) shows the OBS-BAU estimates for pre-lockdown and lockdown in 2020. During the pre-lockdown (Figure 3.7(a2, a4)), we observed an average increase of 3.7% (ORG data) and 12.5% (RPRO data), which is smaller than the year-to-year estimate. However, during the lockdown period (Figure 3.7(b2, b4)) a smaller increase trend was observed, with an average of 0.5% (ORG data) and 10.2% (RPRO data). This indicates that while the OBS NO<sub>2</sub> levels in 2020 were higher than those predicted under the

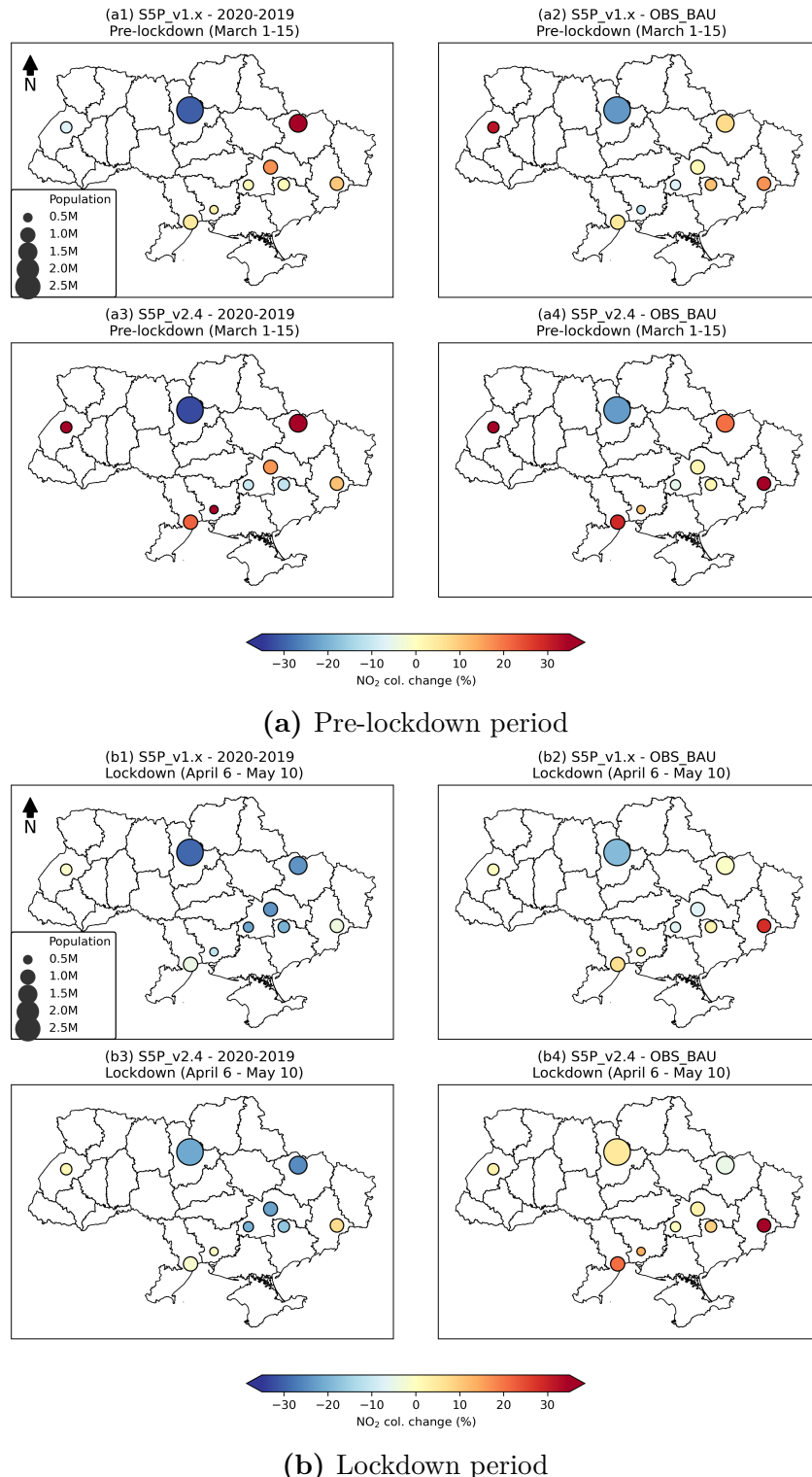


**Figure 3.7.** Estimates of S5P NO<sub>2</sub> column changes for the nine most populous cities in Ukraine during the (a) pre-lockdown and (b) lockdown periods.

**Table 3.3.** The OBS-BAU and year-to-year (2020–2019) estimates (in percentage) during pre-lockdown and lockdown periods in the nine most populous cities in Ukraine. The values are represented as mean, while standard deviation is not presented here due to lack of space.

City	Pre-lockdown (March 1 – 15)				Lockdown (April 6 – May 10)			
	OBS-BAU		2020–2019		OBS-BAU		2020–2019	
	ORG	RPRO	ORG	RPRO	ORG	RPRO	ORG	RPRO
Kyiv	−23.7	−23.1	−30.6	−32.8	−18.8	4.9	−29.4	−21.4
Kharkiv	7.6	20.8	47.9	49.1	−0.9	−4.9	−24.1	−24.9
Odessa	5.1	29.0	4.8	22.4	6.9	21.0	−4.4	−1.9
Dnipro	1.3	1.5	17.0	16.7	−6.6	2.8	−23.9	−22.3
Donetsk	16.8	41.9	10.3	11.2	28.2	42.0	−4.0	7.2
Zaporizhzhia	11.5	1.9	0.6	−11.1	2.5	9.1	−20.1	−17.2
Lviv	32.2	35.7	−7.3	37.7	0.0	3.0	−1.2	1.4
Kryvyi Rih	−7.3	−5.3	1.2	−9.8	−6.4	0.1	−21.9	−20.5
Mykolaiv	−10.2	10.1	3.3	41.5	−0.6	13.8	−11.1	−0.4
Mean	3.7	12.5	5.2	13.9	0.5	10.2	−15.6	−11.1

BAU scenario during the lockdown period, the measures implemented during the lockdown effectively curbed the increase in NO<sub>2</sub> column concentrations in major urban areas of Ukraine when compared to the pre-lockdown levels, aligning with our initial expectations. By using the OBS-BAU estimate based on the ORG data, the most significant reduction was observed in Kyiv (18.8%), with Dnipro and Kryvyi Rih experiencing smaller reductions of 6.6% and 6.4%, respectively. However, when using RPRO data, a reduction was only seen in Kharkiv (4.9%).

In comparison with the year-to-year approach with respect to the pre-lockdown (see Table 3.3), the OBS-BAU estimates (3.7% for ORG data, 12.5% for RPRO data) show a smaller change than in year-to-year estimates (5.2% for ORG data, 13.9% for RPRO data). We consider the OBS-BAU estimate to be more reasonable as mentioned above, and the lower values in BLH in 2020 could result in higher year-to-year estimates during the pre-lockdown period between 2020 and 2019. Therefore, we anticipate a lower estimate, which is a smaller increase, after the weather effects are decoupled. Similar findings are seen during the lockdown

for OBS-BAU and year-to-year estimates. The contribution from the lower BLH in 2019 could overestimate the reduction of NO<sub>2</sub> concentrations by 15.6% (ORG data) and 11.1% (RPRO data) in the year-to-year lockdown estimates. By normalizing the weather effects, a lower reduction in the increase is anticipated and estimated from the OBS-BAU approach (0.5% for ORG data, 10.2% for RPRO data). Additionally, the year-to-year approaches mostly present a larger standard deviation than the OBS-BAU approach, which could be attributed to local biases caused by meteorological variabilities (Barré et al., 2021). Using weather-normalization techniques, we observed that much of the reduction in NO<sub>2</sub> levels between 2020 and 2019 can be attributed to weather variability. This suggests that stricter measures may need to be considered in the future to achieve significant NO<sub>2</sub> reductions in densely populated areas of Ukraine.

### 3.5 NO<sub>2</sub> changes induced by the armed conflict

In the previous section, we discussed the influence of meteorological factors on the concentration of NO<sub>2</sub> and how using OBS-BAU estimates can mitigate overestimation or underestimation in the year-to-year approach. In this section, we shift our focus solely to the OBS-BAU estimates to explore the impacts of the armed conflict on NO<sub>2</sub> column concentration. The year-to-year estimates are displayed together for the purpose of comparison.

During the lockdown, one might reasonably assume that pollution levels were likely to decrease as the result of an anticipated reduction in socio-economic activities in major urban areas. However, trends in NO<sub>2</sub> levels during the conflict are likely to be unpredictable in the chaos of armed conflict actions and regionally attributed to various type of emissions at multiple locations, especially at the beginning of the conflict. On one hand, the NO<sub>2</sub> levels should be expected to decline as anthropogenic emissions would be expected to decline due to minimized activities in transportation, industry and other socio-economic activities. On the other hand, surges in conflict activities – such as attacks with missiles, artillery shelling, bomb and mine explosions, etc., as well as the constant usage of military vehicles and the transportation of civilian populations from conflict zones in such a short time – could result in a rise in air pollution levels. Therefore, we extend our

study beyond the most populous cities and include other territories in Ukraine affected by the conflict. To accomplish this, we begin by locating the conflict hotspots where military actions and battles took place, and then analyse the changes in NO<sub>2</sub> concentrations in the hotspots, which are highly contested zones. We estimated the changes in pollution levels from individual conflict points, and the results are presented in Section 5.1. In Section 5.2, we analyse the impacts of the conflict on NO<sub>2</sub> levels in other affected regions, such as major cities with populations exceeding 0.5 million, and the areas surrounding CPPs.

### 3.5.1 S5P NO<sub>2</sub> level changes in conflict hotspots

#### Satellite-captured fire spots and statistics in conflict hotspots

To understand the distribution of conflict hotspots, we utilized both the satellite-capture fire data from the NASA FIRMS portal, and in particular, the locations of battles provided by ACLED (Raleigh et al., 2010). First, we inspect the fire data from the VIIRS fire product for two consecutive years (2021 and 2022), searching for patterns representing the appearance of conflict hotspots. Then, we visually compare the pattern of fire spots captured by satellite with the reported battle locations.

Figure 3.8 displays the satellite-captured fire spots for 2021 (1st column), 2022 (2nd column) and locations of conflict hotspots (3rd column). We only show the similar patterns captured from the monthly NASA FIRMS product and the reported conflict hotspot locations from Ukraine Crisis Hub, to avoid the overwhelming plots of 12 months. We observe that from February 24 until the end of March, the distribution of the detected fire spots forms no certain pattern and is scattered over the Ukrainian territory. From April to July 2022 the fire pattern starts to form and gradually be identifiable as similar to the conflict spots in the eastern part of the Ukrainian territory, while no special pattern is found in the 2021 figures for the corresponding periods. It is notable that the eastern region comprising of five oblasts (typically translated as regions or provinces, namely Dnipropetrovsk, Donetsk, Kharkiv, Luhansk, and Zaporizhzhia) has been at the frontline of the armed conflict and subject to intense conflict hotspots since the conflict began. Given our understanding that the ongoing armed conflict is the

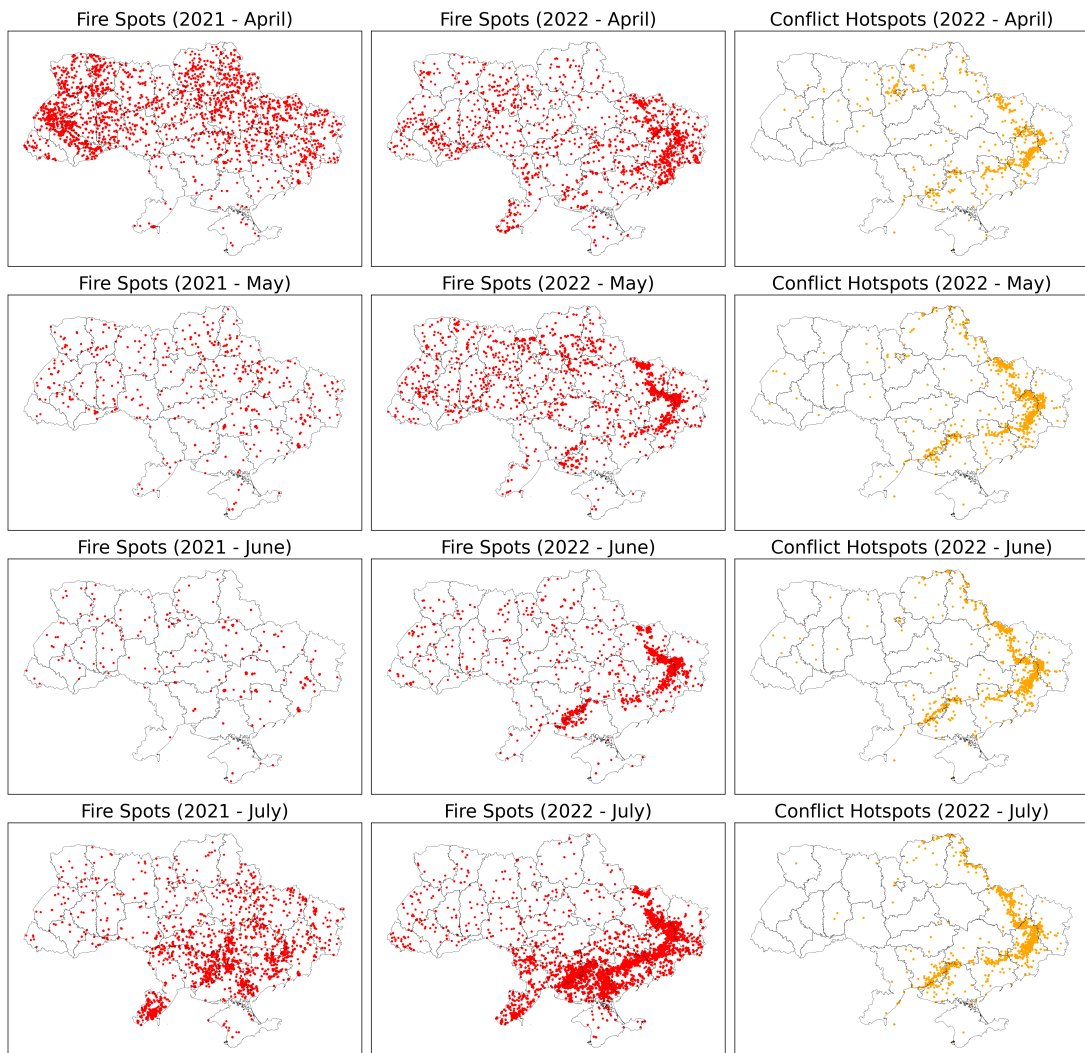


**Figure 3.8.** Satellite-captured fire spots for 2021 (1st column), 2022 (2nd column) and conflict hotspots (3rd column) in April, May, June and July. The patterns of conflict hotspots are clearly recognizable in the satellite-capture fire product from NASA FIRMS

source of explosions and smoke, it is reasonable to assume that the conflict has resulted in a significant increase in air pollution (Pereira et al., 2022), particularly in the areas directly affected by the conflict events that are detectable via VIIRS satellite products, so we would expect that S5P observations have the capability to show the resulting impacts on both overall air quality and concentrations of

NO<sub>2</sub> in the affected areas.

### **Changes of S5P NO<sub>2</sub> column levels**

Until March 2023, as reported by (Nichita and Ana, 2023), nearly 40,000 events related to the conflict were recorded across the Ukrainian territory by the ACLED project (Raleigh et al., 2010). The five oblasts Dnipropetrovsk, Donetsk, Kharkiv, Luhansk and Zaporizhzhia have been on the frontline of the Russia-Ukraine armed conflict since February 24, 2022. In these areas, shelling, artillery, and missile attacks accounted for 71% of conflict events recorded between February 24 and July 31, 2022 (Nichita and Ana, 2023). In order to evaluate the impacts of conflict events at the smallest level, we quantify changes in NO<sub>2</sub> column levels directly at the reported event location using OBS-BAU and year-to-year estimates for the corresponding pixel from S5P data, which is equivalent a 10 km<sup>2</sup>-area containing the event location (Figure 3.9).

The OBS-BAU estimates based on ORG data indicate an average increase of 0.3%, while the year-to-year estimates show a more substantial increase of 13.2%. However, when using RPRO data, we observed an 11% reduction in the OBS-BAU estimate and a 1.35% increase in the year-to-year estimate. Although there is a high level of uncertainty in estimating changes at the event location-pixel level, and the inconsistent timing between the reported conflict related events and S5P overpass may lead to an underestimation of changes in air pollution levels, the information gathered can still be useful in identifying changes in the NO<sub>2</sub> columns associated with conflict related event locations in the five oblasts.

### **3.5.2 Changes of S5P NO<sub>2</sub> levels in other affected areas**

#### **Most populous cities of Ukraine**

In the nine most populous cities in Ukraine, both the lockdown and the conflict have led to a reduction in daily anthropogenic activities. Although this reduction was expected to lower the NO<sub>2</sub> levels, as discussed in Section 4, the lockdown measures did not result in a significant reduction in NO<sub>2</sub> column levels in 2020. To quantify the changes caused by the conflict and compare them with the effects of the lockdown measures, we analysed the OBS-BAU estimate for the most

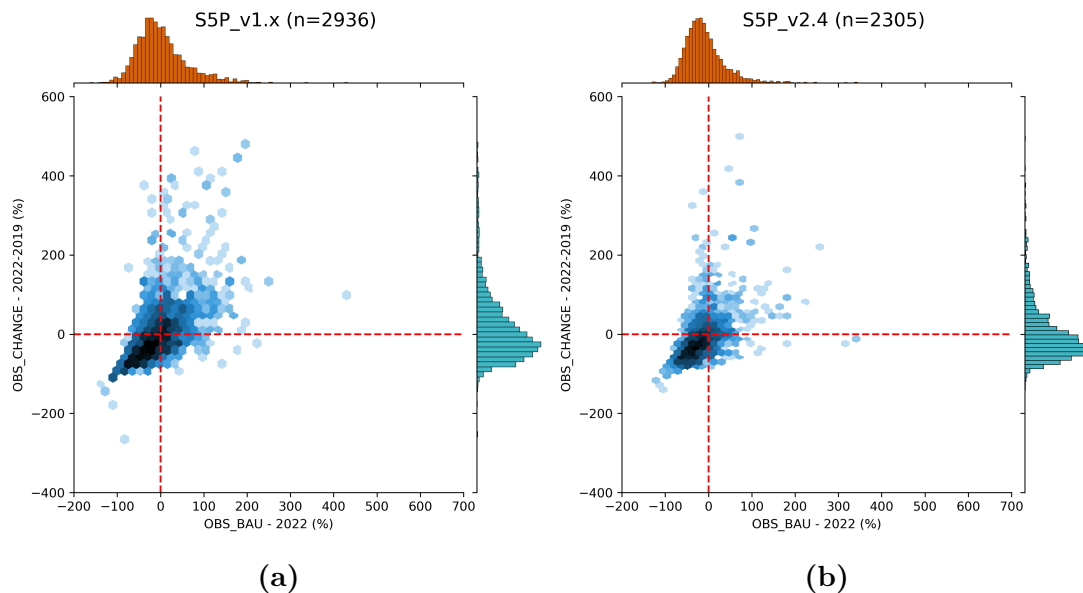


**Figure 3.9.** OBS-BAU and year-to-year estimates for the individual conflict events including air/drone strikes, armed clashes, remote explosive/landmine occurrences, shelling/artillery/missile attacks, and other forms of attacks that occurred between February 24 and July 31, 2022, for five frontline oblasts, Dnipropetrovsk, Donetsk, Kharkiv, Luhansk and Zaporizhzhia. The number of data points is denoted by (n).

populous cities in Ukraine during the strict lockdown period from April 6 to May 10 in 2020 and 2022 (Table 3.4). To avoid overwhelming plots, Figure 3.10 displays the NO<sub>2</sub> column trend lines for OBS data and BAU predictions from February to July in 2020 and 2022 for five cities (Kyiv, Kharkiv, Dnipro, Zaporizhzhia, and Kryvyi Rih) only.

Table 3.4 presents the OBS-BAU estimates corresponding to the strict lockdown period (April 6 to May 10) in 2020 and 2022 for the nine most populous cities in Ukraine. Our findings indicate that the conflict has caused more significant reductions in NO<sub>2</sub> levels, compared to the lockdown measures. While minor reductions to increases were observed during the 2020 lockdown, a consistent and continuous reduction has been noticed in most cities, during the same lockdown period (April 6 to May 10) in 2022. The average reduction across all the cities of interest, as shown in Table 3.4, is about 12.1% (based on ORG data) and 18.1%

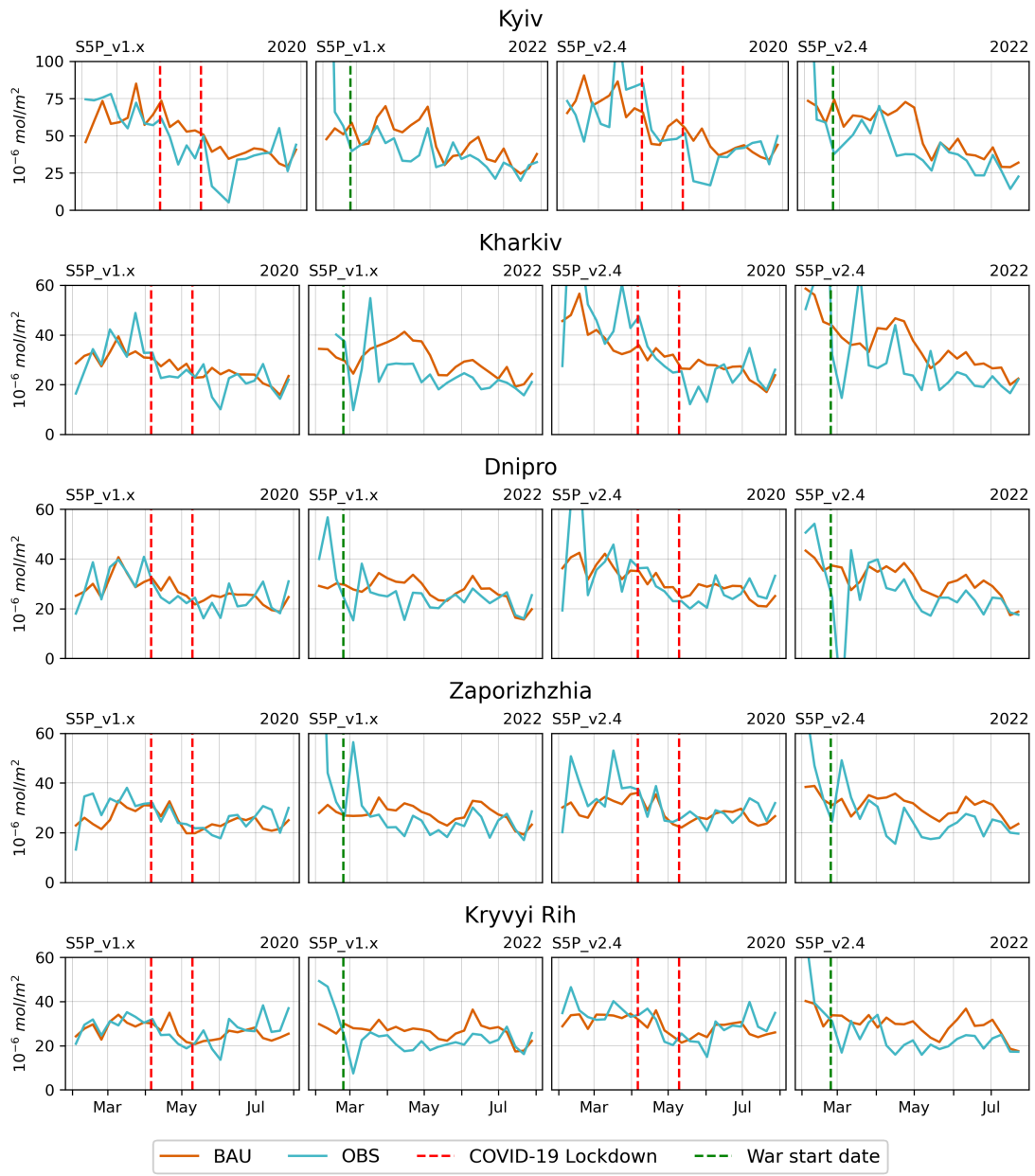


**Figure 3.10.** The trend lines of OBS and BAU S5P NO<sub>2</sub> column levels from February to July in 2020 and 2022 for five cities in Ukraine. Each row displays plots for a different city. The first and second column plots represent the ORG data (S5P version 1.x), while the third and last column plots show the RPRO data (S5P version 2.4). The first and third column plots pertain to 2020, while the second and last column plots pertain to 2022.

**Table 3.4.** The OBS-BAU estimate (in percentage) of ORG data and RPRO data for the strict lockdown period (April 6 to May 10) in 2020 and in 2022 for the nine most populous cities in Ukraine. The values are represented as mean (with standard deviation in parentheses). The mean and standard deviation in the last row were calculated across the nine cities.

City	2020 (April 6 –May 10)		2022 (April 6 –May 10)	
	ORG	RPRO	ORG	RPRO
Kyiv	-18.8 (6.5)	4.9 (17.4)	-29.3 (9.5)	-34.6 (7.6)
Kharkiv	-0.9 (10.3)	-4.9 (15.9)	-24.9 (17.9)	-29.7 (20.8)
Odessa	6.9 (12.4)	21.0 (16.4)	-7.6 (14.3)	-14.5 (9.7)
Dnipro	-6.6 (9.2)	2.8 (10.9)	-17.4 (10.0)	-19.5 (8.6)
Donetsk	28.2 (35.2)	42.0 (29.8)	3.5 (19.9)	3.2 (18.7)
Zaporizhzhia	2.5 (9.1)	9.1 (12.7)	-12.6 (13.7)	-18.4 (11.6)
Lviv	0.0 (10.9)	3.0 (8.5)	14.9 (17.9)	-3.3 (9.9)
Kryvyi Rih	-6.4 (8.7)	0.1 (9.9)	-20.8 (9.8)	-27.7 (8.1)
Mykolaiv	-0.6 (9.8)	13.8 (17.6)	-14.6 (10.1)	-18.0 (6.8)
Mean	0.5 (11.9)	10.2 (13.3)	-12.1 (13.2)	-18.1 (11.5)

(based on RPRO data). The largest reduction was observed in Kyiv, while the increase occurred in Lviv (14.9% based on ORG data) and in Donetsk (3.5% based on ORG data, 3.2% based on RPRO data).

In more than the first five months after the conflict began until the end of July 2022, an overall reduction is observed across the nine cities (see Table 3.5) with an average of 3.1% (ORG data) and 7% (RPRO data). The largest reductions in NO<sub>2</sub> levels were observed in Kyiv, with an average of 14.9% (ORG data) and 27.6% (RPRO data). Conversely, Donetsk and Lviv experienced increases in NO<sub>2</sub> levels, with both ORG and RPRO data, while in Mykolaiv only RPRO data showed the increases. The rise in Donetsk can be attributed to it being where major armed conflicts occurred during this period.

**Table 3.5.** Average OBS-BAU and year-to-year estimate (in percentage) of ORG data and RPRO data from February 24 to July 31, 2022, for the nine most populous cities in Ukraine. The values are represented as mean (with standard deviation in parentheses). The mean and standard deviation in the last row were calculated across the nine cities.

City	ORG		RPRO	
	OBS-BAU	year-to-year	OBS-BAU	year-to-year
Kyiv	-14.9 (17.3)	-30.5 (14.7)	-27.6 (12.1)	-37.3 (11.3)
Kharkiv	-3.2 (28.5)	20.7 (39.8)	-3.0 (33.3)	2.4 (23.6)
Odessa	-6.8 (15.4)	-13.6 (16.4)	-5.4 (13.0)	4.5 (61.0)
Dnipro	-12.4 (16.6)	-15.0 (21.3)	-17.6 (13.8)	-17.0 (20.5)
Donetsk	19.4 (26.6)	4.2 (21.5)	17.0 (22.8)	-9.4 (15.8)
Zaporizhzhia	-10.5 (16.4)	-15.7 (27.3)	-13.7 (14.4)	-19.1 (18.6)
Lviv	20.8 (21.9)	-9.0 (24.1)	2.2 (16.8)	-9.8 (17.3)
Kryvyi Rih	-15.5 (15.7)	-22.4 (21.7)	-17.4 (15.0)	-26.2 (42.7)
Mykolaiv	-4.8 (13.1)	-7.8 (23.5)	2.1 (14.8)	12.9 (21.9)
Mean	-3.1 (13)	-9.9 (14.1)	-7 (12.7)	-11 (15)

### Coal power plants

Besides anthropogenic activities in major cities, the contribution of CPPs to NO<sub>2</sub> concentration levels is considered to be significant in Ukraine (Lauri and Rosa, 2021). The Zaporizhzhia CPP is one of the largest emitters among CPPs in Ukraine, emitting 21,830 tonnes of NOx in 2019. Many power plants have been targeted in the conflict, and their damage or destruction has resulted in power blackouts affecting millions of people.

According to Draft Ukraine Recovery Plan, Materials of the “Energy Security” Working Group covering the period to the end of June 2022, significant damage has been reported at the Zaporizhzhia, Luhansk, and Sievierodonetsk power stations, as well as other CPPs. This damage could be expected to affect NO<sub>2</sub> levels in the areas surrounding the damaged power plants. To investigate such changes, we also compare trends in the NO<sub>2</sub> column levels between OBS data and BAU simulations for 2020 and 2022, utilizing both ORG and RPRO data as presented

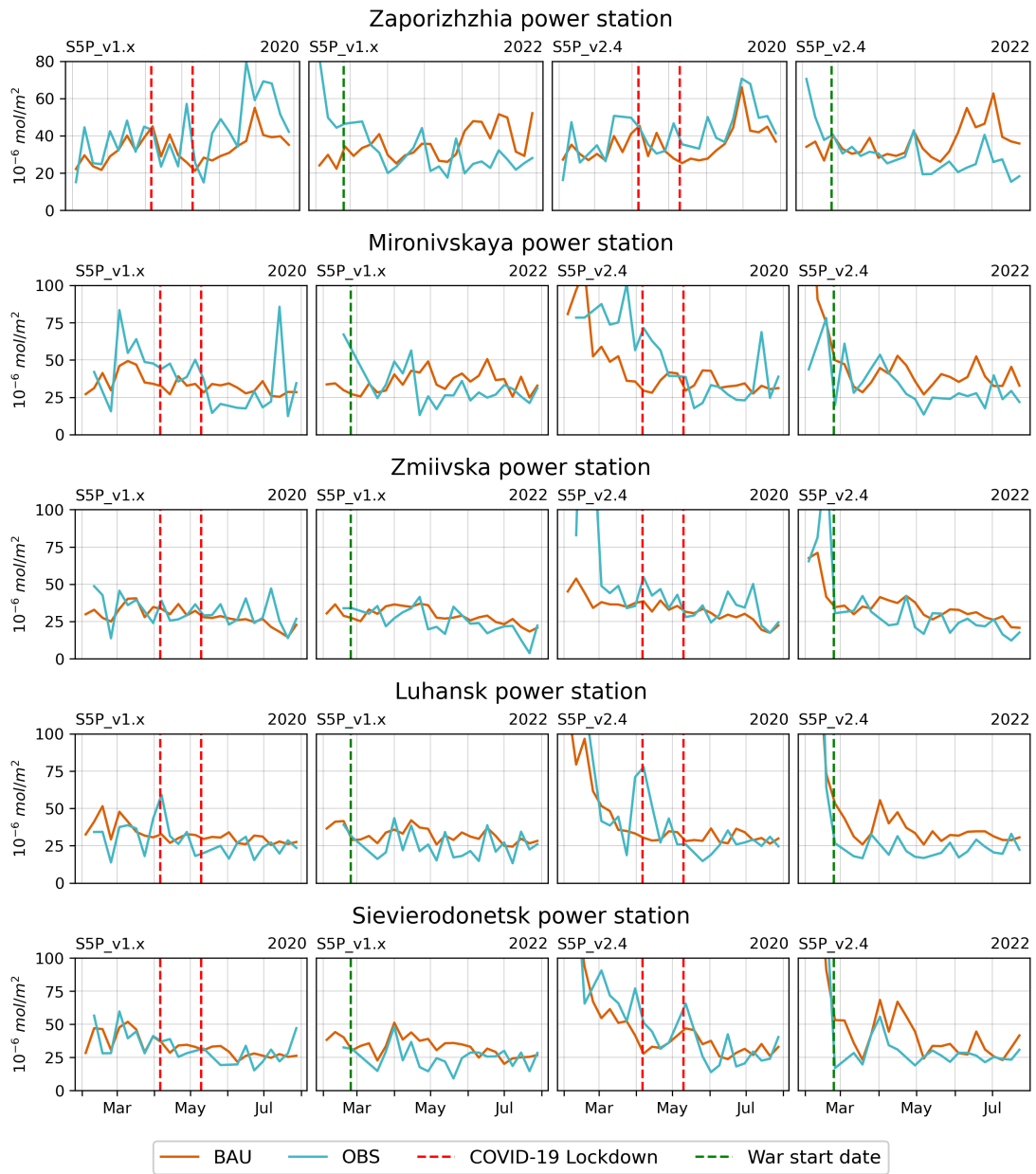


**Figure 3.11.** The trend lines for the OBS and BAU S5P NO<sub>2</sub> column levels from February to July in 2020 and 2022 are presented for selected CPPs. Each row displays plots for a different CPP. The first and second column plots represent ORG data (S5P version 1.x), while the third and last column plots show RPRO data (S5P version 2.4). The first and third column plots pertain to 2020, while the second and last column plots pertain to 2022.

in Figure 3.11. Examining an area of 10km<sup>2</sup> around each CPP, we find that, similar to previous discussions on lockdown effects, little changes are observed around most CPPs during the pandemic lockdown in 2020. However, a clear reduction is evident between the time when the conflict began and July 2022 at the Zaporizhzhia, Mironivskaya, Zmiivska, Luhansk, and Sievierodonetsk power stations. At areas surrounding other power stations, no noticeable reduction is observed.

### 3.6 Conclusion

In this study, we performed a comprehensive assessment of variations in the S5P column NO<sub>2</sub> levels in Ukraine during the COVID-19 pandemic lockdown in 2020 and the armed conflict with Russia in 2022. For this purpose, we utilized two S5P products, namely, original and reprocessing data. We first developed a weather normalization model under business-as-usual conditions, using meteorological parameters from ERA5 reanalysis, ensembled surface forecasts, and analysis NO<sub>2</sub> data from 11 CAMS models, along with other spatial and temporal features. Next, we applied the BAU prediction to estimate the change in NO<sub>2</sub> levels during the lockdown period in 2020 for the nine most populous cities in Ukraine (Kyiv, Kharkiv, Odessa, Dnipro, Donetsk, Zaporizhzhia, Lviv, Kryvyi Rih, and Mykolaiv). We extended the analysis using BAU predictions to estimate the impact of the armed conflict from February 24 to July 31, 2022, in conflict hotspot locations, the nine most populous cities, and areas surrounding selected CPPs (Zaporizhzhia, Mironivskaya, Zmiivska, Luhansk, and Sievierodonetsk) in Ukraine.

The main outcomes of the study can be summarized as follows:

- In 2020, meteorological parameters also heavily influenced the NO<sub>2</sub> tropospheric column levels, contributing to decreases in levels during the lockdown period.
- After normalizing the meteorological parameters, we found that the lockdown did not lead to lower NO<sub>2</sub> levels than the BAU prediction in 2020, although it did manage to mitigate the increase in NO<sub>2</sub> compared to the

pre-lockdown period. Our study indicates that stricter measures may need to be considered in the future to achieve a significant reduction in NO<sub>2</sub> levels in densely populated areas of Ukraine.

- We observed that satellite-capture fire data from the VIIRS product can capture the spatial patterns of the conflict related events on the ground. From this product, conflict location patterns are clearly represented during the April–July 2022 period.
- Upon examining changes in NO<sub>2</sub> levels at conflict hotspots at the location-pixel level, we observed changes ranging from an 11% reduction to a slight increase of 0.3% when comparing the OBS to BAU predictions using RPRO and ORG data, respectively.
- During the strict lockdown period from April 6 to May 10, 2022, the reduction in NO<sub>2</sub> levels in the nine most populous cities was more significant compared to 2020. Across most cities, an average reduction of 12.1% (ORG data) and 18.1% (RPRO data) was observed. However, it is worth noting that Lviv and Donetsk showed an increase in NO<sub>2</sub> levels during this period.
- From February 24 to July 31, 2022, the nine most populous cities in Ukraine experienced an overall reduction of 3.1% (ORG data) and 7% (RPRO data) in NO<sub>2</sub> levels. The most significant reduction was observed in Kyiv, with an average decrease of 14.9% (ORG data) and 27.6% (RPRO data). However, in contrast, NO<sub>2</sub> levels increased in Lviv, Donetsk and Mykolaiv during this period.
- The conflict has resulted in damage to several CPPs, which are considered as major sources of NO<sub>2</sub> emissions in the country. Our analysis indicates a clear reduction in NO<sub>2</sub> levels in the areas closely surrounding Zaporizhzhia, Mironivskaya, Zmiivska, Luhansk, Sievierodonetsk CPPs.
- By utilizing the OBS-BAU estimate for both ORG data and RPRO data to analyse NO<sub>2</sub> variations during the 2022 conflict, we found that discrepancies resulting from changes in the processor during the S5P lifetime in ORG data might lead to a slight underestimation of NO<sub>2</sub> reductions. Specifically, we

observed a smaller decrease using ORG data (3.1%) than with RPRO data (7%) in the most populous cities of Ukraine.

The consideration of meteorological effects is crucial in regulating pollution levels. Neglecting these effects could introduce errors in quantifying actual air quality changes attributed to an intervention event. For future studies assessing the impacts of conflict in Ukraine on air quality, it will be essential to account for meteorological variability to achieve genuine and quantitative estimates.

NO<sub>2</sub> is a significant precursor to tropospheric O<sub>3</sub> and also affects the lifetime of methane (CH<sub>4</sub>) (Akimoto and Tanimoto, 2022). Additionally, it has the potential to serve as an indicator for monitoring CO<sub>2</sub> emissions (Miyazaki and Bowman, 2023). In future studies, it would be valuable to explore how changes in NO<sub>2</sub> levels during conflict could impact O<sub>3</sub> and CH<sub>4</sub> concentrations in Ukraine as both are important short-lived climate pollutants that contribute to positive radiative forcing, thereby exacerbating global warming.

# 4 Japan's case study

## 4.1 Introduction

Nitrogen dioxide ( $\text{NO}_2$ ) is an important air pollutant that raises significant concerns due to its negative effects on human health (Hamra et al., 2015). Additionally, it serves as a crucial precursor to tropospheric ozone ( $\text{O}_3$ ), along with volatile organic compounds (VOCs) (Akimoto and Tanimoto, 2022). Nitrogen oxides ( $\text{NOx} = \text{NO} + \text{NO}_2$ ), carbon monoxide (CO) and non-methane volatile organic compounds (NMVOCs) have an influence on the methane ( $\text{CH}_4$ ) lifetime by affecting the atmospheric mixing ratio of hydroxyl radicals ( $\text{OH}$ ) (Akimoto and Tanimoto, 2022), which act as a primary sink for  $\text{CH}_4$  (Turner et al., 2019). Both  $\text{O}_3$  and  $\text{CH}_4$  are short-lived climate pollutants (SLCPs) that contribute to positive radiative forcing, thereby intensifying global warming (Akimoto and Tanimoto, 2022). Moreover, owing to its short lifetime in the atmosphere and significant signal compared to carbon dioxide ( $\text{CO}_2$ ),  $\text{NO}_2$  possesses the potential to serve as an indicator for monitoring localized fossil fuel  $\text{CO}_2$  emissions (Miyazaki and Bowman, 2023).

In 2020, the implementation of COVID-19 social distancing policies in multiple countries led to a significant decrease in human activities worldwide (de Palma et al., 2022). While the general anticipation was for a reduction in  $\text{NO}_2$  emissions in many cities due to the decline in anthropogenic activities (Bauwens et al., 2020; Barré et al., 2021; Cooper et al., 2022), the response of  $\text{O}_3$  and  $\text{CH}_4$  has been unexpected.

Increased levels of  $\text{O}_3$  have been observed in northern Europe, China, and South Africa as a consequence of the COVID-19 lockdown, according to sensitivity simulations conducted using the MIROC-CHASER global chemical transport model (Miyazaki et al., 2021). This rise in  $\text{O}_3$  can be attributed to the general

reduction in NOx, which enhances O3 production by reducing NO titration in areas with high levels of NOx pollution or VOC-limited areas (Akimoto and Tanimoto, 2022). Furthermore, meteorological effects have played a significant role in the changes observed in O3 levels between 2020 and the reference year (Ordóñez et al., 2020; Liu et al., 2021). Despite accounting for the influence of weather conditions, significant variations in O3 level estimates have been reported across studies, particularly in European countries (Ordóñez et al., 2020; Grange et al., 2021), and China (Liu et al., 2021; Shi et al., 2021). The presence of sunlight is essential for the O3 generation in response to the decrease in NOx during the lockdown period. As a result, the lack of sunny conditions in specific urban areas at the time of the atmospheric response to NO2 reduction may have led to differing time delays before observable changes in O3 levels occurred (Grange et al., 2021) (Grange et al. 2021).

In 2020, during the COVID-19 pandemic, global CH4 emissions experienced a significant growth rate, which was contrary to the expected decrease in anthropogenic CH4 emissions due to the implementation of lockdown measures (Peng et al., 2022). In 2020, anthropogenic CH4 emissions only slightly decreased compared to 2019, while wetland emissions rose sharply. This increase in wetland emissions was likely influenced by unusually warm and wet weather in the Northern Hemisphere (Peng et al., 2022), which could be connected to the impact of climate change (Zhang et al., 2023). Apart from the variation in CH4 emission itself, it was found that the decrease in hydroxyl radical (OH) concentration due to changes in air pollutants like NOx, CO, and NMVOCs during the COVID-19 pandemic mainly accounted for approximately half ( $53 \pm 10\%$ ) of the observed global CH4 level growth in 2020 (Peng et al., 2022). A similar finding regarding the effect of NOx, CO, and NMVOCs emission changes on the 2020 methane levels is reported by (Stevenson et al., 2022). However, other studies using Greenhouse gases Observing SATellite (GOSAT) observations indicated that most of observed increase in atmospheric CH4 during 2020 and 2021 can be attributed to increased CH4 emission itself (Qu et al., 2022; Feng et al., 2023). Although CH4 has a long estimated lifetime of 8-10 years and has mostly been discussed at the global level, it is important to note that policies and approaches to address CH4 emissions may vary locally.

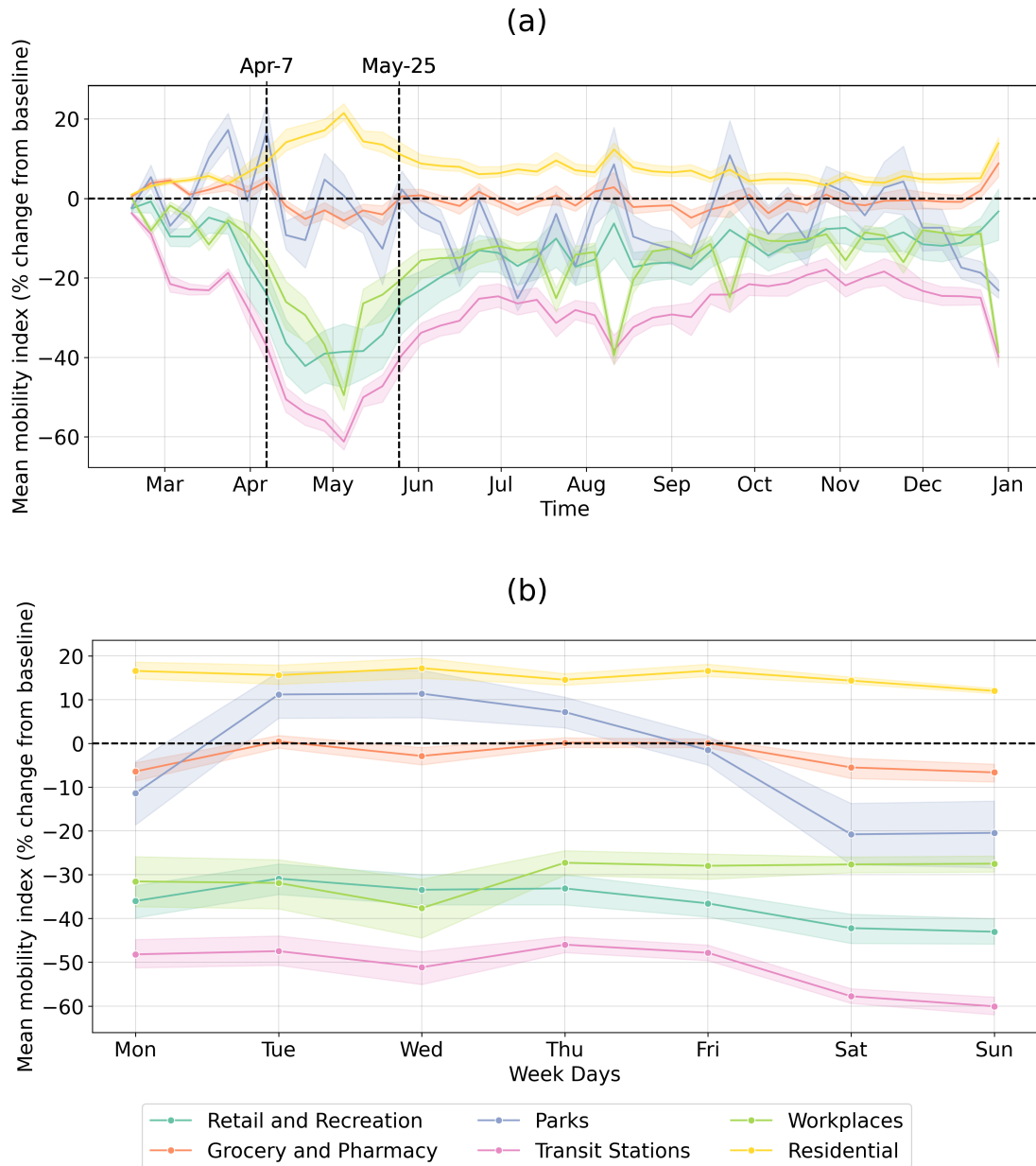


**Figure 4.1.** Mobility changes for 6 prefectures in Japan (Aichi, Fukuoka, Tokyo, Osaka, Kyoto, and Hyogo) in 2020 based on Google's mobility indices for time-series (a) and days of the week (b)

In 2020, Japan also experienced the impact of the COVID-19 pandemic, and in response to prevent the virus's spread, a state of emergency was declared from April 7 to May 25. This measure resulted in the suspension of various economic activities and imposed restrictions on people's mobility. As a consequence, there was a significant decline (Figure 1) in a unique weekend movement trend (Damiani et al., 2022).

Although the primary aim of the lockdown was not specifically to address air pollution and greenhouse gas emissions, the implementation of these measures offers valuable insights for atmospheric modelling. It provides practical knowledge and first-hand experience to develop more efficient strategies for mitigating air pollution and reducing greenhouse gas emissions in the future (Grange et al., 2021). It is important to note that the changes in air pollutants during this period varied across regions and were strongly influenced by meteorological conditions. Performing a regional analysis of these changes can provide evidence to support the formulation of appropriate regional policies in the future. In this study, our objective is to evaluate the impact of changes in anthropogenic activities during the COVID-19 pandemic (from April 7 to December 31) on NO<sub>2</sub>, O<sub>3</sub>, CO and CH<sub>4</sub> in metropolitan areas (MAs) of Japan in 2020, which have not been thoroughly investigated in previous studies.

In the first phase (Section 4.2), we gathered data from ground observations, satellite sources, and biogeochemical model simulations. Subsequently, we constructed a weather normalization model under business-as-usual (BAU) conditions utilizing machine learning techniques, incorporating meteorological, spatial, and temporal predictors (Section 4.3). We investigated variations in air pollution levels by analysing the BAU predictions alongside additional data in Section 4.4. Lastly, we provided discussions in Section 4.5, while in Section 4.6, we present our study's findings, conclusions, and recommendations for future policy considerations.

## 4.2 Data

### 4.2.1 Study area

Prior research primarily focused on assessing the impact of pandemic lockdown measures on air quality within the Greater Tokyo Area, being the most densely populated metropolitan area globally (Damiani et al., 2022; Zoran et al., 2023). Nevertheless, there's a notable absence of similar analyses for other MAs. Our study covers 14 MAs in Japan, extending from Sapporo in the north to Kagoshima in the south, as depicted in Figure 2. We focus on these metropolitan areas due to their housing of Japan's highly populated and vibrant cities, which are intricately connected with human activities and air pollution in Japan.

### 4.2.2 Ground observation

To acquire air quality data, we gathered ground observations for NO<sub>2</sub>, O<sub>3</sub>, CO, and CH<sub>4</sub> from the air quality monitoring data archive published by the National Institute for Environmental Studies (NIES). These observations spanned a ten-year period from 2010 to 2020 and were collected from 1,180 stations for NO<sub>2</sub>, 835 stations for O<sub>3</sub>, 383 stations for CH<sub>4</sub>, and 237 stations for CO. The study utilized two types of stations: roadside air monitoring stations (RsAMS), which are placed in areas prone to air pollution from vehicle exhaust caused by traffic congestion, like intersections, roads, and near road edges, and ambient air monitoring stations (AAMS), which are established to assess air pollution in general living spaces such as residential areas. These station types have been categorized by NIES, and the data can be readily acquired from the original downloadable dataset.

Apart from air quality data, we incorporated ground observations of meteorological data from Japan Meteorological Agency (JMA) as input features for the BAU models used in the study. Specifically, we obtained daily records from 52 weather stations located within the same 14 MAs. At each weather station, we gathered temperature, wind direction and speed, local atmospheric pressure, and relative humidity, as suggested by (Grange et al., 2021). The corresponding meteorological parameters were extracted from the nearest weather observation site for each air quality station.

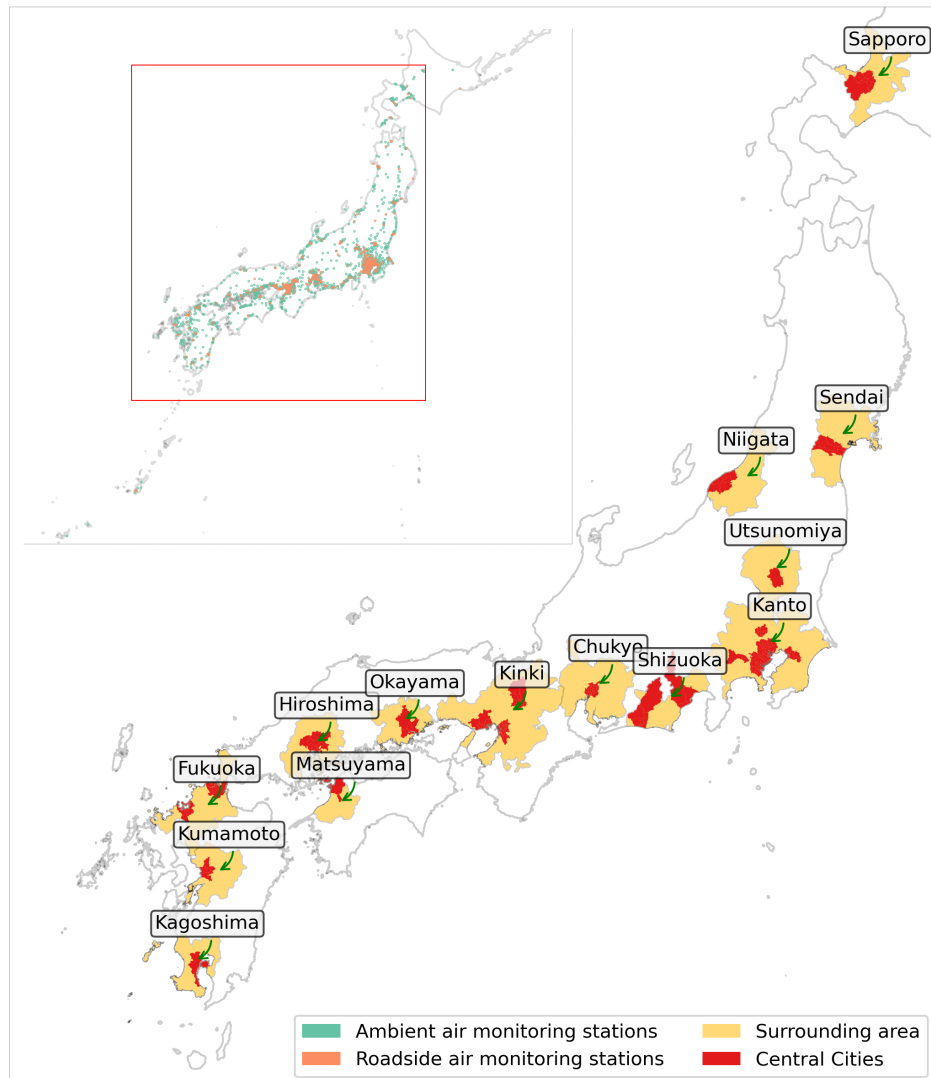


**Figure 4.2.** The locations of 14 metropolitans' areas and the distribution of ground observations for air quality monitoring in Japan

### 4.2.3 ERA5 reanalysis dataset

Alongside the weather data collected from the ground stations in the NIES database, for the features of the BAU models, we incorporated additional daily data pertaining to boundary layer height, total cloud cover, downward solar radiation (SR), and total precipitation, as recommended by (Shi et al., 2021). This supplementary information was sourced from the ERA5 reanalysis dataset (ERA5 hourly data on single levels from 1940 to the present) obtained from the Climate Data Store of the Copernicus Climate Change Service. Additionally, the ERA5 2m temperature variable (T2M) and SR will be utilized to assess the variation of sunny conditions during both the lockdown and post-lockdown periods within the study area. The original ERA5 data possesses a spatial resolution of  $0.25^\circ \times 0.25^\circ$ .

### 4.2.4 Sentinel 5P TROPOMI

In this study, we utilized the Sentinel 5P (S5P) Tropospheric Monitoring Instrument (TROPOMI) data to evaluate the tropospheric formaldehyde-to-NO<sub>2</sub> ratio (FNR) specifically for the year 2020. This ratio serves as a key indicator for the sensitivity of tropospheric ozone production. The tropospheric NO<sub>2</sub> and formaldehyde (HCHO – as a proxy for NMVOCs) data was obtained from the S5P L3 product “OFFL/L3\_NO2” (based on processor version 1.2.x and 1.3.x) and “OFFL/L3\_HCHO” (based on processor version 1.1.x) collections from Google Earth Engine, respectively. To generate the comprehensive L3 S5P product, each operational level (L2) product underwent preprocessing and mosaicking using the harpconvert tool. The low-quality pixels were filtered out in L3 NO<sub>2</sub> product by excluding those with AQ (Air Quality) values below 75% for the band “tropospheric\_NO2\_column\_number\_density”. The resulting data, ready for download, is available with a spatial resolution of about  $1 \times 1 \text{ km}^2$ .

### 4.2.5 Biogeochemical modelled CH<sub>4</sub> budget

In our assessment of CH<sub>4</sub> emission variations, with a specific focus on emissions from natural sources such as wetlands, we utilized CH<sub>4</sub> budget data obtained from the Vegetation Integrative Simulator for Trace gases (VISIT) (Ito et al.,

2019). VISIT is a biogeochemical model that takes into account historical land use and climatic conditions to estimate CH<sub>4</sub> emissions (Ito et al., 2019). The CH<sub>4</sub> budgets generated by the VISIT model are now available and accessible through the Global Environmental Database provided by NIES, Japan (Ito et al., 2019). We utilized the global data versions “Ver.2021.1\_CH4Wetl\_Cao” (Ito, 2021a), and “Ver.2021.1\_CH4Wetl\_WH” (Ito, 2021b), which incorporate Cao scheme (Cao et al., 1996), and Walter and Heimann scheme (WH scheme) (Walter and Heimann, 2000), to estimate CH<sub>4</sub> emission for each MA, which offers CH<sub>4</sub> emission information at a spatial resolution of 0.5° × 0.5°.

## 4.3 Method

### 4.3.1 Business-as-usual (BAU) modelling

To accurately quantify the actual change in the levels of the four pollutants, we developed a weather normalization model under BAU conditions using machine learning. This model was specifically designed to simulate pollutant levels without the influence of COVID-19 restriction measures, using meteorological, spatial, and temporal features as inputs. The meteorological predictors utilized in our model include ground observation data such as temperature, wind direction and speed, local atmospheric pressure, and relative humidity. Additionally, we incorporated data from the ERA5 reanalysis dataset, which comprises boundary layer height, total cloud cover, downward solar radiation, and total precipitation. Temporal predictors included the Julian date (the number of days since January 1) and the day of the week. Furthermore, latitude and longitude coordinates of each station were utilized as spatial predictors. To develop the weather normalization models for each pollutant at both AAMS and RsAMS, we utilized data from the years 2016 to 2019, which offers a comprehensive timeframe to account for the diverse air pollution concentration fluctuations experienced across various meteorological conditions. Extending the period, such as from 2010 to 2019, would not accurately represent recent air quality trends due to the impact of past air pollution reduction policies. Conversely, a shorter timeframe, such as the pre-lockdown period months would not adequately capture the full range of

meteorological variations. Overall, four separate weather normalization models were developed for each pollutant ( $\text{NO}_2$ ,  $\text{O}_3$ ,  $\text{CO}$ , and  $\text{CH}_4$ ), taking into account the specific station type (RsAMS and AAMS).

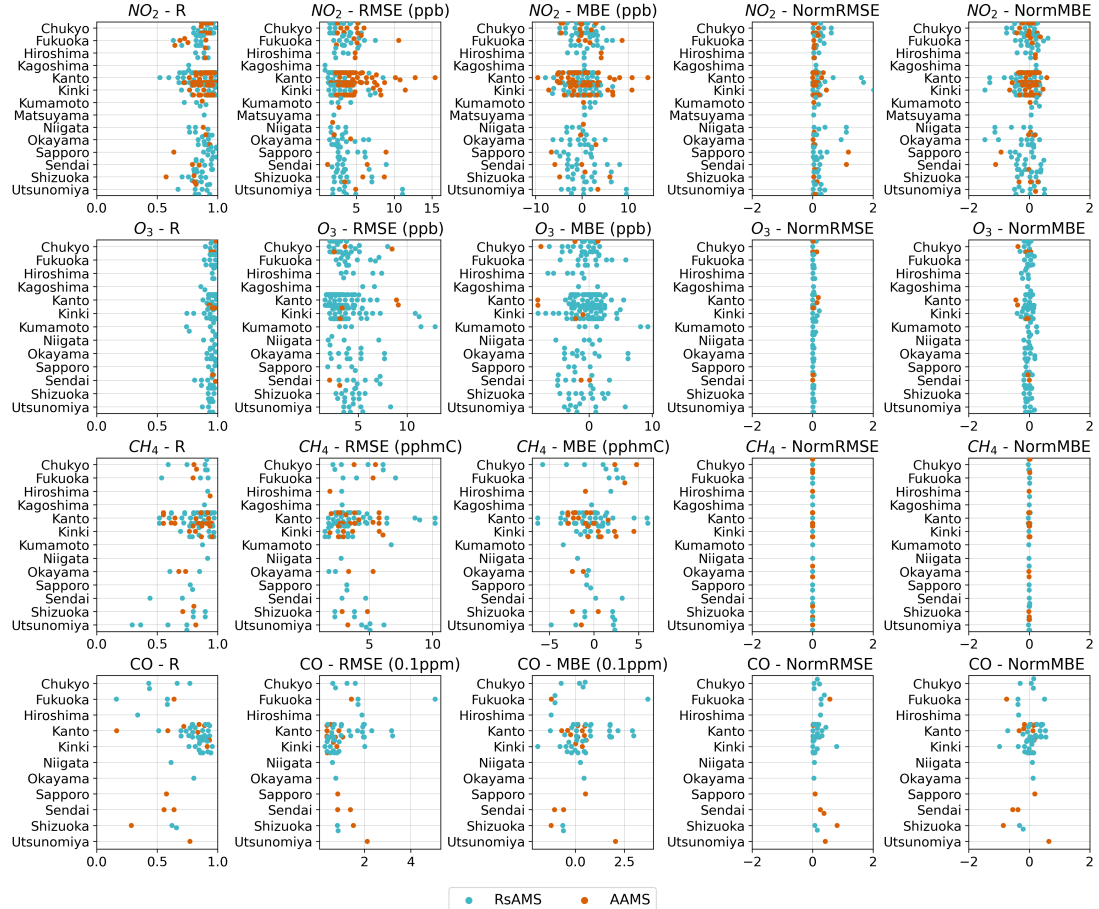


**Figure 4.3.** The details score of each station on the test set. For each station on the test set, we calculated the following scores and display it in this figure: Pearson correlation coefficient (R), root mean square error (RMSE), normalized root mean square error (NormRMSE) and mean bias error (MBE), normalized mean bias error (NormMBE)

We employed the LightGBM machine learning model (Ke et al., 2017), a gradient boosting decision tree algorithm, to construct the BAU model using the aforementioned predictors. To fine-tune the model's hyperparameters, we utilized Fast and Lightweight AutoML Library (FLAML) (Wang et al., 2021), a

**Table 4.1.** The performance of BAU model on the test set (30% station data) with the following metrics: Pearson correlation coefficient (R), root mean square error (RMSE), normalized root mean square error (NormRMSE) and mean bias error (MBE), normalized mean bias error (NormMBE). For the normalized MBE and RMSE, we normalize values for each station and then compute the mean

Pollutants	Station type	R	RMSE	NormRMSE	MBE	NormMBE
NO <sub>2</sub>	AAMS	0.89	3.13	0.15	-0.12	-0.07
	RsAMS	0.88	4.84	0.10	0.30	-0.03
O <sub>3</sub>	AAMS	0.96	3.75	0.02	-0.37	-0.02
	RsAMS	0.96	4.92	0.06	-3.18	-0.16
CO	AAMS	0.73	0.84	0.17	0.00	-0.07
	RsAMS	0.77	1.23	0.13	0.39	0.04
CH <sub>4</sub>	AAMS	0.82	3.75	0.00	-0.29	0.00
	RsAMS	0.80	3.82	0.00	-0.26	0.00

lightweight library specifically designed for accurately identifying optimal hyperparameters for models. During the training process, we utilized 70% of the station data within each metropolitan area (MA), while the remaining 30% was reserved for validating the model's performance. Both the training and test data sets were randomly selected for each MA, ensuring unbiased representation across the dataset.

In order to evaluate the performance of the BAU model we utilized the following metrics mean bias error (MBE), normalized mean bias error (NormMBE), root mean square error (RMSE), normalized root mean square error (NormRMSE) and Pearson correlation coefficient (R) as suggested by (Grange et al., 2021). The detailed results are presented in Figure 3 for each pollutant and station, average scores are shown in Table 1. In general, the model demonstrated strong performance with high R values (mostly R > 0.8) and low MBE and RMSE scores when applied to the test set for NO<sub>2</sub>, O<sub>3</sub>, and CH<sub>4</sub>. Regarding CO, the model achieved a satisfactory R value (R > 0.73).

### 4.3.2 Experiments design

Our aim is to assess the alterations in NO<sub>2</sub> levels within 14 MAs during both the lockdown and post-lockdown periods in 2020. We also intend to explore how changes in NO<sub>2</sub> may influence the shifts in O<sub>3</sub> and CH<sub>4</sub> levels in each of these timeframes. Notably, we were encouraged to undertake this investigation by an observation of an unusual O<sub>3</sub> response to NO<sub>2</sub> reduction in the Greater Tokyo Area (Damiani et al., 2022), prompting me to study the response of O<sub>3</sub> and CH<sub>4</sub> in all 14 MAs across Japan.

We conducted three experiments to assess the impact of NO<sub>2</sub> changes on O<sub>3</sub> and CH<sub>4</sub> levels. In the first experiment, we focused solely on quantifying the change in NO<sub>2</sub> levels using the time series observations and "OBS-BAU" estimate which involved subtracting the BAU prediction from the observed data (OBS). In the second experiment, we expanded the analysis to include O<sub>3</sub>, incorporating additional variables from the ERA5 (temperature – T2M and SR) and S5P datasets (FNR and HCHO). The last experiment included CH<sub>4</sub>, incorporating the "OBS-BAU" estimate for CH<sub>4</sub> and NO<sub>2</sub>, as well as the "OBS-BAU" estimate for CO and simulated CH<sub>4</sub> emissions from wetlands using the VISIT model.

For the experiments, we selected April 7 to May 25 as the lockdown period, August 1–31 as the post-lockdown period for O<sub>3</sub> analysis, and June 1 to December 31 for CH<sub>4</sub> analysis. We selected these timeframes to better understand how the four air pollutants changed in response to the unforeseen COVID-19 lockdown measures and the period after the lockdown.

## 4.4 Results

### 4.4.1 NO<sub>2</sub> level changes

We initially examined the monthly trend of observed NO<sub>2</sub> concentration levels across 1,180 stations in the 14 MAs from 2010 to 2019, and we compared these trends with the NO<sub>2</sub> levels observed during the lockdown in 2020 as depicted in Figure 4a. The results indicate that the actual reduction in NO<sub>2</sub> levels during the lockdown in 2020 is lower than the trend observed during 2010-2019, specifically 2.7 ppb for RsAMS and 2.2 ppb for AAMS. This implies that the NO<sub>2</sub> levels

observed during the lockdown were equivalent to those in 2023 for RsAMS and 2025 for AAMS, based on the trend observed during 2010-2019.

Prior studies have indicated the importance of considering meteorological factors when evaluating the effects of intervention measures (Ordóñez et al., 2020; Grange et al., 2021; Shi et al., 2021). In order to accurately assess the impact of the lockdown while isolating the effects of weather conditions, we computed the "OBS-BAU" estimates for all MAs as depicted in Figure 4b. Additionally, Figure 4c presents the complete time series of NO<sub>2</sub> levels in 2020 (OBS), the expected levels without the lockdown (BAU), and the average data from 2016-2019 for four MAs (Kanto, Kinki, Chukyo, Fukuoka). We only show the figures for four MAs to avoid overwhelming complexity and to provide a more manageable representation of the figures.

**Table 4.2.** OBS-BAU estimates for NO<sub>2</sub> during the lockdown (April 7 to May 25) and post-lockdown (August 1 to 31). For timeseries estimate, we considered all days of the week. However, when considering weekday, we only included Monday to Friday, while for weekends, we only accounted for Sunday and Saturday. The values are represented as mean (standard deviation)

Station type	Lockdown (April 7 –May 25)			Post-lockdown (August 1–31)		
	Timeseries (%)	Weekday (%)	Weekend (%)	Timeseries (%)	Weekday (%)	Weekend (%)
AAMS	-14.5 (12.1)	-12.9 (14.3)	-18.4 (8.6)	-10.2 (7.3)	-6.8 (7.8)	-17.2 (8.3)
RsAMS	-19.1 (13.5)	-18.0 (14.2)	-21.9 (13.9)	-18.1 (11.2)	-13.6 (12.3)	-27.4 (10.0)

Overall, NO<sub>2</sub> levels exhibited a decline across most MAs. The decline in emissions was particularly significant in RsAMS compared to AAMS in most MAs, with an average reduction of 19.1% and 14.5% respectively. However, these reductions were smaller compared to those observed in European cities (Barré et al., 2021; Grange et al., 2021). Additionally, we observed that the reduction in NO<sub>2</sub> levels during weekends was more significant than on weekdays, primarily due to a substantial decrease in mobility during weekends compared to weekdays (refer to Figure 1b). During the lockdown the average reduction in NO<sub>2</sub> levels for AAMS was 12.9% on weekdays and 18.4% on weekends. As for RsAMS, the average reduction stood at 18% on weekdays and 21.9% on weekends. For most MAs,

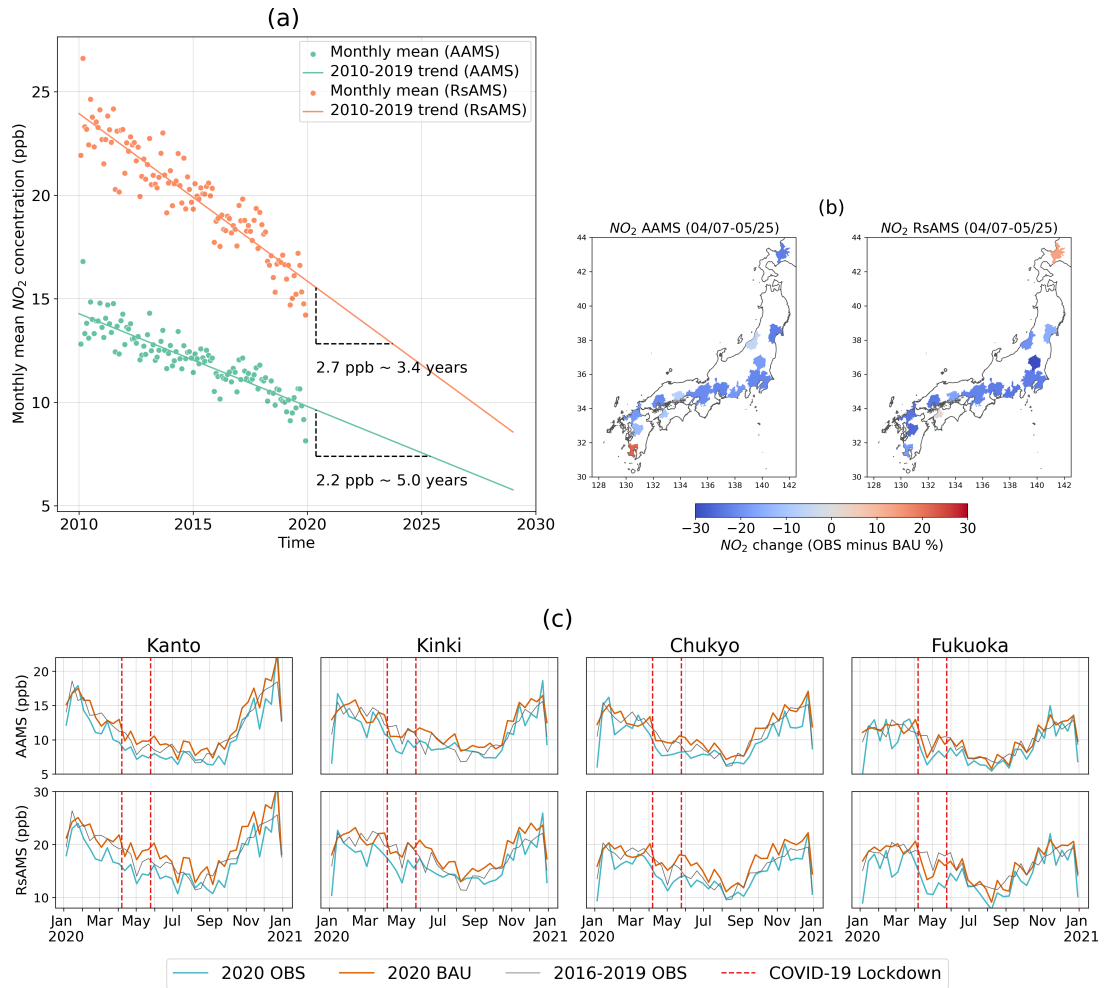


**Figure 4.4.** (a) Mean ground observation trend with the reduction in  $\text{NO}_2$  due to the lockdown in 2020 for AAMS and RsAMS. (b) Map visualization of the “OBS-BAU” estimate for  $\text{NO}_2$  during the lockdown period. (c) The 7-day rolling mean of 2020 observation (OBS), BAU prediction (BAU), and mean level of  $\text{NO}_2$  from 2016 to 2019 for 4 MAs

even the lockdown has been lifted in the end of May 2020, the  $\text{NO}_2$  level still continue to decline until the end of December 2020. This ongoing decrease may be attributed to the sustained reduction in mobility trends from the period of the lockdown through the end of 2020 (as illustrated in Figure 1a). These findings

are summarized in Table 2 and Table 3.

#### 4.4.2 O<sub>3</sub> level changes

In this experiment, we investigated various parameters to gain a better understanding of the changes in O<sub>3</sub> in response to the reduction of NO<sub>2</sub> caused by COVID-19 social distancing policies. Alongside the "OBS-BAU" estimates, we examined standardized anomalies of T2M and SR between 2020 and 2016-2019 period, S5P FNR in 2020, and changes in S5P HCHO between 2020 and 2019. These parameters were analyzed for two distinct periods: the lockdown period and the post-lockdown (August 1 –31), 2020.

##### Changes during the lockdown period

During the lockdown period (April 7 to May 25), we observed a slight change in O<sub>3</sub> levels across most MAs (Figure 5 second row and Figure 6). On average, there was a reduction of 2.3% in AAMS and 0.6% in RsAMS, as indicated in Table 2. Although the overall trend showed a decrease, we did find instances of increased O<sub>3</sub> levels in certain MAs, particularly in RsAMS such as Kanto (1.6%), Kinki (2.2 %), and Fukuoka (3.5 %), as depicted in Figure 5 (second row). Moreover, we have observed the existence of an "ozone weekend effect" in the changes of O<sub>3</sub> levels, indicating higher increase in O<sub>3</sub> mixing ratios during weekends in comparison to weekdays (Akimoto and Tanimoto 2022). This effect was observed in the "OBS-BAU" estimates for RsAMS in Fukuoka (increased 8.8% - weekends, 1.3% - weekdays) and Kinki (increased 4.9% - weekends, 1.2% - weekdays). The observed slight decrease in O<sub>3</sub> levels across most MAs in Japan contrasts with the trends observed in many other major cities worldwide (Shi et al., 2021; Grange et al., 2021), where significant increases in O<sub>3</sub> levels have been observed. For instance, after accounting for weather effects, notable increases have been reported in Beijing (28.9 %), Wuhan (44.5 %), Milan (66.8 %) Rome (55.8 %), New York (17.4 %), Los Angeles (14.8 %), and Delhi (26.2 %) by (Shi et al., 2021).

To explore this variation further, we analyzed the disparity in T2M and SR between the corresponding period of 2020 and the reference period 2016-2019 as

shown in Figure 5 (3rd row). We observed small positive SR anomalies in the southeast region of Japan and negative SR anomalies in the northeast region. Additionally, across the entire country, negative T2M anomalies were observed. The presence of negative T2M anomalies and fluctuating SR levels suggests that the prevailing weather conditions during this period impeded the production of O<sub>3</sub>.

**Table 4.3.** OBS-BAU estimates for O<sub>3</sub> during the lockdown (April 7 to May 25) and post-lockdown (August 1 to 31). For timeseries estimate, we considered all days of the week. However, when considering weekday, we only included Monday to Friday, while for weekends, we only accounted for Sunday and Saturday. The values are represented as mean (standard deviation)

Station type	Lockdown (April 7 –May 25)			Post-lockdown (August 1–31)		
	Timeseries	Weekday	Weekend	Timeseries	Weekday	Weekend
	(%)	(%)	(%)	(%)	(%)	(%)
AAMS	-2.3 (2.7)	-2.7 (3.2)	-1.2 (2.7)	2.2 (15.6)	3.2 (15.3)	0.0 (18.8)
RsAMS	-0.6 (2.7)	-1.4 (2.7)	1.4 (3.7)	8.9 (10.7)	8.9 (12.3)	8.6 (12.7)

### Changes during the August, 2020

In August 2020, the NO<sub>2</sub> levels continued to decline in all MAs, albeit at a slower rate compared to the lockdown period, as shown in Table 2. However, during this period, we observed a more noticeable increase in O<sub>3</sub> levels across most MAs compared to the lockdown. On average, there was a 8.9% increase for RsAMS and a 2.2% increase for AAMS. Notably, the increase in O<sub>3</sub> levels during weekends was more significant than on weekdays in Niigata, Okayama, Kinki and Sendai. Specifically, For AAMS of Niigata, O<sub>3</sub> levels experienced a 9.4% increase on weekends and a 5.8% increase on weekdays. In RsAMS of Okayama, O<sub>3</sub> levels saw a 13% increase on weekends, exceeding the 10.6% increase observed on weekdays. Similarly, in AAMS in the Kinki region, O<sub>3</sub> levels exhibited a weekend increase of 19.8%, surpassing the 17.4% increase observed on weekdays. In Sendai, the increase during weekends was even more pronounced, with a 15.6% increase for AAMS and a 22% increase for RsAMS, whereas on weekdays the increase

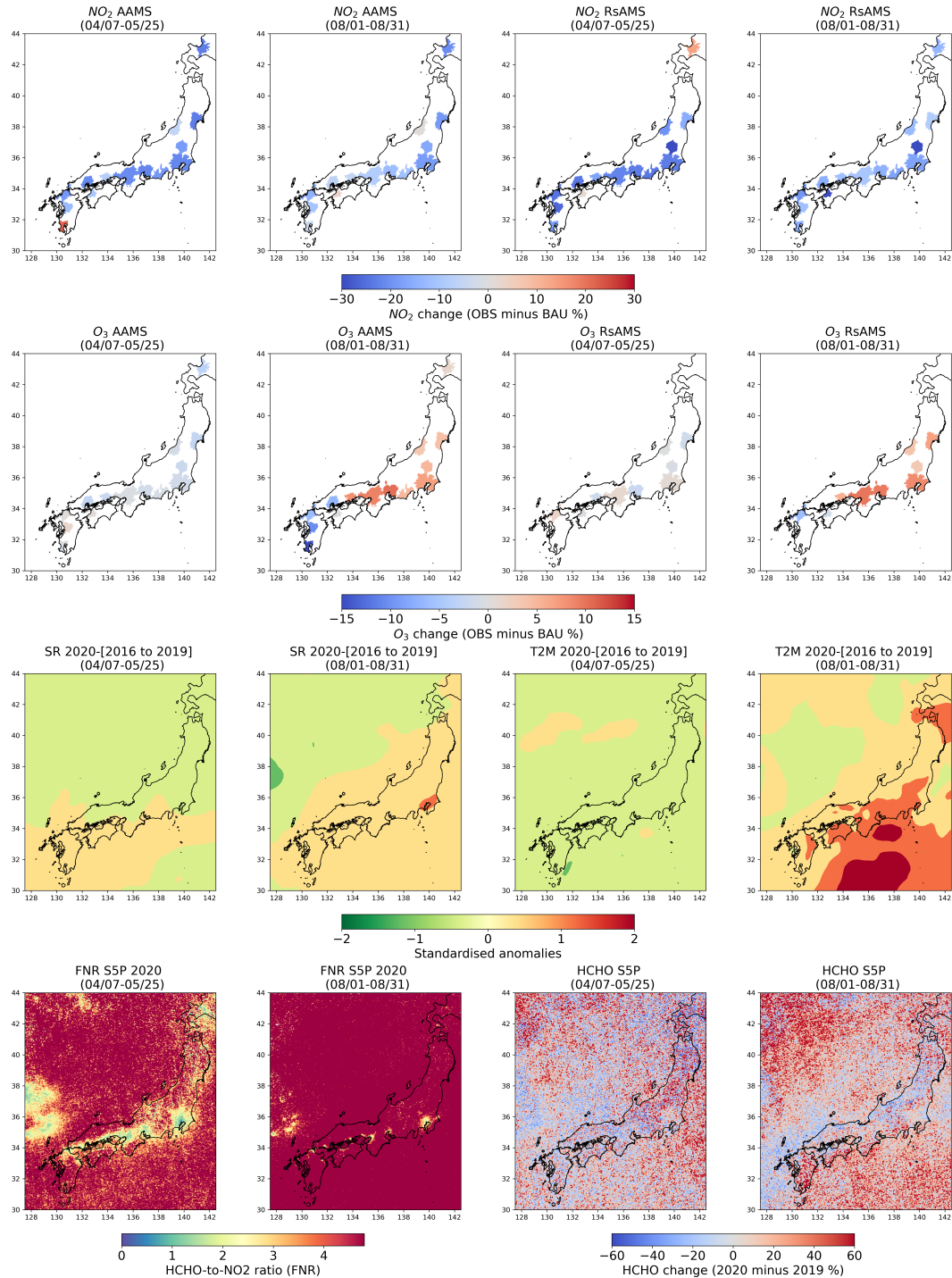


**Figure 4.5.** The 1st and 3rd columns show the plots for the lockdown (April 7 to May 25). The 2nd and last columns show the plots for August 1 – 31. The 1st row: The OBS-BAU estimates of  $\text{NO}_2$  for AAMS and RsAMS. The 2nd row: The OBS-BAU estimates of  $\text{O}_3$  for AAMS and RsAMS. The 3rd row: The standardised anomalies of downward solar radiation (SR) and temperature (T2M) from ERA5 dataset. The last row: The formamide-to- $\text{NO}_2$  (FNR) ratio in 2020 and the HCHO change between 2020 and 2019 from Sentinel 5P data.

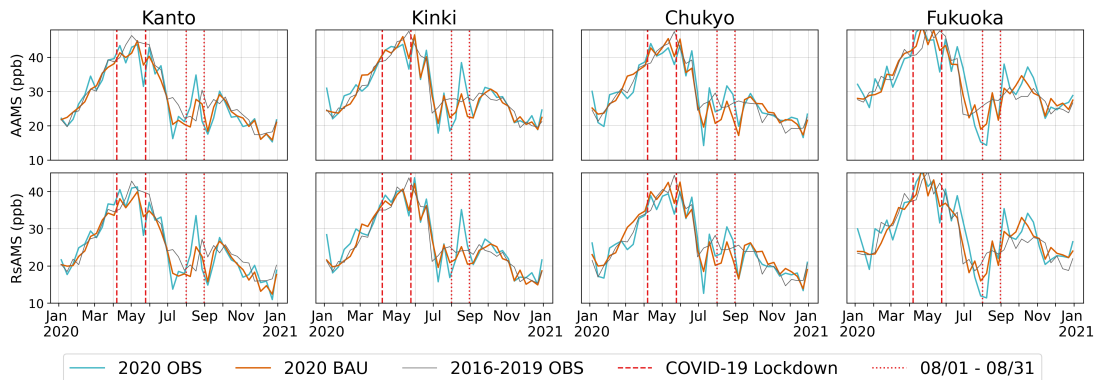


**Figure 4.6.** The 7-day rolling mean of 2020 observation (OBS), BAU prediction (BAU), and mean level of O<sub>3</sub> from 2016 to 2019 for 4 MAs (Kanto, Kinki, Chukyo, and Fukuoka)

was 5.1% for AAMS and 9.8% for RsAMS. This observation could be attributed to the greater reduction in movement during weekends compared to weekdays in these MAs as shown in Figure 1b.

In order to investigate the differences in O<sub>3</sub> levels between August and the lockdown period, we examined the standard anomalies of SR and T2M in August 2020, comparing them to the 2016-2019 period. Our analysis revealed positive anomalies in both SR and T2M across all MAs, as shown in Figure 5 (3rd row). These favorable weather conditions, combined with the reduced levels of NO<sub>2</sub>, likely facilitated increased O<sub>3</sub> production.

Although there was an overall trend of increasing O<sub>3</sub> levels during this period, we did observe a reduction in O<sub>3</sub> levels in five MAs which is located in the southern region: Hiroshima (AAMS: 13.7%), Matsuyama (AAMS: 1%, RsAMS: 3%), Fukuoka (AAMS: 12.5%, RsAMS: 12.3%), Kumamoto (AAMS: 20.7%), and Kagoshima (AAMS: 29.9%). To understand the decrease in O<sub>3</sub> levels observed in these five MAs, we utilized the S5P FNR for 2020, as well as the changes in HCHO as a proxy for NMVOCs between 2020 and 2019. The FNR is commonly used to assess the sensitivity of near-surface O<sub>3</sub> levels (Martin et al., 2004). As suggested by (Duncan et al., 2010), when the FNR is below 1, the O<sub>3</sub> production regime is considered VOC-limited, and when it exceeds 2, it is considered NO<sub>x</sub>-limited. When the FNR values fall within the range of 1–2, O<sub>3</sub> is expected to be

in the transition regime (Duncan et al., 2010). However, it has been observed that the FNR can vary by region (Jin et al., 2020; Irie et al., 2021; Souri et al., 2023; Ren et al., 2022), and the assumption that it lies within the 1–2 range may not hold true at the global level (Schroeder et al., 2017). Hence, it might be essential to calculate this ratio on a regional scale (Damiani et al., 2022; Schroeder et al., 2017). Despite the FNR showing high variability in the region, it still provides information about the trend of O<sub>3</sub> production regimes in our study.

Figure 5 (last row) presents the FNR across all MAs indicating a shift in the O<sub>3</sub> production regime from VOC-limited during the initial lockdown to NO<sub>x</sub>-limited in August. This transition is evident as the FNR changes from  $0 < \text{FNR} < 2$  during the lockdown to  $\text{FNR} > 4$  in August. During the VOC-limited regime, a decrease in NO<sub>x</sub> typically leads to an increase in O<sub>3</sub> levels (Duncan et al., 2010). However, in the NO<sub>x</sub>-limited regime, a reduction in NO<sub>x</sub> can also result in a decrease in O<sub>3</sub> levels (Duncan et al., 2010). In Figure 5 (last row), we can observe that the NO<sub>x</sub>-limited regime dominates the five MAs of Hiroshima, Matsuyama, Fukuoka, Kumamoto, and Kagoshima. Despite NO<sub>2</sub> levels continuing to decline during this period, the HCHO levels exhibited a more significant increase in these MAs compared to the lockdown period. Hence, this could explain the reduction in O<sub>3</sub> levels observed in these five southern MAs.

We elucidated the difference in O<sub>3</sub> levels between major MAs in Japan and other large urban areas worldwide by examining meteorological changes (T2M, SR), and variations in O<sub>3</sub> precursors levels by utilizing S5P FNR derived from S5P NO<sub>2</sub> and HCHO measurements. The difference can be attributed to the absence of sunny conditions during the lockdown period. However, in August, when sunny conditions became more prevalent, we observed an increase in O<sub>3</sub> levels in response to the sustained reduction in NO<sub>2</sub> levels across most MAs, which are likely VOC-limited areas. Based on the analysis of S5P data, it appears that the southern metropolitan areas (MAs) exhibited a predominant NO<sub>x</sub>-limited trend during August 2020, potentially due to the increased presence of biogenic VOCs (BVOCs). However, the monitoring of BVOCs emissions remains challenging due to limited observations (Tani and MOCHIZUKI, 2021; Ito and Ichii, 2021). Therefore, it is also important to pay attention to those NO<sub>x</sub>-limited areas, as future reductions in anthropogenic NMVOCs may have minimal effectiveness in

reducing O<sub>3</sub> levels (Akimoto and Tanimoto 2022).

#### 4.4.3 CH<sub>4</sub> level changes

In this experiment, we analyze the "OBS-BAU" estimates for NO<sub>2</sub>, CO, and CH<sub>4</sub>, and incorporate the VISIT model's simulated CH<sub>4</sub> emissions from wetlands to investigate the changes in CH<sub>4</sub> levels during the 2020 lockdown and post-lockdown period. Our focus is on understanding the relationship between the reduction in NO<sub>2</sub> and its potential impact on OH (hydroxyl radicals), as well as the contrasting effect of CO. The decrease in NO<sub>2</sub> levels is expected to result in a reduction in OH, while reductions in CO can increase OH levels and shorten the lifetime of CH<sub>4</sub> (Akimoto and Tanimoto, 2022).

During the lockdown period, we observed a marginal rise in CH<sub>4</sub> levels across most MAs (Figure 7 third row and Figure 8b), with an average increase of 0.6% for AAMS and 0.8% for RsAMS (Table 3). While NO<sub>2</sub> levels decreased in most MAs (Figure 7 first row), the trend for CO varied (Figure 7 second row and Figure 8a). AAMS showed an average decrease of 10.9% in CO levels, while RsAMS saw a slightly smaller reduction 8.8%. Notably, CO levels significantly increased in RsAMS of Kagoshima (60.6%), while slight increases were observed in Kanto AAMS, and in Matsuyama for both RsAMS and AAMS. It is worth noting that although the increases in CO levels in Kagoshima were significant, this region have among the lowest natural CH<sub>4</sub> emissions in Japan as Figure 7 (last row), which explains the slight increase in CH<sub>4</sub> observed in this MA.

During the post-lockdown period from June to December 2020, NO<sub>2</sub> levels continued to decrease, showing an average reduction of 12.8% for AAMS and 18.3% for RsAMS (Table 3) which is smaller than during the lockdown period. In contrast, CO levels started to recover as the COVID-19 lockdown was lifted, with a smaller reduction of 5.7% for AAMS and 5.5% for RsAMS. Notably, significant increases in CO levels were still evident at RsAMS in Kagoshima (62.2%). In Fukuoka we also observed a steady rise of CO levels in both RsAMS (13%) and AAMS (11.5%). In response to these changes in NO<sub>2</sub> and CO, we observed a greater increase in CH<sub>4</sub> levels during this period, with a rise of 1.3% for AAMS and 1.1% for RsAMS.

In general, we saw a slight increase in CH<sub>4</sub> levels both during the lockdown

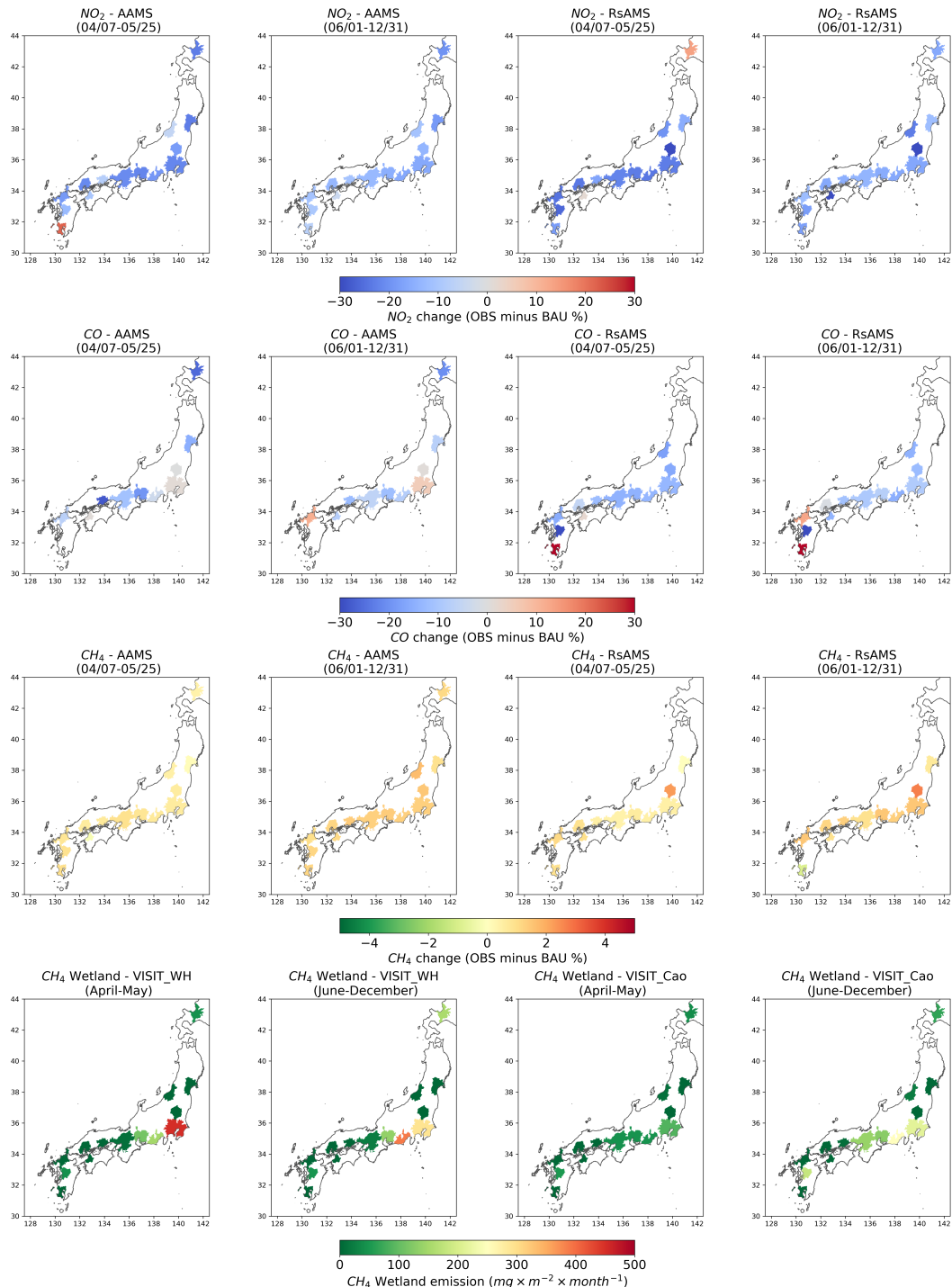


**Figure 4.7.** The 1st and 3rd columns show the plots for the lockdown (April to May). The 2nd and last columns show the plots for the post-lockdown (June to December). The 1st row: The “OBS-BAU” estimates of NO<sub>2</sub> for AAMS and RsAMS. The 2nd row: The “OBS-BAU” estimates of CO for AAMS and RsAMS. The 3rd row: The “OBS-BAU” estimate of CH<sub>4</sub> for AAMS and RsAMS. The last row: The CH<sub>4</sub> emission from wetland based on the simulation of VISIT model with Walter and Heimann scheme and Cao scheme.

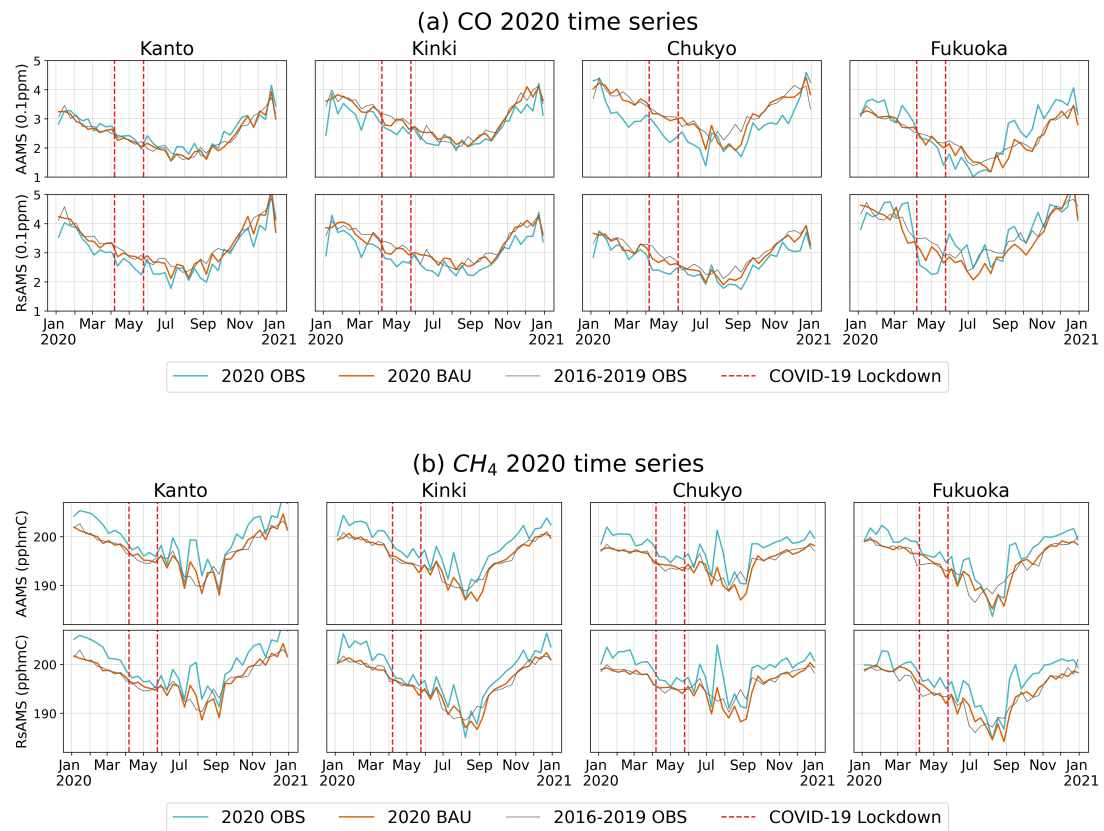


**Figure 4.8.** The 7-day rolling mean of 2020 observation (OBS), BAU prediction (BAU), and mean level of CO (a) and CH<sub>4</sub> (b) from 2016 to 2019 for 4 MAs (Kanto, Kinki, Chukyo, and Fukuoka)

and the post-lockdown periods, based on the "OBS-BAU" estimates. However, a more pronounced increase in CH<sub>4</sub> was observed during the post-lockdown phase in AAMS when compared to RsAMS, which can be attributed to the more substantial recovery of CO levels in AAMS relative to the lockdown period. Although it has been reported that global CH<sub>4</sub> growth in 2020 is primarily attributed to the atmospheric sink resulting from lower anthropogenic NO<sub>x</sub> emissions (Stevenson et al., 2022; Peng et al., 2022), our findings regarding the contribution of NO<sub>x</sub> reduction to the CH<sub>4</sub> growth in Japan in 2020 align with a previous study (Akimoto and Tanimoto, 2022; Qu et al., 2022; Feng et al., 2023), indicating that the impact of NO<sub>x</sub> and CO change on the increase in CH<sub>4</sub> growth in Japan during

**Table 4.4.** OBS-BAU estimates for NO<sub>2</sub> and CO and CH<sub>4</sub> during the lockdown (April 7 to May 25) and the post-lockdown (June 1 to December 31). For CH<sub>4</sub> analysis we only consider timeseries estimate which include all days of the week. The values are represented as mean (standard deviation)

Pollutant	Station type	(April 7 – May 25)	(June 1 – December 31)
		(%)	(%)
NO <sub>2</sub>	AAMS	-14.5 (12.1)	-12.8 (4.3)
	RsAMS	-19.1 (13.5)	-18.3 (6.4)
CO	AAMS	-10.9 (11.0)	-5.7 (9.4)
	RsAMS	-8.8 (24.6)	-5.5 (25.2)
CH <sub>4</sub>	AAMS	0.6 (0.3)	1.3 (0.2)
	RsAMS	0.8 (0.6)	1.1 (0.9)

the lockdown and post-lockdown period is not as significant as the direct CH<sub>4</sub> emission itself.

## 4.5 Discussion

### 4.5.1 Variations in spatial resolution of multisource data

Since we utilized multisource data for the analysis, we acknowledge that variations in spatial resolution among input data can influence the consistency and reliability of data analysis. In certain situations, the need for interpolation to achieve a uniform grid may arise, particularly when generating inputs for a Convolutional Neural Network (CNN). This interpolation process inadvertently introduces uncertainty into the results. However, in this study, we refrained from any data interpolation and used it at its provided original resolution. The multisource data was employed for two primary objectives: weather-normalization model development and visual examination purpose.

For weather-normalization model development, we used ERA5 data and ground station data to construct the weather-normalization model. Certain variables, such as total cloud cover and boundary layer height, are exclusively available from ERA5. The ERA5 data we employed has a resolution of  $0.25^\circ \times 0.25^\circ$ , meaning

that some stations might share identical ERA5 records. This can influence the model development, even though, ideally, local ERA5 values for each station should be distinct, albeit not significantly deviating from the  $0.25^\circ \times 0.25^\circ$  spatial resolution value. To mitigate this effect on the model development, we have integrated spatial context values (latitude and longitude) and station types as additional inputs. Since these features are distinct for each station, we anticipate that they can help minimize the impact of the coarse spatial resolution from ERA5 on the model.

To visually inspect the sensitivity of tropospheric O<sub>3</sub> production utilizing S5P HCHO and NO<sub>2</sub>, as well as CH<sub>4</sub> emission estimates from wetland, we rely exclusively on original data with consistent spatial resolution. It's important to note that our primary focus is to visually inspect the prevailing trends at the MA level, which has a spatial resolution coarser than that of any input data we utilized. Therefore, we believe that the dominant trends at the MA level remain unaffected by these spatial disparities in this particular MA-level context.

#### 4.5.2 Limitations

In this research, we utilized the S5P FNR to examine the sensitivity of O<sub>3</sub> production. Although HCHO could be an alternative indicator for NMVOCs presence, the significant uncertainty in the FNR threshold from previous studies, along with the lack of NMVOCs observations and reliable satellite HCHO and NO<sub>2</sub> data, poses challenges in understanding O<sub>3</sub> level variations during and after the lock-down period. This issue is particularly crucial and warrants in-depth exploration in future studies.

Additionally, it's important to mention that the study did not include an analysis of long-range air pollution transportation from China to western MAs of Japan following the Chinese economic recovery from the pandemic (Itahashi et al., 2022). This aspect was beyond the scope of the current research but should be considered in future investigations.

## 4.6 Conclusion

This study presents an air quality analysis that examines the changes in four air pollutants, namely NO<sub>2</sub>, O<sub>3</sub>, CO, and CH<sub>4</sub>, during the COVID-19 pandemic in 14 MAs of Japan from April 7 to December 31 in 2020. Firstly, we developed a machine learning BAU model that incorporates meteorological, spatial, and temporal features to account for weather variability in air quality time series. Next, we utilized the BAU model predictions and observation data to estimate the actual reduction (OBS-BAU estimate) in NO<sub>2</sub> levels. We then integrated temperature and solar radiation anomalies from ERA5 reanalysis data and S5P TROPOMI data (FNR and HCHO) along with the “OBS-BAU” estimate to investigate the unique response of O<sub>3</sub> to the NO<sub>2</sub> reduction during the lockdown and post-lockdown period (August 1 – 31, 2020). Finally, we evaluated the impact of NO<sub>2</sub> and CO changes on the CH<sub>4</sub> levels using a combination of “OBS-BAU” estimate and wetland CH<sub>4</sub> emission simulations from the VISIT model. The main findings of the study can be summarized as follows:

Based on ground observations of NO<sub>2</sub>, the reduction of NO<sub>2</sub> during the lockdown period in 2020 corresponds to a decrease equivalent to 3.4 years and 5 years of the 2010-2019 trend of NO<sub>2</sub> for roadside and ambient air monitoring stations respectively. After normalizing the meteorological effects by BAU predictions, the NO<sub>2</sub> reduction was 14.5% for AAMS and 19.1% for RsAMS. The decrease in NO<sub>2</sub> levels is more pronounced during the weekend than on weekdays.

By analyzing ground observations of NO<sub>2</sub> and O<sub>3</sub>, along with BAU simulations and meteorological data from ERA5, as well as FNR and HCHO data from S5P TROPOMI, we found that the reduction in NO<sub>2</sub> levels during the lockdown did not immediately result in an increase in O<sub>3</sub>. Instead, we observed that the increase in O<sub>3</sub> occurred after the lockdown, specifically in August when sunny conditions were reinforced. This finding is significant for Japan, as it has not been previously reported in other studies.

Furthermore, when analyzing the ground observations of NO<sub>2</sub>, CO, and CH<sub>4</sub> alongside BAU simulations and model-simulated CH<sub>4</sub> emissions from wetlands, we found that the changes in NO<sub>2</sub> and CO contributed marginally to the variations in CH<sub>4</sub> levels, ranging from 0.6% to 1.3%, across the study areas. This finding aligns with previous studies (Akimoto and Tanimoto, 2022; Qu et al.,

2022; Feng et al., 2023), but also differs from others where the reduction in atmospheric sink has been reported as a major contributor to increased CH<sub>4</sub> levels (Stevenson et al., 2022; Peng et al., 2022).

Based on the findings of this study, we recommend simultaneous reduction of air pollutants and anthropogenic VOCs as well as biogenic VOCs to mitigate the adverse effects on O<sub>3</sub> and CH<sub>4</sub>. These pollutants are significant SLCPs that can have detrimental impacts on future climate mitigation efforts. Therefore, it is crucial to address both air pollutants and VOCs emissions to effectively mitigate these adverse effects in the future policies.

# **GREENHOUSE GAS ESTIMATION, FORECASTING AND MONITORING**

# 5 Plant functional types mapping

We proposed a combined machine learning approach with a deep convolutional neural network (CNN) to monitor forest utilization toward Sustainable Development Goals (SDGs) for data-scarce regions. First, we employed the Random Forest (RF) classifier using Google Earth Engine (GEE) for forest mapping. Then, we designed a deep CNN architecture that works for PFTs/age mapping from coarse and polygonal ground-truth data. The proposed network has U-shape and comprises 3D Atrous Convolutions. The model was optimized by a weighted cross-entropy loss function. We trained the model with times-series Sentinel 1, 2, and Digital Elevation Model (DEM) data with sparse annotations. Our proposed models achieved 94.5% overall accuracy (OA) for forest mapping, 77.80% (OA) for PFTs, and 81.74% (OA) for forest age classification, respectively in Ena city, Japan. The outcome of our study indicates the potential of remote sensing and machine learning in monitoring forest development, conservation, and utilization toward SDGs from coarse ground-truth data. Our source code for the implementation is available at: [https://github.com/anhp95/forest\\_attr\\_segment](https://github.com/anhp95/forest_attr_segment)

## 5.1 Introduction

The pivotal role of forests in advancing Sustainable Development Goal 15 (SDG15) and addressing global climate change is widely recognized. Leveraging the capabilities of remote sensing technology and cutting-edge machine learning algorithms, the mapping of forested areas, along with the identification of PFTs and forest age, emerges as a valuable contribution to the monitoring of SDG-related issues, encompassing indicators such as 15.1.1, 15.2.1, and 15.4.2.

While forest mapping is a familiar task in land-cover/land-use classification, generating a detailed map specifying plant functional types (PFTs) and forest

age introduces heightened complexity. Previous studies focusing on PFTs/age classification often relied on either high-resolution input data or ground-truth information at the point level, as evidenced in the works of (Schiefer et al., 2020; La Rosa et al., 2021; Lee et al., 2016). However, these resources are known to be expensive, time-consuming to collect, and infrequently available in specific regions, particularly in developing areas. In response to these challenges, this chapter introduces a methodology aimed at monitoring forest areas, PFTs, and forest age, utilizing coarse annotations and freely available remote sensing data.

The approach begins with the application of a Random Forest (RF) classifier to classify forested areas. Subsequently, a deep Convolutional Neural Network (CNN) architecture is designed for the segmentation of PFTs and forest age. Notably, our proposed methodology demonstrates its efficacy in regions where data scarcity is a significant concern.

The structure of this chapter unfolds as follows: Section 5.2 provides insights into the study area and the data utilized in the study. Section 5.3 delves into the overall methodology employed, and the experimental results within the study area are expounded upon in Section 5.4. Finally, Section 5.5 encapsulates the conclusion of the chapter, highlighting avenues for future research and development.

## 5.2 Data

### 5.2.1 Study area

The focal point of our investigation is Ena city (see Figure 5.1), strategically positioned in the southeastern expanse of Gifu prefecture, nestled within the heart of Japan. Encompassing an expansive total area of approximately 504 square kilometers, the city boasts an elevation of 282 meters, contributing to its diverse topography. The climate exhibits a noteworthy annual temperature range, spanning from a minimum of 2 °C to a maximum of around 26.4 °C, showcasing the dynamic climatic conditions that characterize the region.

A compelling facet of Ena city lies in its rich forest cover, a significant portion of which, as reported by local government statistics, comprises artificial forests,

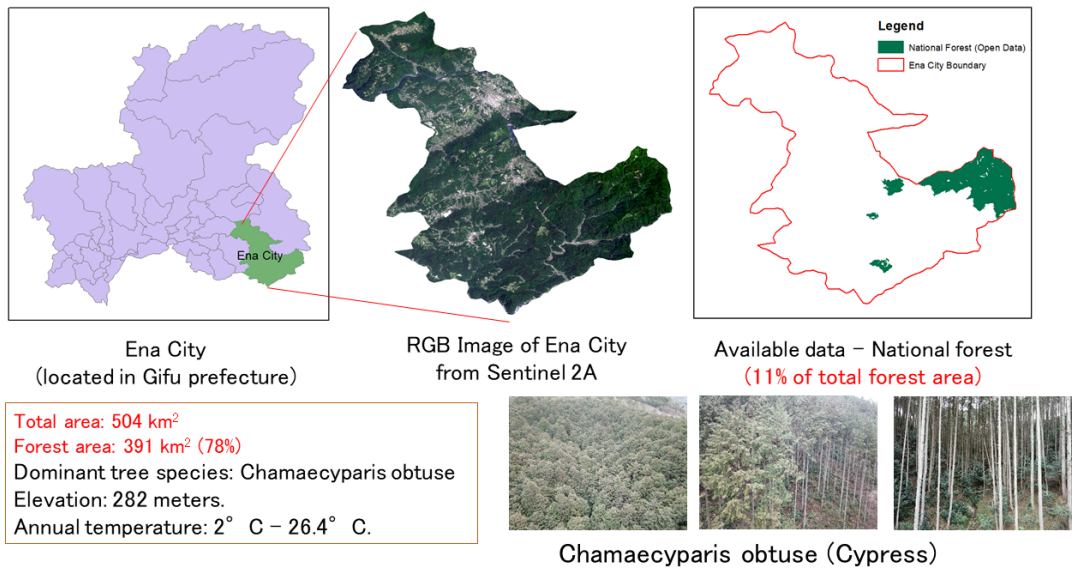


**Figure 5.1.** Ena city and national forest in Ena city.

constituting 60% of the total forested area. The dominant species within these artificial forests is *Chamaecyparis obtusa*. This coniferous species plays a pivotal role in the city's ecosystem, serving multifaceted purposes such as timber production, prevention of water-related disasters, and the sequestration of carbon dioxide (CO<sub>2</sub>). Notably, the artificial forest, largely populated by *Chamaecyparis obtusa*, underscores its significance as a valuable resource for sustainable timber harvesting, acting as a buffer against potential water-related calamities, and contributing to the mitigation of greenhouse gas emissions through effective CO<sub>2</sub> sequestration. This intricate interplay of environmental elements highlights the intricate web of ecological services provided by Ena city's forests, emphasizing their integral role in the broader context of regional sustainability and resilience.

### 5.2.2 Data collection

In our forest mapping approach, the creation of a training set involved a random selection of 750 forest and 250 non-forest points, alongside a validation set comprising 300 forest and 100 non-forest points. This selection was based on the 2016 land-use map provided by the National Land Information Portal. Transitioning

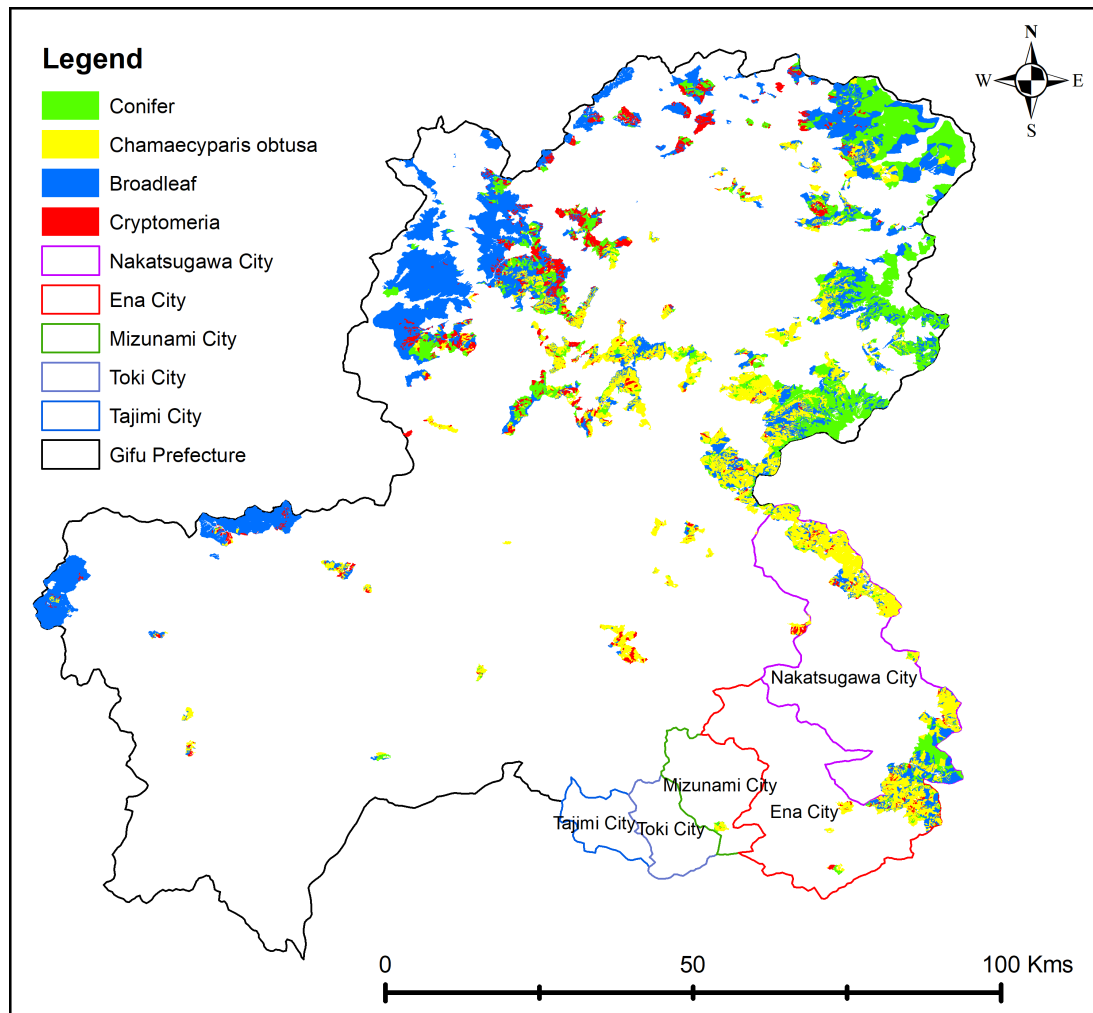
to the task of mapping PFTs and forest age, our labeled data was sourced from the same repository. The ground-truth information, represented as coarse polygons, delineates mixed-species zones, with each polygon annotated according to the most dominant PFTs in that particular area. Notably, this ground-truth data is restricted to national forest areas, presenting a limitation in its coverage. To address this constraint, given the relatively small portion (11%) of national forest data available for Ena city, we supplemented our dataset with the annotations collected in 2018 from Gifu prefecture to enhance model training (5.2).

Our utilization of remote sensing resources encompassed Sentinel 1A, Sentinel 2 L1C, and a Digital Elevation Model (DEM), each featuring spatial resolutions of 10m, 10m, and 30m, respectively. The dataset comprises 11 spectral channels, encompassing the Red, Green, Blue, Red Edge, Near-infrared, Short-wave infrared, and Normalized Difference Vegetation Index (NDVI) from Sentinel 2, along with the VV and VH bands from Sentinel 1A. Additionally, the DEM data is derived from the NASA Shuttle Radar Topography Mission digital elevation model, providing crucial elevation information. This comprehensive dataset serves as the input features for our machine learning model.

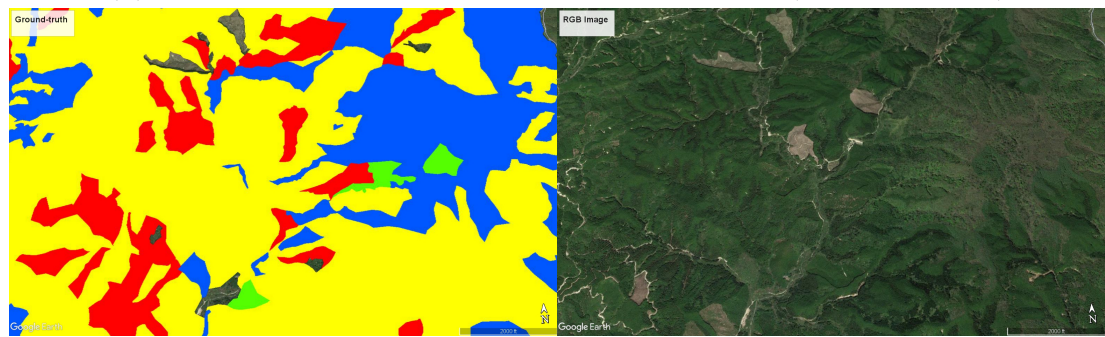
In the subsequent sections, we describe the specifics of acquisition times for Sentinel 1 and Sentinel 2, pertaining to the segmentation of PFTs and forest age, as well as forest mapping. Recognizing the dynamic nature of forest ecosystems and evolving land-use patterns, the temporal dimension of data acquisition plays a crucial role in maintaining the relevance and accuracy of our models.

### 5.3 Methodology

The proposed workflow is depicted in Figure 5.3a. Initially, the Sentinel 1 data was obtained directly from Google Earth Engine (GEE). Each pixel represents the backscatter coefficient and undergoes a series of preprocessing steps, including the application of an orbit file, removal of GRD border noise, thermal noise elimination, radiometric calibration, and terrain correction. The Sentinel 2 data was mosaicked and monthly averaged to address clouds and missing values, also leveraging GEE. The training and validation sets for forest mapping, Plant Functional Types (PFTs), and forest age segmentation were extracted from the satellite im-



(a) Annotations of national forest in Gifu prefecture (black boundary)



(b) Example of annotated area

(c) The corresponding RGB image

**Figure 5.2.** (a) The designated study area outlined in red is Ena city, (b) demonstrates coarse annotations as an illustrative example, and (c) showcases the corresponding RGB image sourced from Google Earth.

ages. Subsequent sections provide a detailed illustration of how these acquired sets are utilized to train the machine learning models.

### Forest mapping

To expedite the forest mapping process, we implemented the Random Forest (RF) model, a widely recognized ensemble machine learning classifier for land-cover and land-use classification (Gislason et al., 2006). The utilization of RF is well-founded not only due to its popularity but also its demonstrated effectiveness in land-cover mapping, particularly when dealing with low-resolution ground-truth data (Robinson et al., 2021). This machine learning approach leverages the strength of ensemble techniques, combining multiple decision trees to enhance accuracy and robustness in the classification of forested areas. The choice of RF aligns with its established success in handling land-cover mapping challenges, making it an efficient solution for our specific context.

### PFTs/forest age mapping

While Random Forest (RF) exhibits commendable performance with low-resolution labeled data, it falls short of achieving superior results compared to our proposed deep learning model, as indicated in Table 5.2. The architecture of our proposed network draws inspiration from the UNET architecture (Ronneberger et al., 2015) but is intentionally shallower, as depicted in Figure 5.3b. To enhance the model’s semantic segmentation capabilities, we incorporated 3D Atrous Convolution (3DACConv), a technique proven effective in handling semantic segmentation tasks with coarse annotations (Chen et al., 2017b). Atrous convolution, initially introduced in the DeepLab architecture (Chen et al., 2017a), involves convolution with upsampled filters.

The model comprises an encoder and decoder path backbone. The encoder path encompasses three layers, with the first layer featuring three 3D convolutions (3DConv) followed by a 3DACConv. The second layer contains three 3DConvs, while the last layer consists of one 3DConv followed by a 3DACConv. A  $2 \times 2 \times 2$  max pooling layer with strides of two follows each encoder layer. Each 3DConv is followed by a rectified linear unit (ReLU), before each ReLU is a batch normalization (BN). Notably, we avoid doubling the number of channels immediately

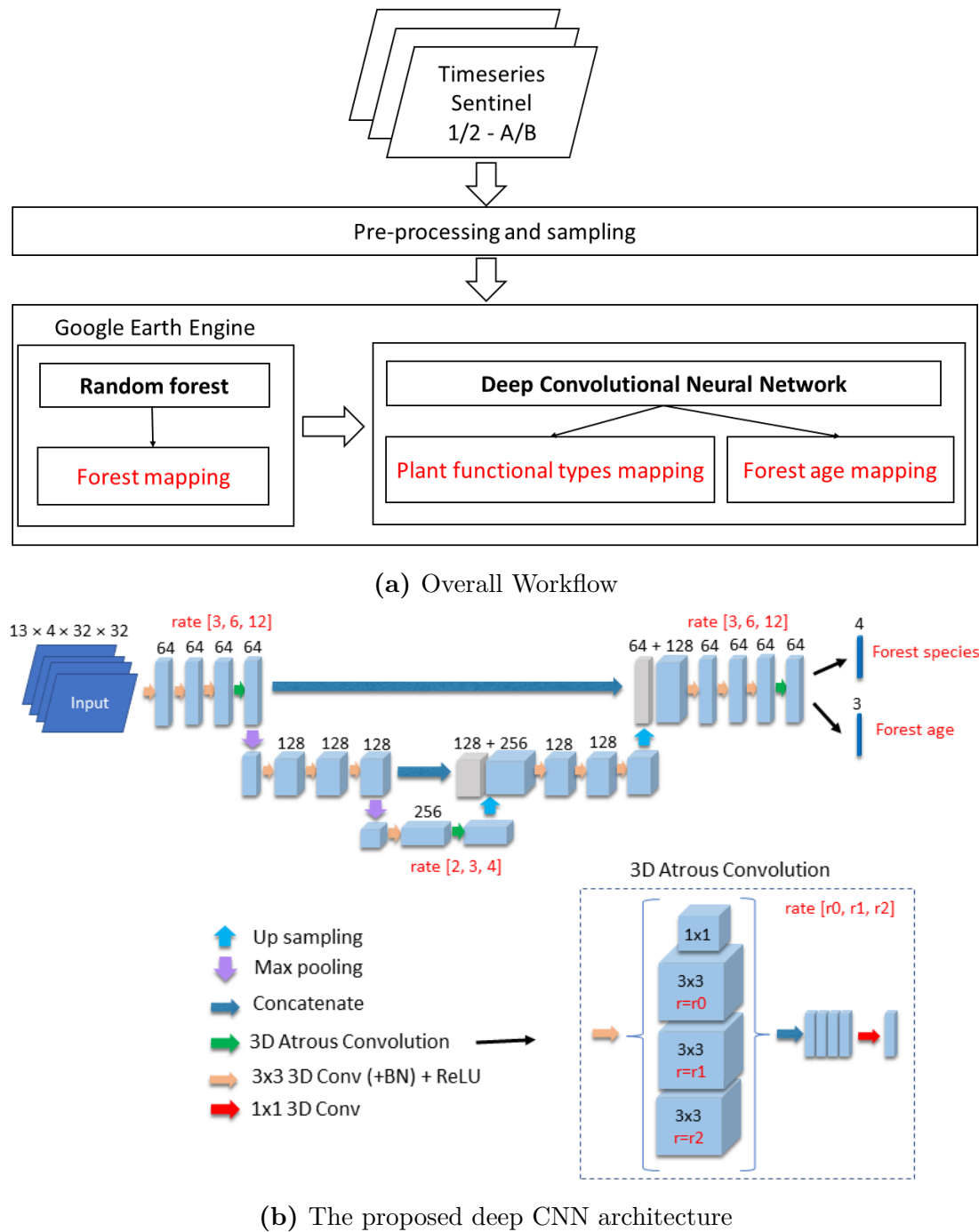


**Figure 5.3.** (a) Overall workflow and (b) The proposed deep CNN architecture.

before the max pooling, a departure from the approach introduced in 3D UNET (Çiçek et al., 2016).

Moving to the decoder path, ConvTranspose3D is employed for up-convolution to upsample the feature map. A 3DACConv is added at the end of the decoder path. The output dimensions are then reduced to the number of labels through a  $1 \times 1 \times 1$  3DConv following the last 3DACConv. In our specific case, the number of labels is 4 for Plant Functional Types : Broadleaf, Conifer, Cryptomeria, Chamaecyparis obtusa; and 3 for forest age: young forest ( $\leq 20$  years), mature forest (21-50 years), and harvesting age ( $\geq 50$  years).

**Table 5.1.** Training and validation samples and the corresponding weights for cross-entropy loss function.

Class	Training set	Validation set	Weight
PFTs (number of input images)			
Broadleaf	5017	264	0.153
Conifer	3048	160	0.252
Chamaecyparis obtusa	3191	168	0.241
Cryptomeria	768	40	1
Forest age (number of input images)			
Harvesting age	4000	205	0.05
Mature age	2095	110	0.1
Young age	186	10	1

The input data is structured with dimensions  $13 \times 4 \times 32 \times 32$ , representing the number of channels, time-series periods, height, and width, respectively. Each input image consists of  $32 \times 32$  pixels, encompassing a total of 13 channels distributed across three time-series periods. The Digital Elevation Model (DEM) data was incorporated, contributing to the formation of the 4th dimension in the input. Further elaboration on these details is provided in the subsequent section for a more in-depth understanding.

Given the imbalanced nature of the training set, as evident in Table 5.1, we fine-tuned the model by incorporating a weighted cross-entropy loss function. Specifically, distinct weights were assigned for PFTs and age categories, as out-

lined in Table 5.1.

### Experiment design and settings

To assess the performance of the proposed network against Random Forest (RF), 2D UNET, and 3D UNET, we devised an experiment for Plant Functional Types (PFTs) and age mapping using time-series satellite data from Sentinel 1 and 2 in 2018. This data was organized into three distinct periods: January-April (P1), May-August (P2), and October-December (P3). For each period, we conducted a mosaicking and compositing process to create a comprehensive satellite image. Our initial exploration aimed to understand the impact of seasonal changes on PFTs and age mapping performance using RF and 2D UNET. Due to the constraints imposed by the input shape, the assessment of 3D UNET and our proposed model was carried out with data spanning the entire year. To facilitate training with our network and 3D UNET, the input shape needed to be adjusted to  $13 \times 4 \times 32 \times 32$ . This adjustment involved stacking the Digital Elevation Model (DEM) band with the Sentinel 1/2 data in P1, P2, and P3, resulting in input dimensions of each  $13 \times 32 \times 32$ .

The performance evaluation of segmentation models was conducted using the Overall Accuracy (OA) score on the validation set. Subsequently, results maps generated by each model underwent visual examination to provide a qualitative assessment.

Our deep learning model, implemented in PyTorch, underwent training on an NVIDIA GeForce RTX 3080 Ti GPU. The training process involved 100 epochs, utilizing the Adam optimizer (Kingma and Ba, 2014) with an initial learning rate of  $10^{-5}$ . The learning rate underwent halving after every 10 epochs.

In the context of forest mapping, our approach exclusively employed Sentinel 2 data from June 2018, complemented by 10-meter-resampled DEM data retrieved from GEE. This choice was guided by our observation that June data exhibits minimal slope effects, particularly in regions characterized by higher elevations. The utilization of GEE’s API facilitated a seamless implementation, significantly boosting computational efficiency throughout the mapping stages.

## 5.4 Experimental results

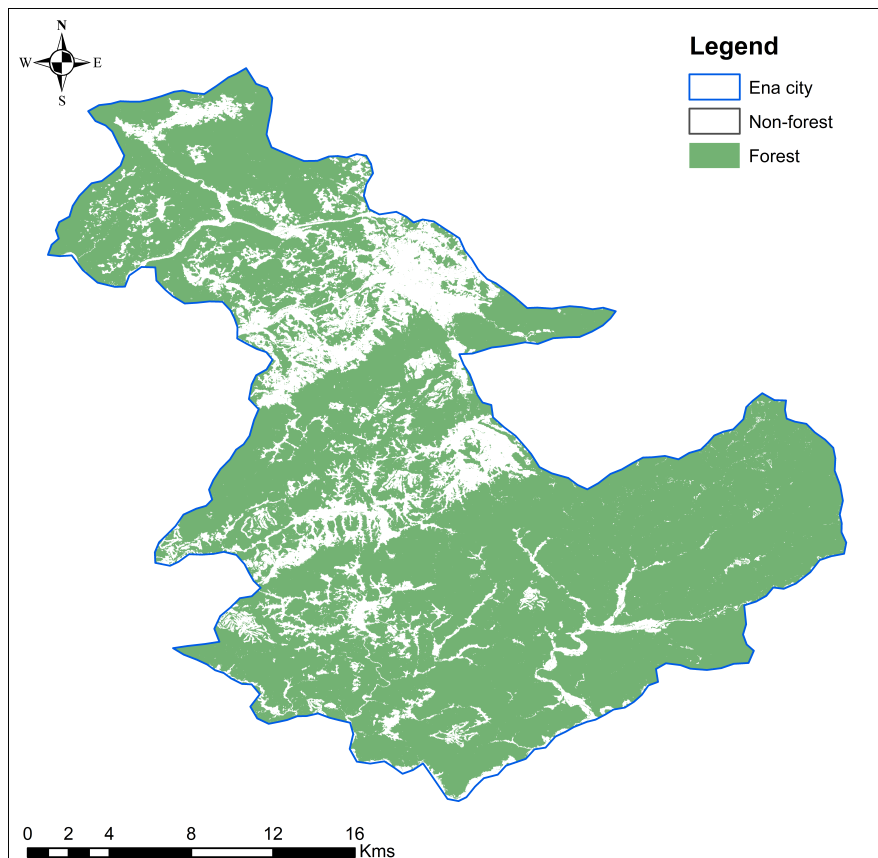
For forest mapping, the model accomplished a 94.5% Overall Accuracy (OA) for the classification of forest and non-forest areas. The resulting forest map, generated by the model, is displayed in Figure 5.4. Upon scrutinizing the high-resolution satellite image from Google Earth alongside the overlaid inferred forest map, it becomes evident that the RF model has proficiently and accurately classified the forest pixels using information derived from Sentinel 2 and DEM data.

**Table 5.2.** The experimental results of UNET and our model.

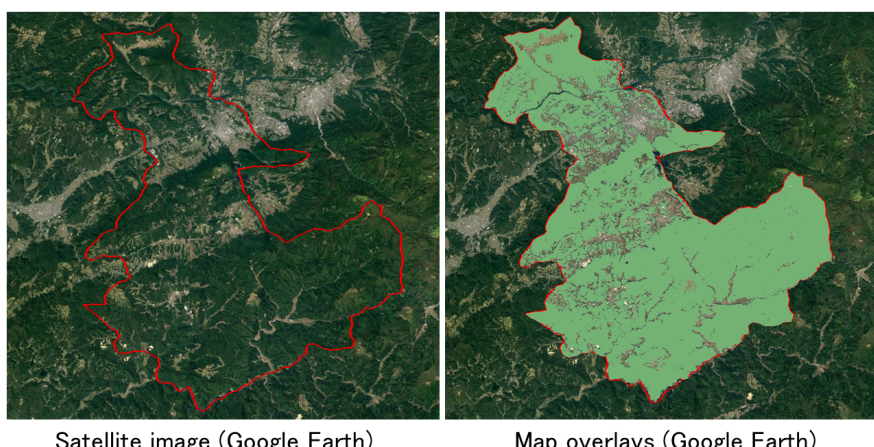
Model	Time-series period	Highest OA (%)	
		Species	Age
RF	P2	67.41	73.94
	P1 + P2	71.68	78.66
	P1 + P2 + P3	71.65	78.68
2D UNET	P2	59.81	65.67
	P1 + P2	67.25	75.4
	P1 + P2 + P3	65.02	74.55
3D UNET	P1 + P2 + P3	76.91	80.53
Our model	P1 + P2 + P3	77.80	81.74

As evident from Table 5.2, RF consistently outperformed 2D UNET across all conducted tests. Notably, both the RF and 2D UNET experiments yielded suboptimal results when exclusively relying on data from the P2 period, resulting in the lowest OA for both Plant Functional Types (PFTs) and forest age segmentation.

Substantial improvements in OA were observed when extending the time-series scheme from P2 to encompass P1 + P2. However, the addition of P3 to the training set did not yield a significant enhancement in the performance of RF and 2D UNET when compared to the P1 + P2 configuration. This suggests that, for the effective utilization of time-series data in PFTs and forest age segmentation within the study area, the preferable approach involves employing data collected from the January to August period. This is best achieved through an ensemble learning model like RF, or a CNN architecture based on 2D UNET.

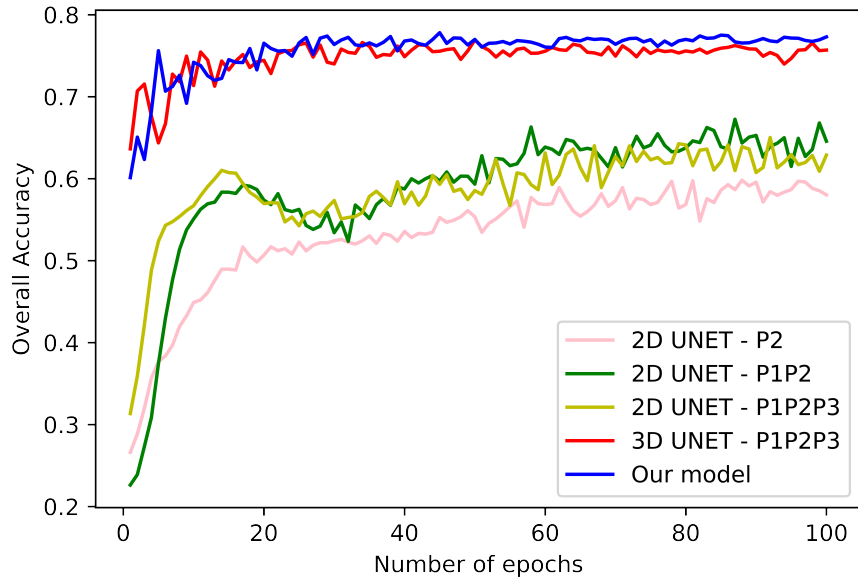


(a) Forest map in Ena City, Japan

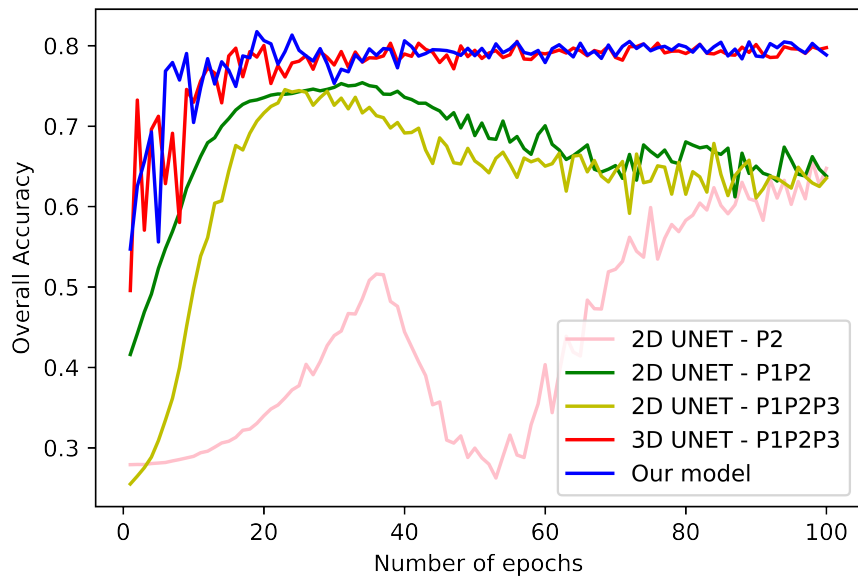


(b) Map overlays

**Figure 5.4.** Inferred forest map in Ena City, Japan –2018 (OA –94.5%)



(a) PFTs segmentation.



(b) Forest age segmentation.

**Figure 5.5.** OA profile of PFTs (a) and forest age (b) segmentation

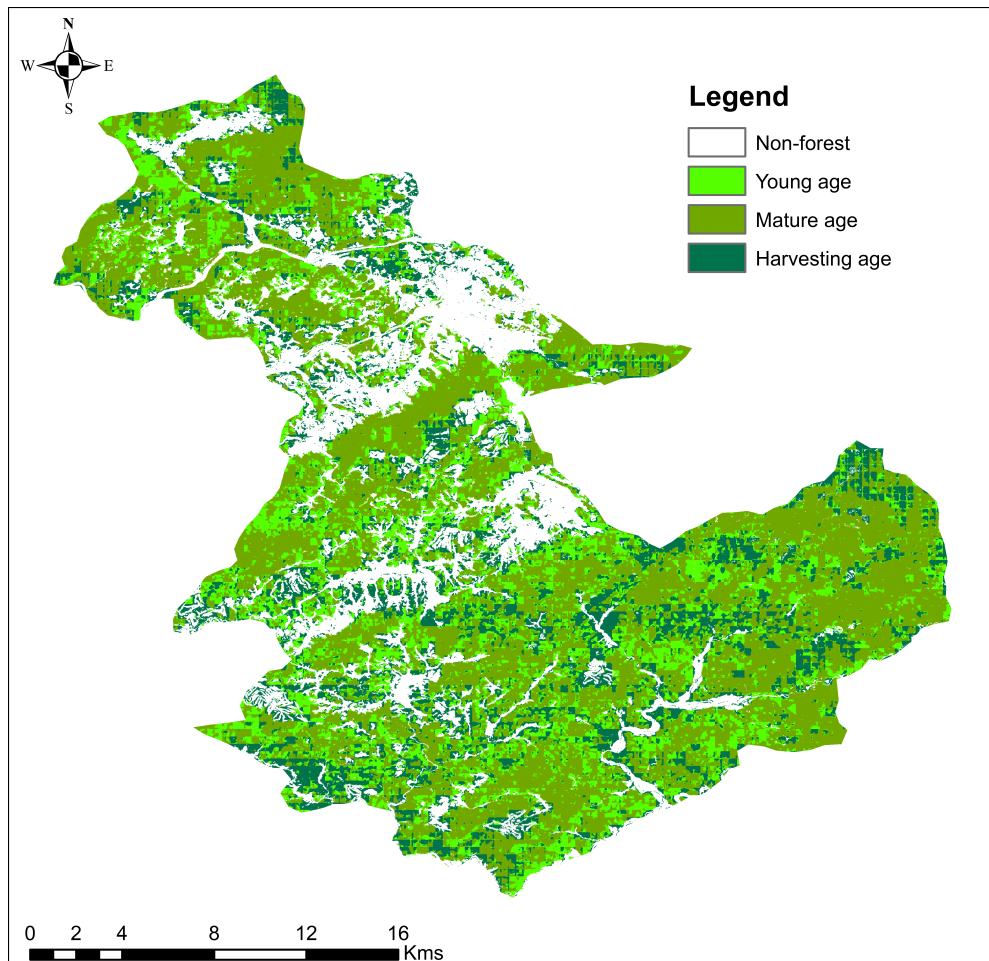


**Figure 5.6.** Inferred forest age map in Ena City, Japan –2018.

Despite the minimal impact of P3 data on the performance of RF and 2D UNET, with 3D CNN scheme in 3D UNET and our suggested model, the incorporation of P3 data has significantly elevated the OA in discriminating Plant Functional Types (PFTs) and forest age. The performance comparison of our model, 2D/3D UNET, and RF over 100 epochs is presented in Table 3.3, and Figure 5.5. Notably, the OA has experienced a substantial improvement, increasing from 71.68% to 76.91% with 3D UNET, and reaching 77.80% with our proposed model for PFTs segmentation. Similarly, for forest age segmentation, the OA has risen from 78.66% to 80.53% with 3D UNET, and to 81.74% with our model.

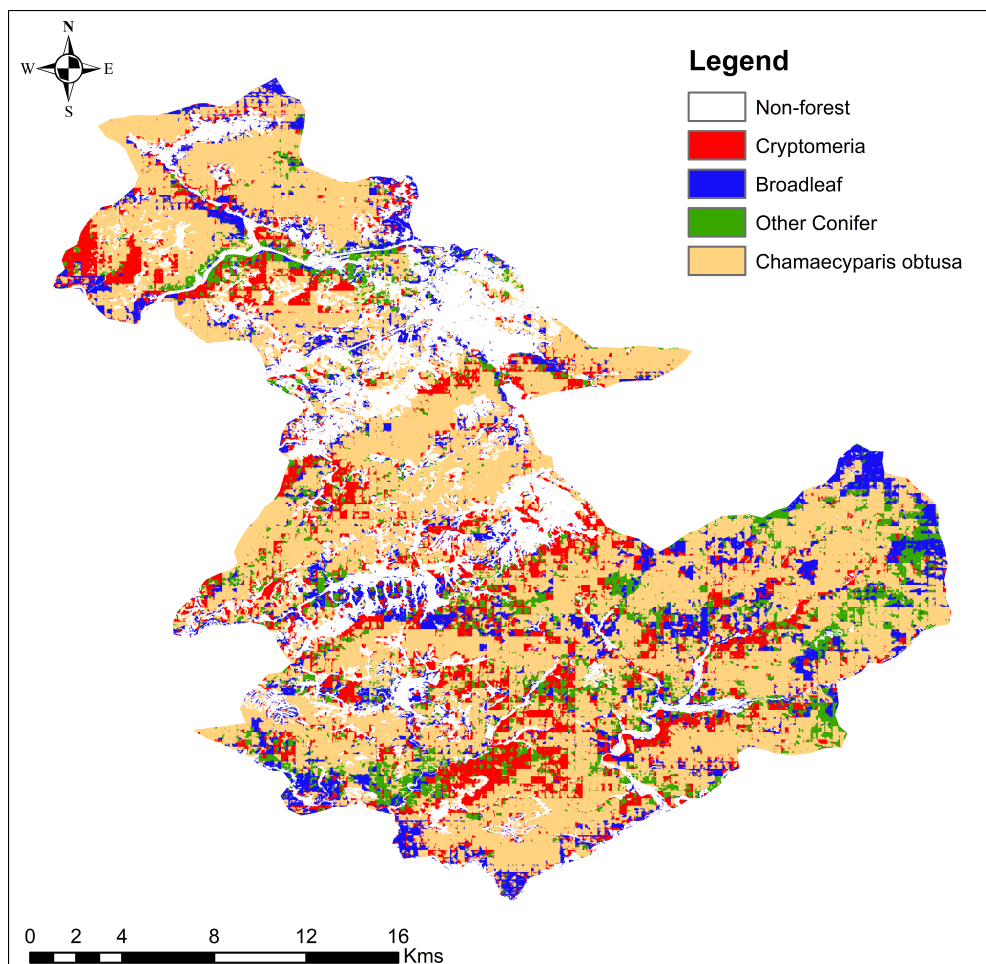


**Figure 5.7.** Inferred PFTs map in Ena City, Japan –2018.

The OA profiles in Table 3.3, and Figure 5.5 underscore the superior performance of our model compared to RF, 2D UNET, and 3D UNET, exhibiting an approximate 6.12%, 10.55%, and 0.89% higher OA for PFTs, and 3.03%, 6.31%, and 1.18% higher OA for forest age segmentation, respectively.

Figure 5.6 depicts the forest age map generated by our model, revealing that the primary harvesting-age areas are predominantly situated in the Northern, Southern, and central parts of the city. Mature-age forests are distributed extensively throughout the region, while smaller areas of young-age forests are scattered across the city from the west to the south.

The visual representation of the deduced PFTs map is presented in Figure

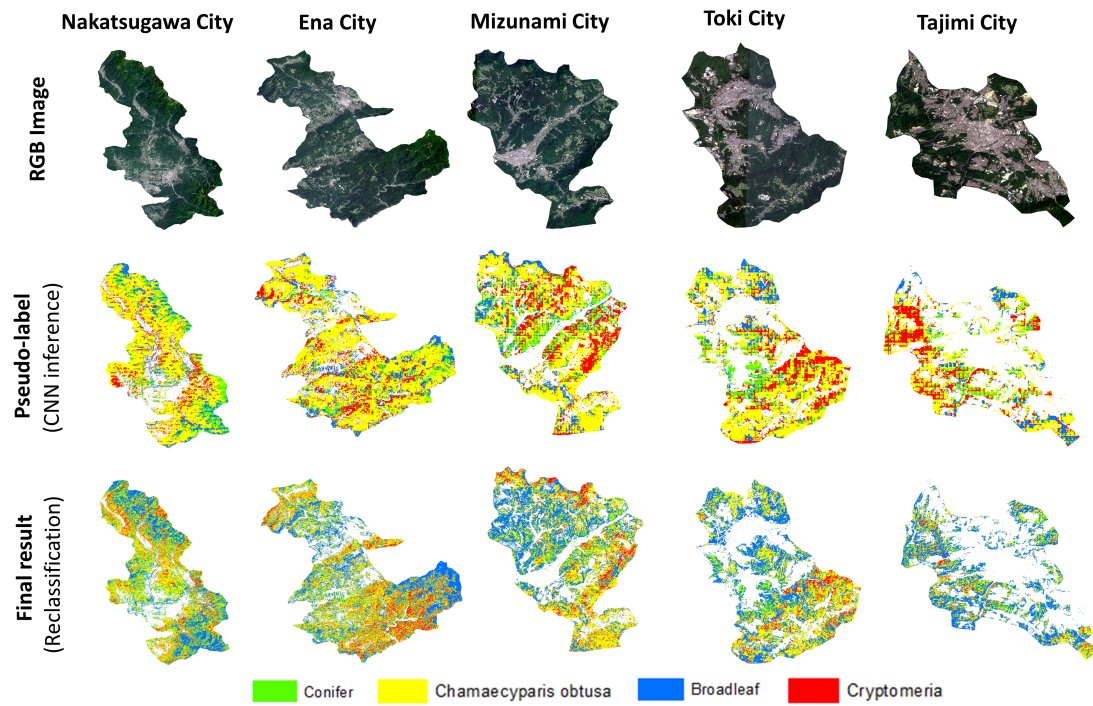


**Figure 5.8.** Performance of the proposed method in other regions.

5.7. Notably, *Chamaecyparis obtusa* emerges as the prevailing PFTs, exhibiting widespread distribution across the entire region. *Cryptomeria*, on the other hand, dominates the central Southeast and Northwest sectors of the study area. Broadleaf trees, in majority, are concentrated in the Northeast, Southern, and Northwest segments of the region. The identified Conifer species, while dispersed throughout the Northern and Southern regions, makes a minor contribution from the Northwest portion of the city.

Implementing the proposed methodology, we have expanded our mapping efforts to encompass additional cities in Gifu prefecture, namely Nakatsugawa, Mizunami, Toki, and Tajimi, as depicted in Figure 5.8. Our approach involved the initial application of the proposed network, followed by the utilization of a straightforward reclassification method. This process enabled the generation of a high-resolution map of Plant Functional Types (PFTs), derived from the pseudo-label output produced by the proposed model.

## 5.5 Conclusion

In this study, by utilizing remote sensing, RF classifier, and deep learning, the approach for forest-related SDG issues monitoring in data-scarce regions has been proposed. We examined the approach in Ena City, Japan and achieved promising results in forest mapping, and PFTs and forest age mapping. Our proposed model outperforms the RF, 2D/3D UNET in PFTs and forest age segmentation with coarse-polygonal ground-truth data. The outcome of this study could be served as an input for further steps to produce high-resolution land cover map for the data-scarce regions. In the future, we will investigate the postprocessing method to improve the map quality from coarse annotations.

# 6 Upscaling global carbon fluxes

## 6.1 Background and summary

Terrestrial ecosystem plays a crucial role in mitigating global warming, functioning as a persistent carbon sink (Pan et al., 2011). Terrestrial gross primary production (GPP) is the largest global carbon fluxes which contributes to the reduction of anthropogenic CO<sub>2</sub> in the atmosphere (Beer et al., 2010). Estimation of GPP could possibly be based on the simulation of dynamic global vegetation model (Sitch et al., 2015; Le Quéré et al., 2018) and upscaling from flux tower measurements and satellite observations (Jung et al., 2019; Zeng et al., 2020). Plant functional types (PFTs) is an important factor in estimating ecosystem productivity (Lin et al., 2021; Guo et al., 2023; Yan et al., 2023).

## 6.2 Methods

### 6.2.1 Input data

#### FLUXNET 2015

The FLUXNET 2015 dataset (Pastorello et al., 2020) serves as the groundtruth for carbon fluxes in the transformer model in this study. Monthly GPP and RECO data were extracted from the dataset tier 1 of FLUXNET 2015, encompassing data from 206 sites. We filtered out records with a quality control value of less than 80% for measured and good-quality gap-fill data. Relying solely on quality control values is reported to be insufficient for obtaining qualified data due to inconsistencies in the differences between GPP, RECO, and NEE (Zeng et al., 2020; Tramontana et al., 2016). Following the approach of (Zeng et al., 2020), we

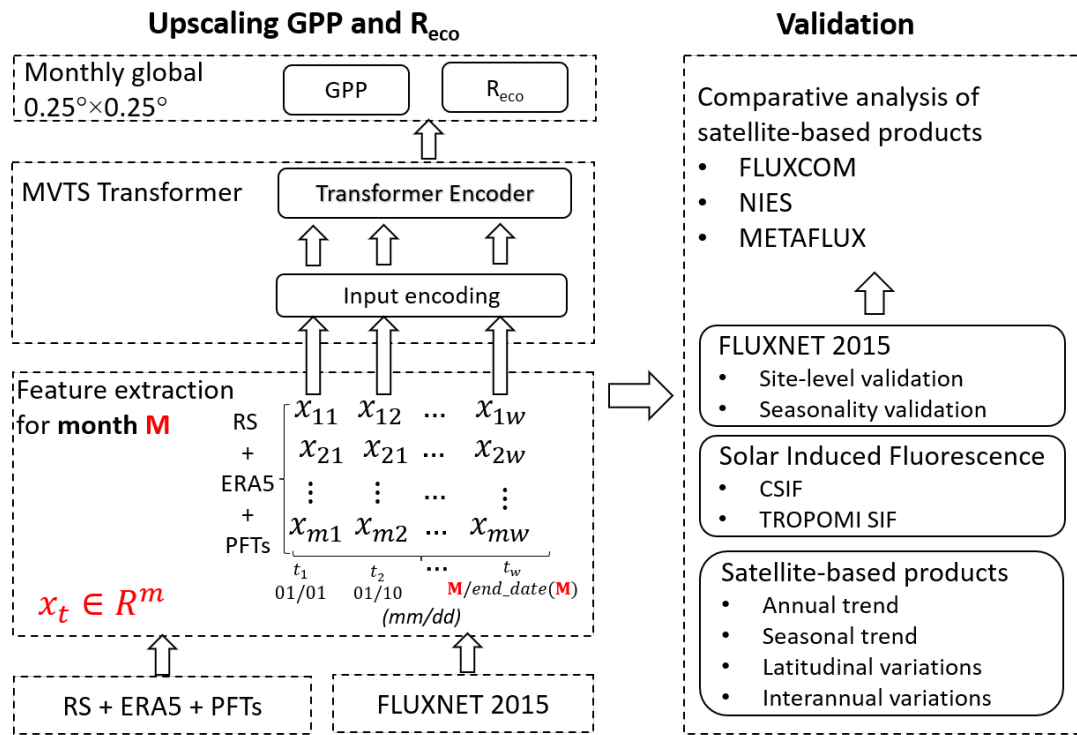


**Figure 6.1.** Schematic workflow of our FluxFormer methodology

also excluded records with an absolute difference between GPP-RECO and NEE larger than  $0.1 \text{ gC } m^{-2} d^{-1}$ .

### Remote sensing data

For the remote sensing data, we employed version 2 of the global leaf area index (LAI) and fraction of absorbed photosynthetically active radiation (FAPAR) datasets, generated using the algorithm proposed by (Verger et al., 2014). These datasets can be accessed through the Copernicus Global Land Service, providing a 1 km spatial resolution for every 10 days spanning from 1999 to 2019. The remote sensing data utilized in this study is in line with the approach presented in (Zeng et al., 2020). The latitude boundary of this dataset ranges from  $-60^\circ\text{S}$  to  $80^\circ\text{N}$ .

### Meteorological data

For meteorological data, we employed specific variables from the ERA5 reanalysis product (Hersbach et al., 2020), including 2-meter air temperature (T2M), surface short-wave (solar) radiation downwards (SSRD), vapor pressure deficit (VPD), total precipitation (TP), and evaporation (E). As VPD is not directly available in the original dataset, we estimated it using the relationship between saturated vapor pressure (SVP) and actual vapor pressure (AVP):  $VPD = SVP - AVP$ , based on 2-meter air and dewpoint temperature. The original spatial resolution of ERA5 data is  $0.25^\circ \times 0.25^\circ$  and was obtained from the Copernicus Climate Change Service (C3S) Climate Data Store (CDS).

### Plant function types

The PFTs dataset employed in this study, denoted as PFT v2.0.8 and obtained from (Harper et al., 2022), spans the period from 1992 to 2020. It provides the specific percentage cover of 14 PFTs for each pixel at a 300m resolution. The annual dataset comprises 14 layers, with pixel values at 300m resolution indicating the percentage cover (ranging from 0% to 100%) for each of the 14 PFTs. This updated PFTs dataset is considered a more accurate representation of PFT distributions as it relies on high-resolution, peer-reviewed mapping of specific vegetation classes to refine global assumptions about PFT fractions (Harper et al., 2022). Regional updates in PFT fractions are anticipated to enhance carbon fluxes estimation. The complete set of PFTs includes bare soil, built areas, water bodies, snow and ice, natural grasses, managed grasses (i.e., herbaceous cropland), broadleaved deciduous trees, broadleaved evergreen trees, needleleaved deciduous trees, needleleaved evergreen trees, broadleaved deciduous shrubs, broadleaved evergreen shrubs, needleleaved deciduous shrubs, and needle-leaved evergreen shrubs. The dataset can be accessed from the CEDA archive at <https://catalogue.ceda.ac.uk/uuid/26a0f46c95ee4c29b5c650b129aab788>.

#### 6.2.2 Multivariate Time Series Transformer Framework

Figure 6.1 illustrates the overall workflow of our FluxFormer methodology to upscale GPP and RECO from remote sensing data, and PFTs data. We utl-

ized the original Multivariate Time Series MVTS Transformer model which is transformer-based framework proposed by (Zerveas et al., 2021) which contains an input encoding layer with learnable positional encoding and a Transformer Encoder (Vaswani et al., 2017). MVTS Transformer achieved good performance on supervised and unsupervised regression task based on multivariate time series representation even with limited training samples.

In order train the MVTS Transformer, First, we extracted the remote sensing data, meteorological data and PFTs for each monthly record from FLUXNET 2015 dataset. Then the extracted data is formed to feed to the deep learning model. In particular, for a specific month  $\mathbf{M}$ , each traing sample  $\mathbf{X} \in \mathbb{R}^{w \times n}$  where  $w$  is the lengths of timeseries for month  $\mathbf{M}$   $w = 3 \times \mathbf{M}$  as we have 3 remote sensing products per month and  $m$  is the number of different variables  $m = 21$  2 remote sensing varibales (LAI and FAPAR), 5 meteorological variables (T2M, SSRD, VPD, TP, E) and 14 PFTs variables, constitutes a sequence of  $w$  feature vectors  $\mathbf{x}_t \in \mathbb{R}^m : \mathbf{X} \in \mathbb{R}^{w \times n} = [\mathbf{x}_1, \mathbf{x}_2, \dots, \mathbf{x}_w]$  is a multivariate timeseries of length  $w$  and  $m$  different variables.

### 6.2.3 Training setup

To train the model, approximately 80% of the monthly data was randomly chosen for training, while the remaining 20% was allocated for validation. Twelve models were trained over the course of 12 months. Notably, the distribution of FLUXNET 2015 sites is uneven across climate zones, particularly in the tropics and semi-arid regions, despite the highest Gross Primary Productivity (GPP) values being observed in tropical areas such as Amazonia, Central Africa, and Southeast Asia(Chen et al., 2017c). Additionally, semi-arid regions play a crucial role in influencing the global carbon cycle (Poulter et al., 2014). To address this imbalance, only the most recent data from the past three years for each site was utilized to ensure a more equitable representation of each site during the training of the transformer model. This approach resulted in a total of 4576 samples over the 12-month period. The distribution of samples for training and validation is detailed in Table 6.1.

**Table 6.1.** Number of samples for training and validation

Month	Number of samples	
	Training	Validation
January	363	68
February	377	72
March	392	77
April	385	75
May	408	88
June	372	66
July	379	66
August	365	67
September	387	68
October	406	71
November	385	75
December	357	62

#### 6.2.4 Validation

To evaluate our product’s quality, we performed a comparative analysis against other remote sensing-based products, including FLUXCOM (Jung et al., 2019), NIES (Zeng et al., 2020), and MetaFlux (Nathaniel et al., 2023). Initially, we assessed the correlation of monthly FLUXNET 2015 GPP and RECO values with the corresponding data from these products at the FLUXNET sites. Additionally, we examined the seasonality trends in our data across climate zones in comparison to FLUXNET 2015.

Subsequently, we conducted a seasonality examination using Solar-Induced Fluorescence (SIF) from CSIF (Zhang et al., 2018) (accessible at <https://fgshare.com/articles/dataset/C>) and TROPOMI SIF (Köhler et al., 2018) (retrievable from <ftp://fluo.gps.caltech.edu/data/tropomi/>)

Ultimately, we examined the interannual trends and variations, as well as the seasonal and latitudinal patterns of our outputs in comparison with FLUXCOM, NIES, and MetaFlux. To evaluate interannual trends, we computed the annual global mean Gross Primary Productivity (GPP) and Ecosystem Respiration (RECO), scaling the global average fluxes using the total global land area of 122.4

million square kilometers from (Friedl et al., 2010), as recommended by (Jung et al., 2020) to ensure consistent global area representation across all products. The annual trends and their statistical significance in GPP and RECO were indicated by the slope of the linear regression line and the corresponding p-value. For the assessment of interannual variations, we determined the Interannual Variability (IAV) at the pixel level by calculating the standard deviation divided by the mean of annual fluxes.

## 6.3 Data records

## 6.4 Technical validation

### 6.4.1 Validation with FLUXNET 2015

#### Site-level validation

We utilized the Pearson Correlation Coefficient ( $r$ ) and Root Mean Square Error (RMSE) to assess the quality of our products in comparison to FLUXNET 2015 observations. As depicted in Figures 6.3a and 6.3b, our product demonstrates the highest correlation and the lowest RMSE with FLUXNET 2015 for both Gross Primary Productivity (GPP) and Ecosystem Respiration (RECO) data ( $R = 0.894$ ,  $RMSE = 1.706$  for GPP and  $R = 0.866$ ,  $RMSE = 1.244$  for RECO). In contrast, MetaFlux shows the lowest correlation with FLUXNET 2015 ( $R = 0.652$ ,  $RMSE = 3.135$  for GPP and  $R = 0.612$ ,  $RMSE = 2.046$  for RECO). NIES and FLUXCOM also exhibit strong correlations with the ground truth data, achieving  $R/RMSE : 0.857/1.981$  (NIES),  $0.819/2.32$  (FLUXCOM) for GPP and  $R/RMSE : 0.795/1.511$  (NIES),  $0.792/1.627$  (FLUXCOM) for RECO.

#### Seasonality validation

We analyzed the seasonal trend using FLUXNET 2015 data, calculating monthly mean values across climate zones, as depicted in Figure 6.4 and Table ???. In arid regions, FluxFormer, FluxCom, and NIES exhibited high correlation ( $R > 0.9$ ) with FLUXNET for both GPP and RECO. However, MetaFlux showed lower

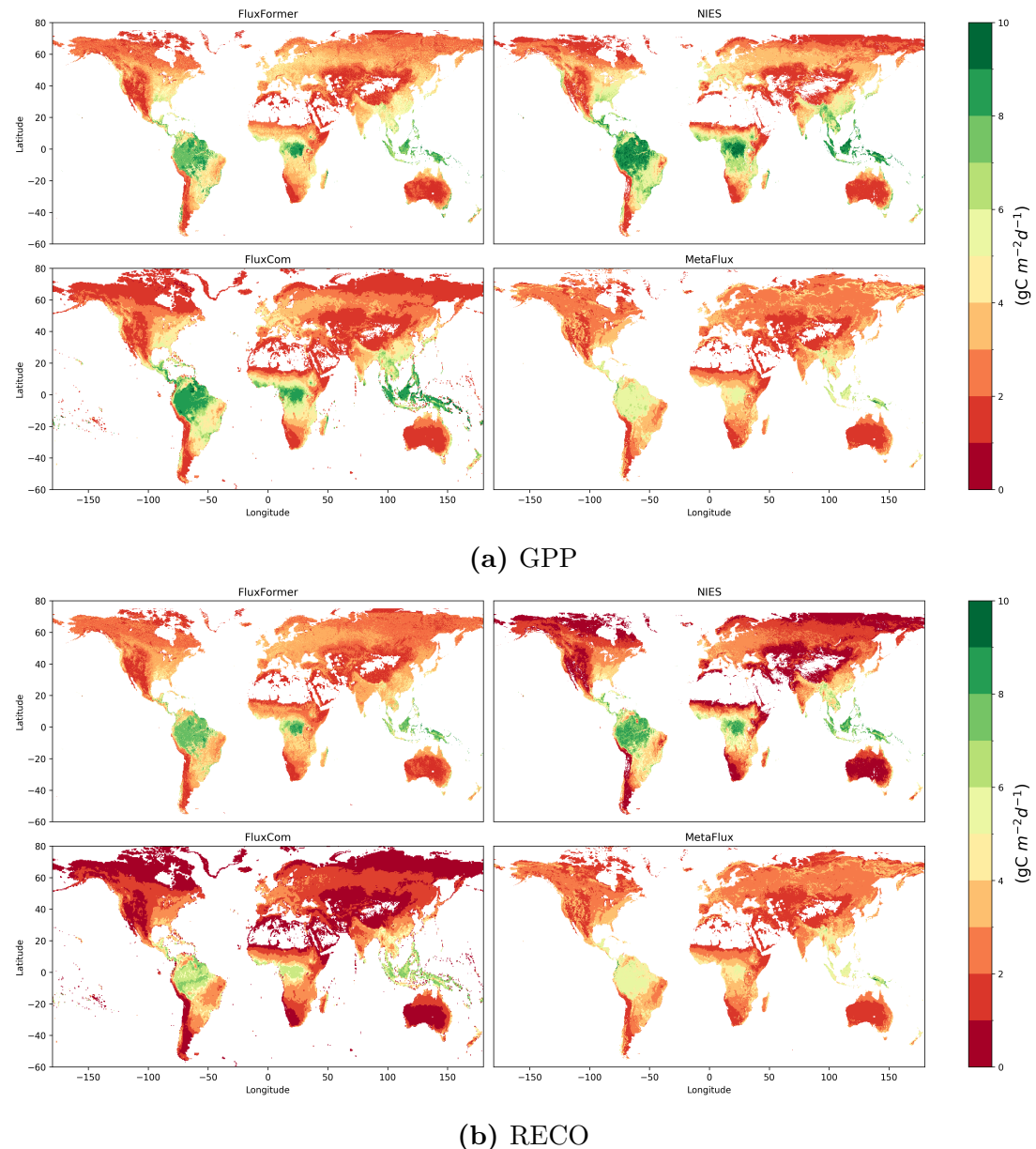


**Figure 6.2.** Validation with FLUXNET 2015: GPP (a) RECO (b)

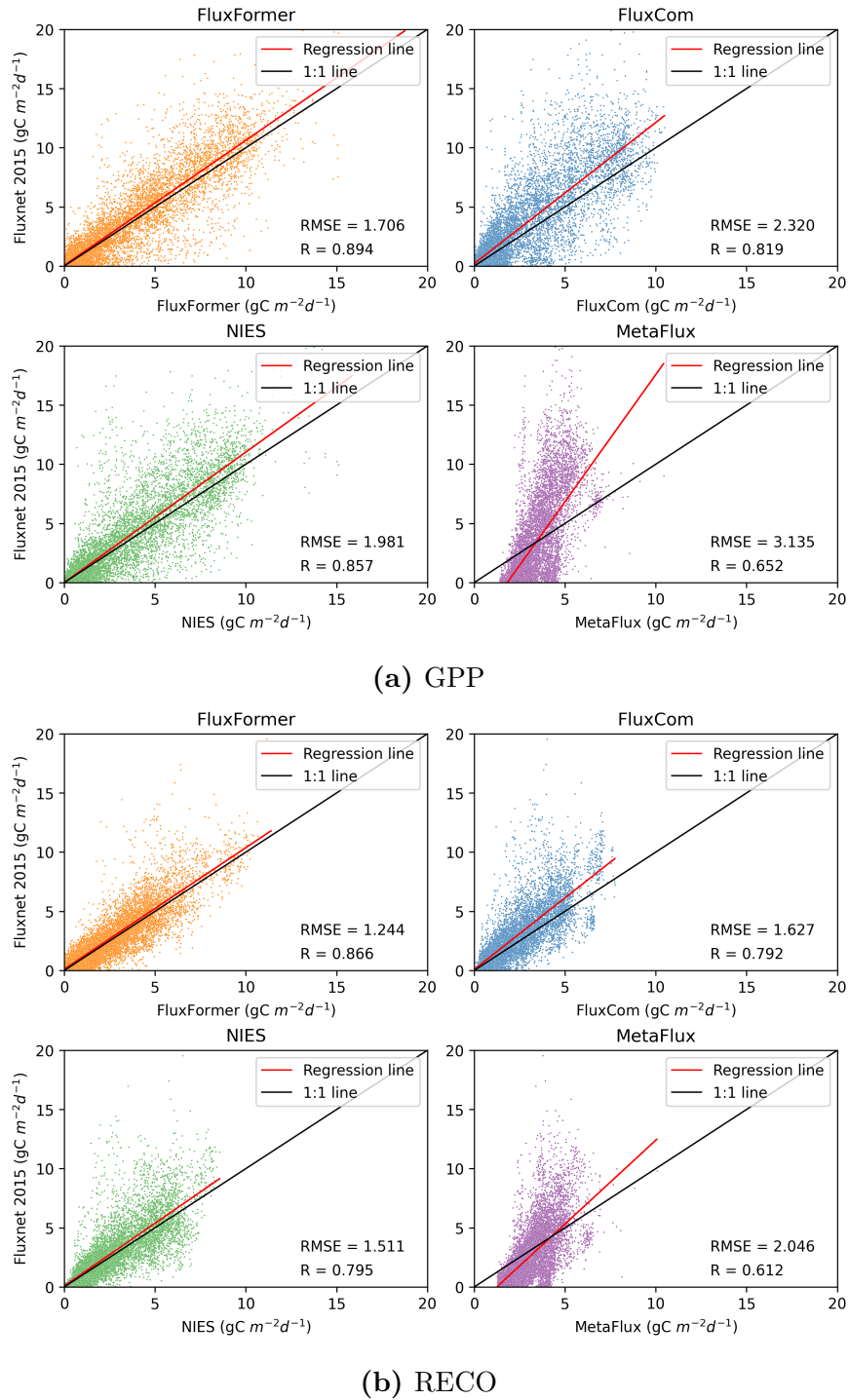


**Figure 6.3.** Validation with FLUXNET 2015: GPP (a) RECO (b)

correlation with  $R = 0.48$  for GPP and  $R = 0.66$  for RECO in arid regions. For temperate and cold regions, all satellite-based products (FluxFormer, FLUXCOM, NIES, and MetaFlux) demonstrated high correlations ( $R > 0.97$ ) with FLUXNET 2015 GPP and RECO.

**Table 6.2.** Pearson correlation of seasonal trend with FLUXNET 2015

Climate groups	FluxFormer	FluxCom	NIES	MetaFlux
GPP				
Arid	0.91	0.91	0.94	0.48
Temperate	0.99	0.99	0.97	0.97
Cold	1	0.99	1	0.99
Trop. SVN	0.99	0.99	0.94	0.97
Trop. MS	<b>0.84</b>	0.04	0.58	-0.05
Trop. RF	0.68	0.6	0.71	0.41
RECO				
Arid	0.94	0.92	0.95	0.66
Temperate	0.98	0.99	0.99	0.99
Cold	1	0.99	1	1
Trop. SVN	0.99	0.98	0.92	0.91
Trop. MS	<b>0.88</b>	0.51	0.29	0
Trop. RF	<b>0.68</b>	0.37	0.5	0.47

In the tropical region, we partitioned the area into tropical savanna (Trop. SVN), tropical monsoon (Trop. MS), and tropical rainforest (Trop. RF). In Trop. SVN, all satellite-based products displayed a high correlation with FLUXNET 2015 for both GPP and RECO. Conversely, for Trop. MS, our data exhibited the highest correlation at  $R = 0.84$ , while NIES data showed a moderate correlation ( $R = 0.58$ ). FLUXCOM and MetaFlux demonstrated no correlation with FLUXNET 2015 for GPP, with  $R < 0.1$ . Regarding RECO in Trop. SVN, our data maintained the highest correlation with the seasonal trend of the ground truth, whereas other products showed lower correlation (FLUXCOM:  $R = 0.51$ , NIES:  $R = 0.29$ ) or no correlation with the ground truth (MetaFlux:  $R = 0$ ). In the Trop. RF area, our data exhibited the second-highest correlation with GPP

seasonal trend ( $R = 0.68$ ) and the highest correlation with RECO seasonal trend ( $R = 0.68$ ).

Overall, our data demonstrates a robust correlation in arid, temperate, cold, and Trop. SVN regions, surpassing  $R > 0.9$  for both GPP and RECO. Specifically, in Trop. MS, our data exhibits the highest correlation, reaching  $R = 0.84$  for GPP and  $R = 0.88$  for RECO. In the Trop. RF region, our data exhibits the second-highest correlation with the ground truth GPP seasonal trend ( $R = 0.68$ ) and the highest correlation with the ground truth RECO seasonal trend ( $R = 0.68$ ) among the selected satellite-based products.

#### 6.4.2 Validation with SIF

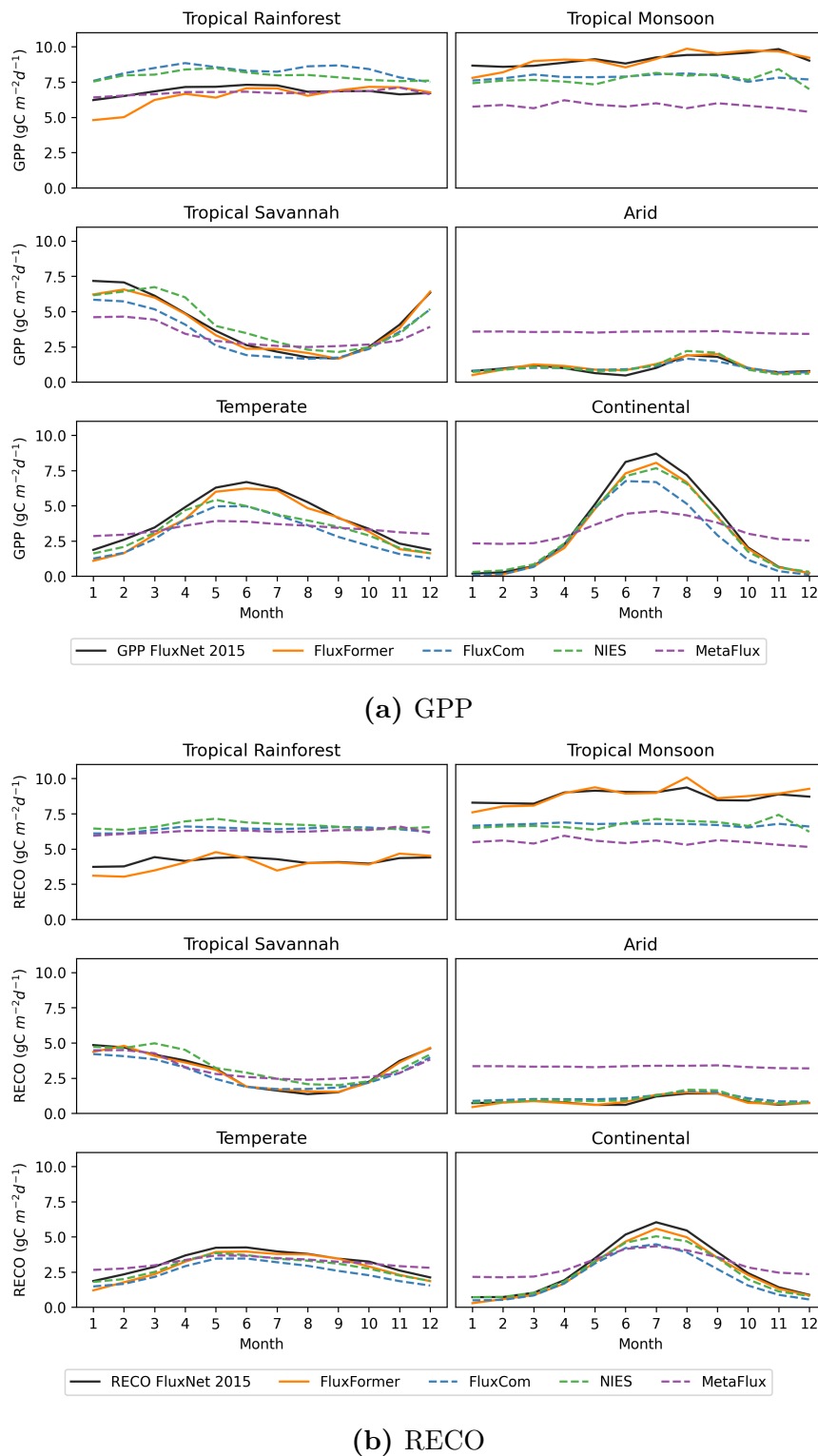
SIF serves as a reliable proxy and has seen increased usage for estimating GPP (Norton et al., 2019; Liu et al., 2020; Bai et al., 2022). To expand the seasonality validation, we incorporated independent products, namely CSIF and TROPOMI SIF. We examined the pixel-level correlation distribution of FluxFormer and selected satellite-based products with the seasonal trend of CSIF from 2000 to 2019 and TROPOMI SIF from 2018 to 2019, as TROPOMI data is available only from 2018 onwards.

The results are illustrated in Figure 6.5a and Figure 6.5b. We observed that our data exhibits lower correlation with CSIF and TROPOMI SIF in tropical regions (Central and South America, West and Central Africa, and Southeast Asia) and arid regions compared to FLUXCOM, NIES, and MetaFlux. This finding aligns with (Sanders et al., 2016), indicating weaker seasonality in these regions.

#### 6.4.3 Interannual variations between products

##### Interannual trend

The interannual trends of FluxFormer and other products (FLUXCOM, NIES, and MetaFlux) are illustrated in Figure 6.6a. We examined the global annual time series from 2001 to 2019 to analyze the trend in Gross Primary Productivity (GPP). Our dataset exhibits the highest positive trend, with a growth rate of 0.45 PgC/year. The second-highest trend is observed in the NIES global annual time series, with a growth rate of 0.32 PgC/year. MetaFlux shows a small increasing

**Figure 6.4.** Seasonality validation with FLUXNET 2015: GPP (a) RECO (b)

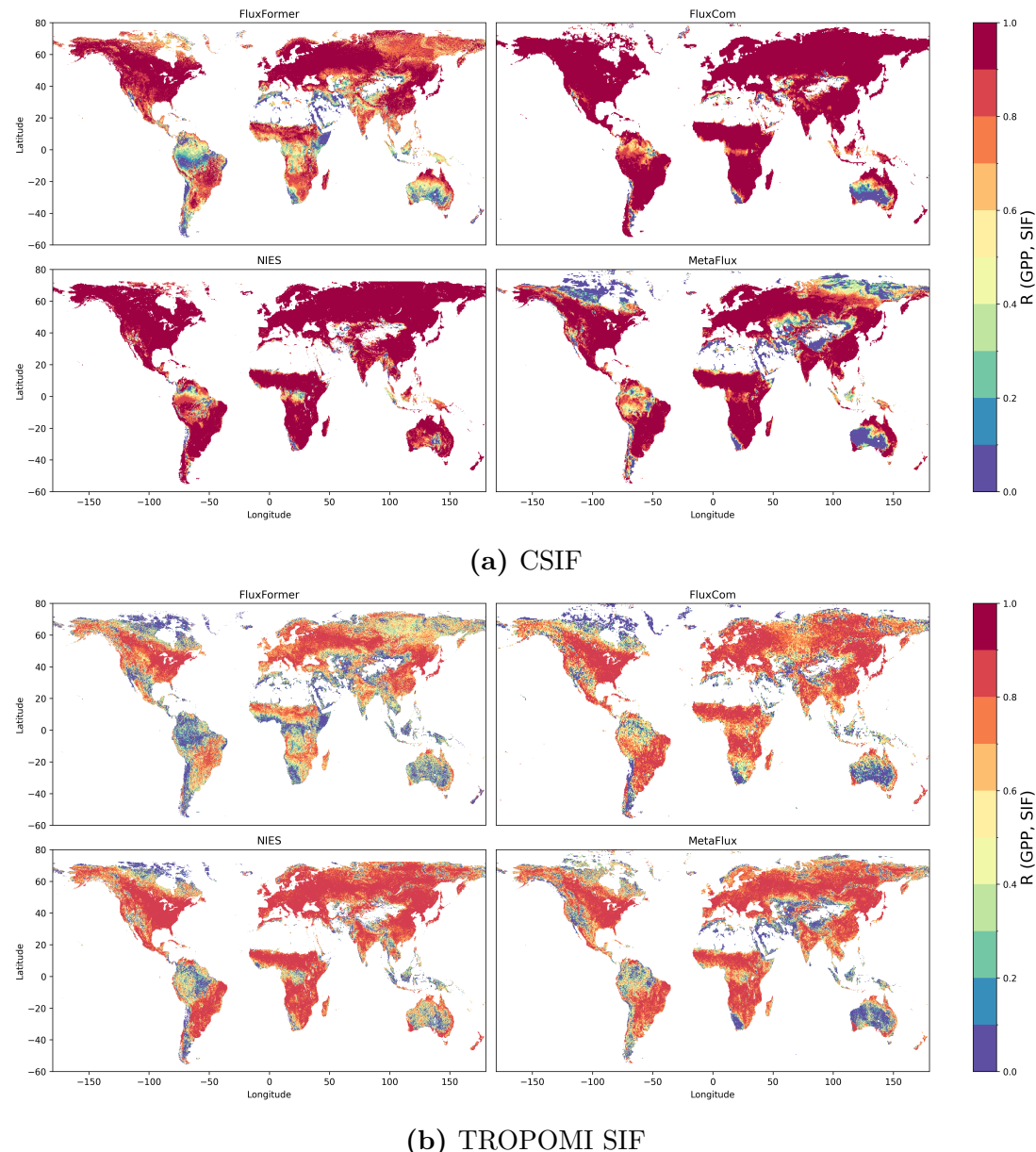


**Figure 6.5.** Validation with SIF products: CSIF (a) TROPOMI SIF (b)

trend, albeit with an insignificant p-value of 0.08. On the other hand, FLUXCOM indicates a small negative trend, with a reduction rate of 0.04 PgC per year.

Our long-term GPP trend aligns with the expected increase due to the CO<sub>2</sub> fertilization effect, anticipated to enhance the land carbon sink (Piao et al., 2020; Guo et al., 2023; Yang et al., 2022).

We also inspect the latitudinal distribution of GPP and RECO as depicted in Figure 6.6b. All four products exhibit a gradual increase in both GPP and RECO values from cold climate regions to warm and humid climates in temperate and tropical regions.

### Interannual variations

Finally, we assess the interannual variations of Gross Primary Productivity (GPP) and Ecosystem Respiration (RECO), as illustrated in Figures 6.7a and 6.7b, respectively. We observe that our data exhibits lower interannual variability than NIES in desert regions, including Australia, Central Asia, Central America, and South America. We posit that our data may be more reasonable, considering that in desert areas, GPP is expected to be extremely low (Hadley and Szarek, 1981). Additionally, our dataset demonstrates smaller interannual variability than NIES in the northern parts of Eurasia and North America.

Our dataset displays greater interannual variability compared to FLUXCOM and MetaFlux. This difference could be attributed to the use of distinct remote sensing data sources for upscaling carbon fluxes. Specifically, we employed LAI and FAPAR from SPOT/VEGETATION and PROBA-V, which aligns with the approach described in (Zeng et al., 2020). In contrast, FLUXCOM and MetaFlux utilize input remote sensing data sourced from MODIS (Jung et al., 2019; Nathaniel et al., 2023).

## 6.5 Usage notes

In this chapter, we present our work on upscaling global gross primary production and ecosystem respiration using multivariate timeseries transformer (Zerveas et al., 2021) and new plant functional types data (Harper et al., 2022). We provide the monthly global GPP and RECO data at the spatial resolution of 0.25°

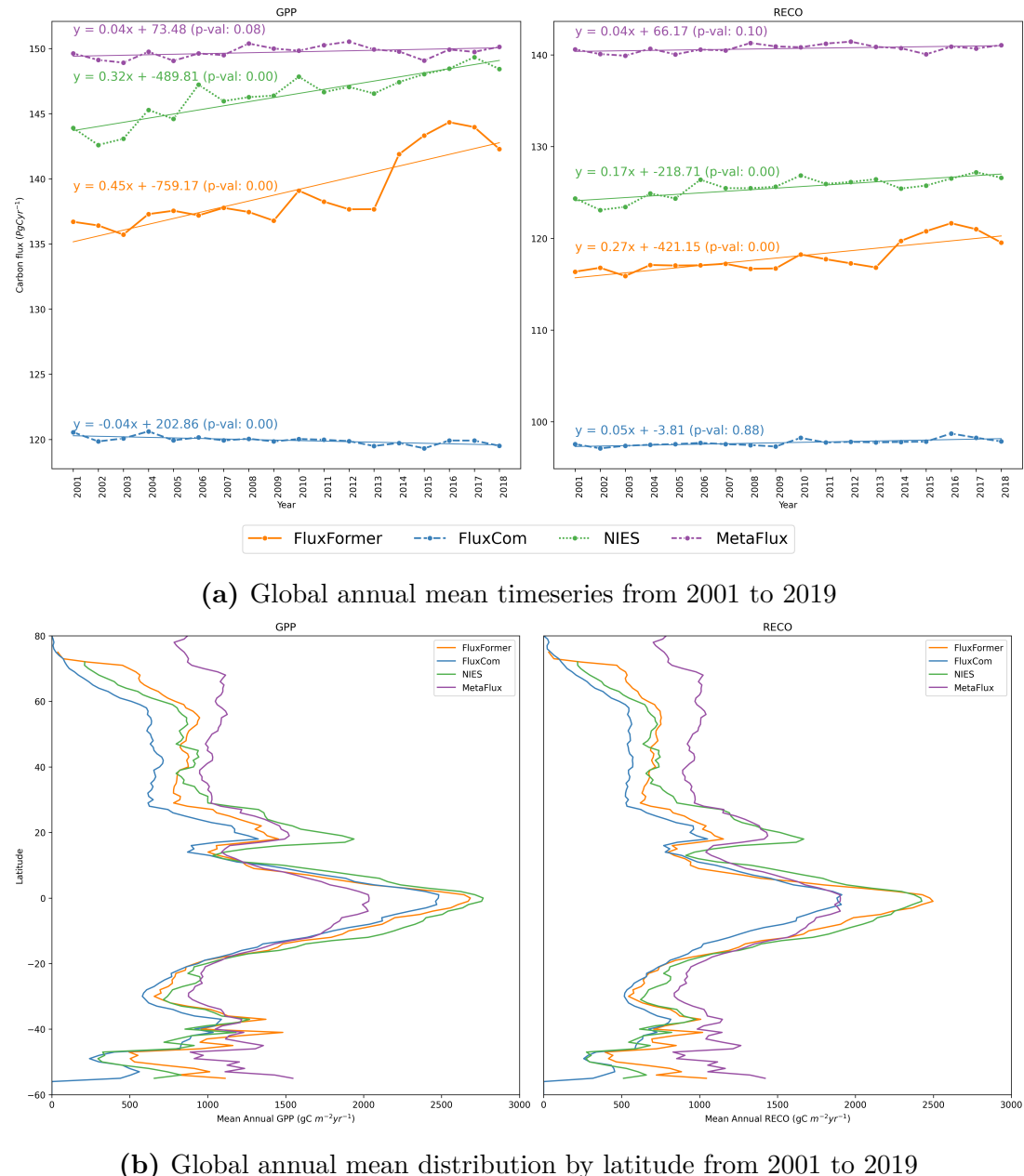


**Figure 6.6.** Seasonality validation with FLUXNET 2015: GPP (a) RECO (b)

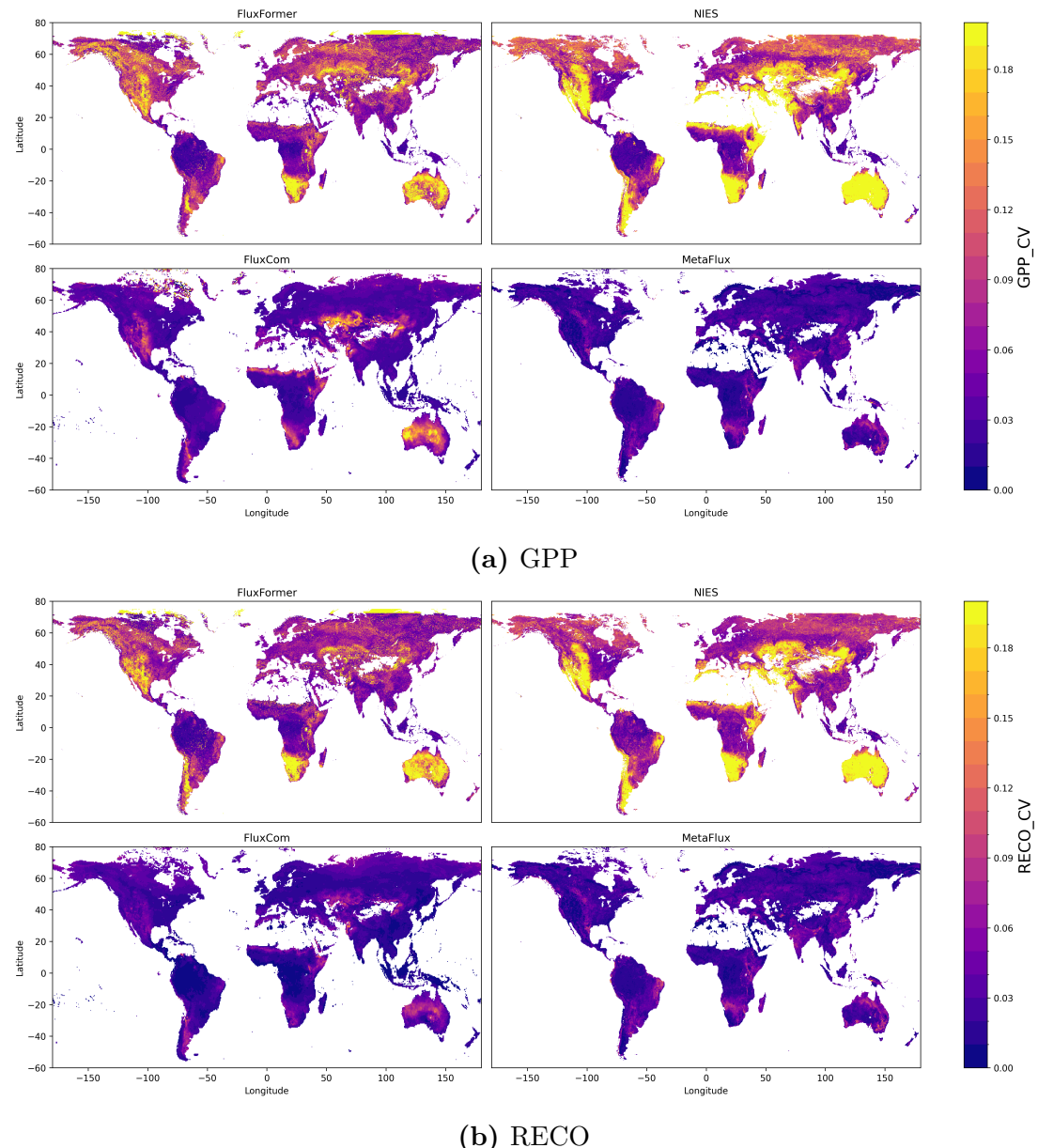


**Figure 6.7.** Interannual variations: GPP (a) RECO (b)

$\times 0.25^\circ$  from 1990 to 2019.

In this version, we have The data is permantly

# 7 CO2 monitoring platform

## 7.1 Introduction

The widely acknowledged importance of climate change across various aspects (Primack et al., 2009; Watanabe and Kume, 2009; Ogawa-Onishi and Berry, 2013; Shibuya and Croxford, 2016) is driving an accelerated momentum toward achieving Carbon Neutrality (CN) in local Japanese governments (Nakazawa et al., 2023). In both major corporations and small businesses, there is a rising demand for the measurement of greenhouse gas (GHG) emissions (Kauffmann et al., 2012). Companies are mandated to visualize their CO2 emissions and implement measures to reduce them. As of September 2023, 991 local governments, including Tokyo, Kyoto, and Yokohama, have demonstrated increased enthusiasm for this initiative by declaring their commitment to achieving net-zero carbon emissions by 2050 (Ministry of the Environment, 2023). However, to specifically implement mitigation and adaptation measures, it is necessary to perform comprehensive risk analysis and calculate detailed emissions for each sector. Furthermore, it is required to visualize this information in an easy-to-understand manner in time and space, and to explain and disclose it to various stakeholders. On the other hand, in recent years, local governments have been accelerating the integration of map information that had previously been prepared separately for each department, such as taxation, urban planning, and the environment. Integrated geographic information systems (GIS) enable cross-sectional analysis of various elements, have become one of the cornerstones of administrative digital transformation (DX), and have been introduced in 60% of all 1,741 municipalities (Nikkei, 2023).

By using WebGIS functions, local CN-related policy makers can monitor energy consumption and CO2 emissions by sector such as industry, electricity, trans-

portation, buildings and housing. By integrating it into the Geo-portal site, it will be possible to better understand the actual situation and make appropriate plans to introduce renewable energy and reduce emissions. However, for example, although national energy consumption and power generation can be determined from the regional energy supply and demand database (Tohoku University, 2023) and the electric power database (Asanobu, 2023; Planning and Regional Policy Bureau, 2023), the visualization systems for these databases have been developed separately, therefore it is difficult for policy makers to analyze comprehensively and make integrated planning.

In this chapter, we presented a case study illustrating the creation of a comprehensive tool for developing a "Supporting and Visualizing Carbon Neutrality (CN) Roadmap". This tool serves as a Digital Earth application designed to aid Japanese local governments in their pursuit of CN goals. To achieve CN, it is necessary to create cost-effective roadmaps (scenarios) based on the characteristics of each region and local government. Drafting such scenarios requires a comprehensive understanding of energy use and CO<sub>2</sub> emission patterns in each sector. The Project Drawdown (Brennan et al., 2020), a prominent initiative in this realm, represents a collaborative effort among multidisciplinary scientists, researchers, and practitioners. Its primary objective is to identify and advocate for the most impactful solutions to mitigate and potentially reverse global warming. A research group composed of researchers and policymakers has formulated and recommended various solutions for reducing greenhouse gas emissions. Despite these proposals, none of the tools have been fully integrated into the GIS platform. The integration of greenhouse gas (GHG) monitoring and zero carbon roadmap simulation into GIS platforms is currently under exploration within the Digital Earth platform (Fukui et al., 2021). Consequently, we are engaged in research and development efforts aimed at creating a Digital Earth-based platform. This platform is designed to furnish policymakers with comprehensive roadmaps, progress tracking toward goals, and other pertinent information, all within a unified GIS platform (Figure 7.1).

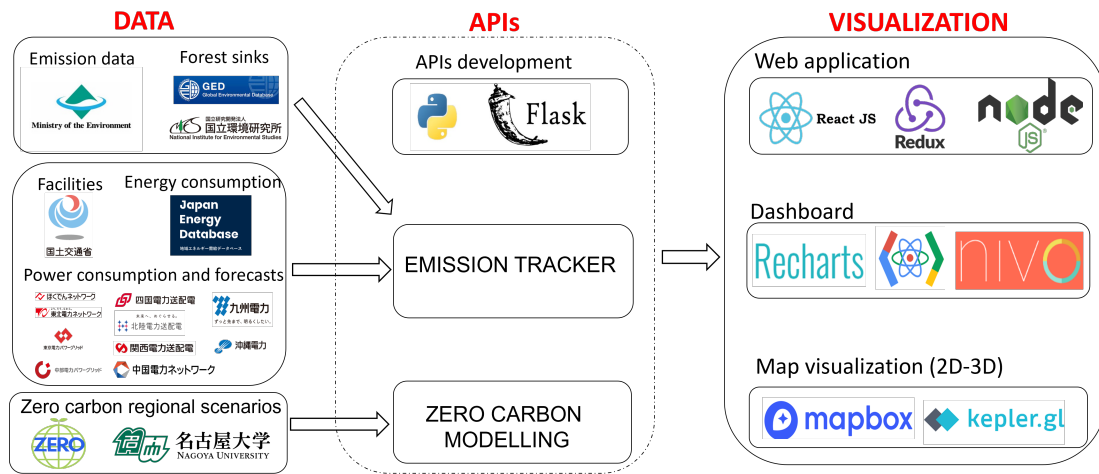


**Figure 7.1.** Platform Architecture and the technology used to develop the GIS platform

## 7.2 Method

Figure 7.1 depicts the components of the GIS platform established in this study and the core technologies utilized in its development. Initially, the process involves collecting, preprocessing, and archiving CO<sub>2</sub> emissions and related data from various sources. This data is then made available to end-users for visualization and other purposes through the development of Application Programming Interfaces (APIs). The API is designed to encompass two main functionalities: the CO<sub>2</sub> Emissions Tracker and Zero Carbon Modeling (also referred to as Drawdown). In the CO<sub>2</sub> Emissions section, users can analyze trends and patterns in CO<sub>2</sub> emissions. In the Zero Carbon Modeling (Drawdown) section, roadmaps are presented for 1,741 municipalities, each delineating effective reduction strategies for achieving carbon neutrality by 2050.

### 7.2.1 Data collection

Table 7.1 compiles information on datasets integrated into the GIS platform, along with their respective data sources. All data utilized underwent collection or preprocessing to maintain original resolution and municipality granularity.

Initially, for monitoring current greenhouse gas emissions and energy-related

**Table 7.1.** The dataset used for the GIS platform development

Dataset	Data source
CO <sub>2</sub> emissions by sector	(Ministry of the Environment, 2022)
Energy consumption statistics	(Tohoku University, 2023)
Power generation facility	(Planning and Regional Policy Bureau, 2023)
	(Hokkaido Electric Power, 2023)
	(Tohoku Electric Power, 2023)
	(Tokyo Electric Power, 2023)
	(Chubu Electric Power, 2023)
	(Hokuriku Electric Power, 2023)
Power consumption and forecasts	(Kansai Electric Power, 2023)
	(Chugoku Electric Power, 2023)
	(Shikoku Electric Power, 2023)
	(Kyushu Electric Power, 2023)
	(Okinawa Electric Power, 2023)
Gross Primary Production	
Net Ecosystem Production	(Ito, 2019)
Ecosystem respiration	
Zero carbon regional scenario	(Tsuneo et al., 2023)

issues, we employed diverse data sources. Specifically, we utilized CO<sub>2</sub> emission estimates by sectors from (Ministry of the Environment, 2022) to visualize the overall emission landscape. Additionally, we delved into industrial emissions details, using data from the Ministry of the Environment spanning 2009 to 2017. To depict forest sink capabilities, we incorporated three terrestrial carbon flux variables—gross primary production, net ecosystem production, and ecosystem respiration—from (Ito, 2019). For presenting energy-related information, energy consumption data from (Tohoku University, 2023) showcased the contrast between 2013 and 2019. The distribution of power plants across the country was illustrated using data from (Planning and Regional Policy Bureau, 2023). To offer near-real-time power consumption, we utilized data from 10 electric power companies, as outlined in Table 7.1, showcasing power consumption and forecasts.

Subsequently, we integrated data from the Zero Carbon Region Scenario Anal-

ysis Tool (Tsuneo et al., 2023), specifically designed to assist municipal staff in identifying and achieving CO<sub>2</sub> reduction targets for 2030, 2040, and 2050 to attain net-zero carbon by 2050. This information was utilized to generate corresponding maps and charts for visualization.

### 7.2.2 API development

In the development of the API for handling this data, we employed Flask (Grinberg, 2018), a lightweight web framework coded in Python, and conformed to the JSON API specification for data formatting. The API within this system is responsible for rendering dashboards related to Emission Tracker and Zero Emission Modeling (Drawdown). JSON functions as the predominant data format for the API, with all responses aligning with the specifications outlined in Table 7.2. The APIs are deployed on the cloud-based platform Heroku, and the interfaces are depicted in Figure 7.2.

**Table 7.2.** APIs specifications

End point	Parameters	Description
Base URL: <a href="https://emissionjp.herokuapp.com/ems_tracker/">https://emissionjp.herokuapp.com/ems_tracker/</a>		
GET /overall_ems/country	year: year of the emission data	Emissions at national level
GET /overall_ems/municipality	adm_code: municipality code year: year of the emission data	Emissions at municipality level in a specific year
GET /overall_ems/municipality_ts	adm_code: municipality code	Time-series emissions at municipality level.
GET /overall_ems/sector	sector_type: sector type	Emissions categorized by sectors.
GET /ee_stats/5mins	None	Near real time power usage, forecast
GET /ee_stats/energy_consumption	adm_code: municipality code	Energy consumption at municipality level.
GET /forest_sink/municipality	adm_code: municipality code	Forest variable at municipality level.
GET /industry/annual_ems	adm_code: municipality code year: year of the emission data	Industrial emission at municipality level
Base URL: <a href="https://emissionjp.herokuapp.com/zero_ems/">https://emissionjp.herokuapp.com/zero_ems/</a>		
GET /zero_ems/municipality	adm_code: municipality code	Roadmap to reduce GHG at municipality level

We present examples of two API responses, achieved through the execution of a GET request directed to two distinct endpoints: /overall\_ems/municipality for generating a map visualization and /overall\_ems/municipality\_ts for generating a line chart visualization specific to a municipality. This demonstration offers a clear and practical example of the API's functionality. Users can initiate these requests without the need for authentication.

**Listing 7.1.** A response from GET /overall\_ems/municipality

```
1  {
2      "features": [
3          {
4              "geometry": {
5                  "coordinates": [ [ ... ] ],
6                  "type": "Polygon"
7              },
8              "id": "26",
9              "properties": {
10                  "adm_code": 23100,
11                  "agriculture": 30,
12                  "building": 3435,
13                  "business": 5034,
14                  "city": "Nagoya Shi",
15                  "construction_mining": 235,
16                  "consumer_total": 8469,
17                  "freight_car": 1222,
18                  "industry_total": 3900,
19                  "manufacture": 3635,
20                  "passenger_car": 2134,
21                  "pref": "Aichi Ken",
22                  "pref_code": 23,
23                  "railway": 126,
24                  "ship": 46,
25                  "total": 16017,
26                  "transportation_total": 3528,
27                  "waste": 121
28              },
29              "type": "Feature"
30          }
31      ],
32      "type": "FeatureCollection"
33 }
```

**Listing 7.2.** A response from GET /overall\_ems/municipality\_ts

```
1  {
2      "result": [
3          {
4              "agriculture": 39,
5              "building": 2473,
6              "business": 3032,
7              "construction_mining": 311,
8              "freight_car": 1478,
9              "manufacture": 6910,
10             "passenger_car": 1840,
11             "railway": 133,
12             "ship": 36,
13             "waste": 144,
14             "year": 1990
15         },
16         ...
17         {
18             "agriculture": 30,
19             "building": 3435,
20             "business": 5034,
21             "construction_mining": 235,
22             "freight_car": 1222,
23             "manufacture": 3635,
24             "passenger_car": 2134,
25             "railway": 126,
26             "ship": 46,
27             "waste": 121,
28             "year": 2005
29         },
30     ]
31 }
```

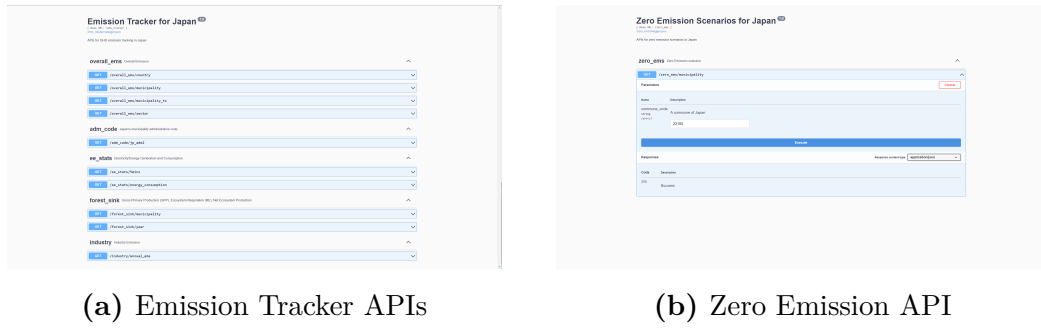


**Figure 7.2.** APIs interfaces Emission Tracker APIs (a) Zero Emission APIs (b)

### 7.2.3 Web application

The web application comprises two primary functionalities: (1) tracking greenhouse gas (GHG) emissions, referred to as the Emissions Tracker, and (2) modeling scenarios for achieving zero-carbon emissions, known as Drawdown. The objective of the GHG emission tracker is to offer a comprehensive overview of emissions and forest sinks at the municipality level. Additionally, we provide data on energy consumption to enhance end-users' understanding of the current situation. To achieve this, we have organized the GHG emission tracker into five specific tabs: Emission Overview, Forest Sinks, Energy Consumption, Electricity Statistics, and Industrial Emission. In the context of Drawdown modeling, we present simulation results that serve as a roadmap for maximizing emission reduction by 2050. To construct the interactive and informative GIS dashboard, we utilized the following technologies for platform development.

- Web Application: Node.js, ReactJS, Redux
- Interactive Charts: Rechart, React Google Charts, NIVO
- Interactive Maps: Mapbox and Kepler.gl

## 7.3 Result and discussion

### 7.3.1 Result

The summary of usage scenarios for the created GIS platform is presented below. Initially, we delve into the interface of Emission Tracker-related pages (see Figure 7.3) and the Drawdown page see Figure 7.4. Subsequently, we elaborate on other functionalities of the platform (see Figure 7.5).

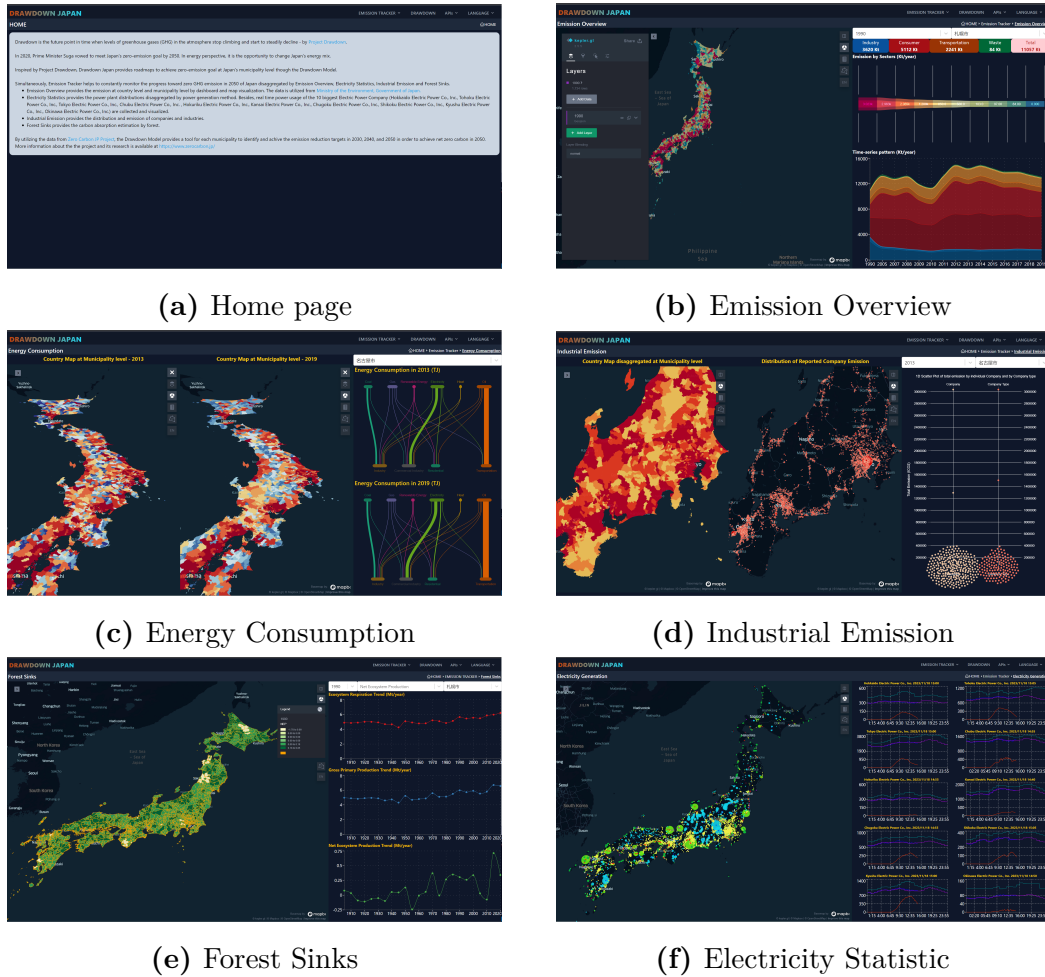


Figure 7.3. Emission Tracker interfaces

The Emission Tracker, depicted in Figure 7.3, furnishes details about emissions and energy consumption at the municipal level. The visualized data is categorized

into tabs, encompassing an overview of emissions, energy consumption, electricity statistics, industrial emissions, and forest sinks. Users can conveniently access pertinent information by choosing a municipality of interest through a dropdown selection box or a map.

[Emission Overview]: The content of this webpage, illustrated in Figure 7.3b, presents emission data categorized by sector (Industry, Consumer, Transportation, Waste) spanning from 1990 to 2019. This section offers insights into the current status and temporal fluctuations in emissions.

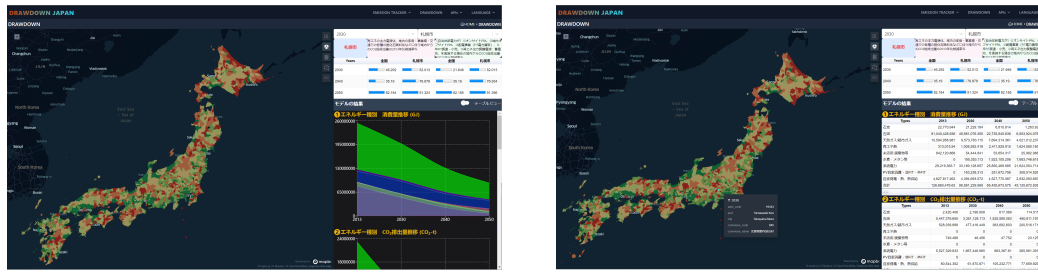
[Energy Consumption]: The contents of this webpage, depicted in Figure 7.3c, provide in-depth details regarding energy consumption at the municipal level in Japan spanning from 2013 to 2019. The data is compiled based on energy type and sector, aiding in decision-making processes related to efficient energy use and savings.

[Electricity Statistics]: The content on this webpage, illustrated in Figure 7.3f, presents details on the spatial distribution of power plants in Japan, categorized by plant type. The information encompasses data from major domestic power companies, covering electricity usage, usage forecasts, and supply forecasts. This data is sourced through the provided APIs from 10 major electric power companies, each representing a region in Japan (Table 7.1 contains the API endpoints for the data utilized in the platform, sourced from 10 electric companies).

[Industrial Emissions]: The content on this webpage, depicted in Figure 7.3d, provides a thorough perspective on industrial sector emissions. It displays emission profiles for each company (specific operators under the Energy Saving Act with a total energy usage of 1500kl/year or more) from 2009 to 2017. The webpage utilizes reporting information in accordance with the Energy Saving Act to consolidate municipal-level emissions, offering insights into the nationwide distribution of industrial emissions. Additionally, it ranks companies based on annual emissions within municipalities, serving as reference information for monitoring industrial sector emissions.

[Forest Sinks]: The content on this webpage, illustrated in Figure 7.3e, exhibits three crucial variables associated with forest absorption: Gross Primary Production (GPP), Net Ecosystem Production (NEP), and ecosystem respiration. These variables, obtained from simulations conducted by the global model Vegetation

Integrative Simulator for Trace Gas (VISIT), depict a long-term trend spanning from 1901 to 2020. The data is presented at the municipal level, offering a rolling display of 5 years of data.



(a) Map and charts

(b) Map and tables

**Figure 7.4.** Drawdown tab interfaces

The "Drawdown" page (refer to Figure 7.4) outlines a comprehensive roadmap for achieving a reduction in CO<sub>2</sub> emissions by 2050 at the municipal level in Japan. Specifically, it provides a roadmap with diverse parameters, including trends in energy consumption, trends in CO<sub>2</sub> emissions by energy type, trends in CO<sub>2</sub> emissions by sector/industry, regional renewable energy electricity, regional production-consumption planning, and the ratio of total regional production-consumption to total energy usage. Additionally, it visually represents the total CO<sub>2</sub> emissions reduction by 2030, 2040, and 2050. This enables municipal officials not only to scrutinize their municipality's data intricately but also to enhance their understanding through personalized data comparisons with other similar municipalities.



(a) 3D buildings visualization

(b) Japanese text

**Figure 7.5.** Additional platform interfaces

In addition to the functionalities outlined earlier, as we incorporated Kepler.gl for map visualization, which enables end-users to customize the map personally with options such as 2D/3D views, color schemes, tooltips, and various settings (refer to Figure 7.5). Users also have the capability to upload their own data for visualization and comparison with the provided data. Furthermore, we offer content in both English and Japanese to facilitate easy comprehension of information on our GIS platform.

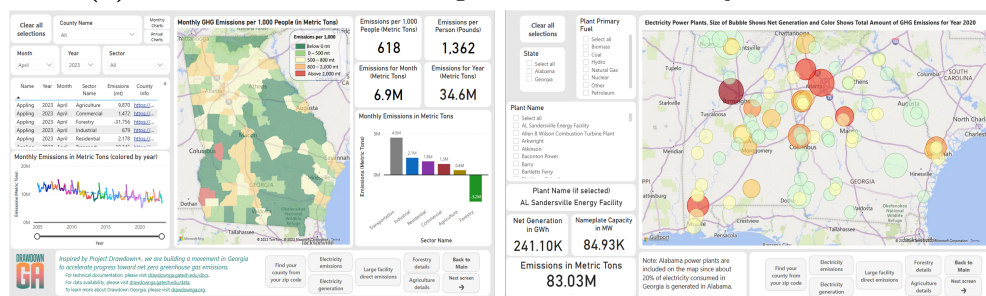
The GIS platform is accessible at <http://de14.digitalasia.chubu.ac.jp/>.

### 7.3.2 Discussion

When comparing this GIS platform to existing platforms like Project Drawdown (refer to Figure 7.6a) and Drawdown Georgia (Brown et al., 2022, 2021) (refer to Figure 7.6b), the interface design may differ slightly, but the commonality lies in charts and maps being fundamental components.



(a) The Drawdown modelling interface of the Project Drawdown



(b) The GHG Tracker interface of the Drawdown Georgia project

**Figure 7.6.** The interfaces of the Project Drawdown (a) and the GHG Tracker (Drawdown Georgia) (b)

The key distinction between this GIS platform and these existing platforms

is that this platform has become an integrated Geo-portal, utilizing GIS for all components from emission tracking to drawdown modelling. This integration allows for a comprehensive representation of emission data and simultaneously provides a simulated roadmap, setting it apart from other platforms.

In the future, we plan to enhance the user interface based on user experience feedback and incorporate a global perspective into the system development.

# 8 Conclusion

  Lorem ipsum dolor sit amet, consectetur adipisicing elit, sed do eiusmod tempor incididunt ut labore et dolore magna aliqua. Ut enim ad minim veniam, quis nostrud exercitation ullamco laboris nisi ut aliquip ex ea commodo consequat. Duis aute irure dolor in reprehenderit in voluptate velit esse cillum dolore eu fugiat nulla pariatur. Excepteur sint occaecat cupidatat non proident, sunt in culpa qui officia deserunt mollit anim id est laborum.

# Acknowledgements

Thank you, and thank you.

# Bibliography

- Hajime Akimoto and Hiroshi Tanimoto. Rethinking of the adverse effects of nox-control on the reduction of methane and tropospheric ozone—challenges toward a denitrified society. *Atmospheric Environment*, 277:119033, 2022.
- Kitamoto Asanobu. Electrical japan, 2023. URL <http://agora.ex.nii.ac.jp/earthquake/201103-eastjapan/energy/electrical-japan/>.
- Jia Bai, Helin Zhang, Rui Sun, Xing Li, Jingfeng Xiao, and Yan Wang. Estimation of global gpp from gome-2 and oco-2 sif by considering the dynamic variations of gpp-sif relationship. *Agricultural and Forest Meteorology*, 326:109180, 2022.
- Jérôme Barré, Hervé Petetin, Augustin Colette, Marc Guevara, Vincent-Henri Peuch, Laurence Rouil, Richard Engelen, Antje Inness, Johannes Flemming, Carlos Pérez García-Pando, et al. Estimating lockdown-induced european no<sub>2</sub> changes using satellite and surface observations and air quality models. *Atmospheric chemistry and physics*, 21(9):7373–7394, 2021.
- M Bauwens, S Compernolle, T Stavrakou, J-F Müller, J Van Gent, H Eskes, Pieterneel Felicitas Levelt, R Van Der A, JP Veefkind, J Vlietinck, et al. Impact of coronavirus outbreak on no2 pollution assessed using tropomi and omi observations. *Geophysical Research Letters*, 47(11):e2020GL087978, 2020.
- Christian Beer, Markus Reichstein, Enrico Tomelleri, Philippe Ciais, Martin Jung, Nuno Carvalhais, Christian Rödenbeck, M Altaf Arain, Dennis Baldocchi, Gordon B Bonan, et al. Terrestrial gross carbon dioxide uptake: global distribution and covariation with climate. *Science*, 329(5993):834–838, 2010.
- Rachel A Brennan, Julio Urbina, Jose F Oliden, and Juan Martín Rodríguez. Project drawdown. In *2020 ASEE Virtual Annual Conference Content Access*, 2020.

- Marilyn A Brown, Blair Beasley, Fikret Atalay, Kim M Cobb, Puneet Dwivedi, Jeffrey Hubbs, David M Iwaniek, Sudhagar Mani, Daniel Matisoff, Jacqueline E Mohan, et al. Translating a global emission-reduction framework for subnational climate action: A case study from the state of georgia. *Environmental Management*, 67(2):205–227, 2021.
- Marilyn A Brown, Ranal Tudawe, and Hamilton Steimer. Carbon drawdown potential of utility-scale solar in the united states: Evidence from the state of georgia. *Renewable and Sustainable Energy Reviews*, 161:112318, 2022.
- Mingkui Cao, Stewart Marshall, and Keith Gregson. Global carbon exchange and methane emissions from natural wetlands: Application of a process-based model. *Journal of Geophysical Research: Atmospheres*, 101(D9):14399–14414, 1996.
- Liang-Chieh Chen, George Papandreou, Iasonas Kokkinos, Kevin Murphy, and Alan L Yuille. Deeplab: Semantic image segmentation with deep convolutional nets, atrous convolution, and fully connected crfs. *IEEE transactions on pattern analysis and machine intelligence*, 40(4):834–848, 2017a.
- Liang-Chieh Chen, George Papandreou, Florian Schroff, and Hartwig Adam. Rethinking atrous convolution for semantic image segmentation. *arXiv preprint arXiv:1706.05587*, 2017b.
- Min Chen, Rashid Rafique, Ghassem R Asrar, Ben Bond-Lamberty, Philippe Ciais, Fang Zhao, Christopher PO Reyer, Sebastian Ostberg, Jinfeng Chang, Akihiko Ito, et al. Regional contribution to variability and trends of global gross primary productivity. *Environmental Research Letters*, 12(10):105005, 2017c.
- Inc Chubu Electric Power. Electricity forecast for chubu area, 2023. URL <https://powergrid.chuden.co.jp/>.
- Inc Chugoku Electric Power. Electricity forecast for chugoku area, 2023. URL <https://www.energia.co.jp/nw/>.

Özgün Çiçek, Ahmed Abdulkadir, Soeren S Lienkamp, Thomas Brox, and Olaf Ronneberger. 3d u-net: learning dense volumetric segmentation from sparse annotation. In *Medical Image Computing and Computer-Assisted Intervention—MICCAI 2016: 19th International Conference, Athens, Greece, October 17–21, 2016, Proceedings, Part II 19*, pages 424–432. Springer, 2016.

Matthew J Cooper, Randall V Martin, Melanie S Hammer, Pieter Nel F Levelt, Pepijn Veefkind, Lok N Lamsal, Nickolay A Krotkov, Jeffrey R Brook, and Chris A McLinden. Global fine-scale changes in ambient no<sub>2</sub> during covid-19 lockdowns. *Nature*, 601(7893):380–387, 2022.

Ivan Csiszar, Wilfrid Schroeder, Louis Giglio, Evan Ellicott, Krishna P Vadrevu, Christopher O Justice, and Brad Wind. Active fires from the suomi npp visible infrared imaging radiometer suite: Product status and first evaluation results. *Journal of Geophysical Research: Atmospheres*, 119(2):803–816, 2014.

Alessandro Damiani, Hitoshi Irie, Dmitry A Belikov, Shuei Kaizuka, Hossain Mohammed Syedul Hoque, and Raul R Cordero. Peculiar covid-19 effects in the greater tokyo area revealed by spatiotemporal variabilities of tropospheric gases and light-absorbing aerosols. *Atmospheric Chemistry and Physics*, 22(18):12705–12726, 2022.

Bohdan Danylyshyn. The peculiarities of economic crisis due to covid-19 pandemic in a developing country: case of ukraine. *Problems and Perspectives in Management*, 18(2):13–22, 2020.

André de Palma, Shaghayegh Vosough, and Feixiong Liao. An overview of effects of covid-19 on mobility and lifestyle: 18 months since the outbreak. *Transportation Research Part A: Policy and Practice*, 159:372–397, 2022.

Carmelia Mariana Dragomir, Daniel-Eduard Constantin, Mirela Voiculescu, Lucian Puiu Georgescu, Alexis Merlaud, and Michel Van Roozendael. Modeling results of atmospheric dispersion of no<sub>2</sub> in an urban area using meti-lis and comparison with coincident mobile doas measurements. *Atmospheric Pollution Research*, 6(3):503–510, 2015.

V. Dumitru, P. Inga, M. Danu, S. Andreas, K. Ievgen, and Y Viktoriaia. Covid-19 impact on air quality in ukraine and the republic of moldova, 2020. URL <https://www.undp.org/ukraine/publications/covid-19-impact-air-quality-ukraine-and-republic-moldova>.

Bryan N Duncan, Yasuko Yoshida, Jennifer R Olson, Sanford Sillman, Randall V Martin, Lok Lamsal, Yongtao Hu, Kenneth E Pickering, Christian Retscher, Dale J Allen, et al. Application of omi observations to a space-based indicator of nox and voc controls on surface ozone formation. *Atmospheric Environment*, 44(18):2213–2223, 2010.

Liang Feng, Paul I Palmer, Robert J Parker, Mark F Lunt, and Hartmut Bösch. Methane emissions are predominantly responsible for record-breaking atmospheric methane growth rates in 2020 and 2021. *Atmospheric Chemistry and Physics*, 23(8):4863–4880, 2023.

Mark A Friedl, Damien Sulla-Menashe, Bin Tan, Annemarie Schneider, Navin Ramankutty, Adam Sibley, and Xiaoman Huang. Modis collection 5 global land cover: Algorithm refinements and characterization of new datasets. *Remote sensing of Environment*, 114(1):168–182, 2010.

Jerome H Friedman. Greedy function approximation: a gradient boosting machine. *Annals of statistics*, pages 1189–1232, 2001.

Hiromichi Fukui, Duc Chuc Man, and Anh Phan. Digital earth: A platform for the sdgs and green transformation at the global and local level, employing essential sdgs variables. *Big Earth Data*, 5(4):476–496, 2021.

Pall Oskar Gislason, Jon Atli Benediktsson, and Johannes R Sveinsson. Random forests for land cover classification. *Pattern recognition letters*, 27(4):294–300, 2006.

Noel Gorelick, Matt Hancher, Mike Dixon, Simon Ilyushchenko, David Thau, and Rebecca Moore. Google earth engine: Planetary-scale geospatial analysis for everyone. *Remote sensing of Environment*, 202:18–27, 2017.

- Stuart K Grange and David C Carslaw. Using meteorological normalisation to detect interventions in air quality time series. *Science of the Total Environment*, 653:578–588, 2019.
- Stuart K Grange, David C Carslaw, Alastair C Lewis, Eirini Boleti, and Christoph Hueglin. Random forest meteorological normalisation models for swiss pm 10 trend analysis. *Atmospheric Chemistry and Physics*, 18(9):6223–6239, 2018.
- Stuart K Grange, James D Lee, Will S Drysdale, Alastair C Lewis, Christoph Hueglin, Lukas Emmenegger, and David C Carslaw. Covid-19 lockdowns highlight a risk of increasing ozone pollution in european urban areas. *Atmospheric Chemistry and Physics*, 21(5):4169–4185, 2021.
- Miguel Grinberg. *Flask web development: developing web applications with python*. " O'Reilly Media, Inc.", 2018.
- Renjie Guo, Tiexi Chen, Xin Chen, Wenping Yuan, Shuci Liu, Bin He, Lin Li, Shengzhen Wang, Ting Hu, Qingyun Yan, et al. Estimating global gpp from the plant functional type perspective using a machine learning approach. *Journal of Geophysical Research: Biogeosciences*, page e2022JG007100, 2023.
- Neil F Hadley and Stan R Szarek. Productivity of desert ecosystems. *BioScience*, 31(10):747–753, 1981.
- Ghassan B Hamra, Francine Laden, Aaron J Cohen, Ole Raaschou-Nielsen, Michael Brauer, and Dana Loomis. Lung cancer and exposure to nitrogen dioxide and traffic: a systematic review and meta-analysis. *Environmental health perspectives*, 123(11):1107–1112, 2015.
- Kandice L Harper, Céline Lamarche, Andrew Hartley, Philippe Peylin, Catherine Ottlé, Vladislav Bastrikov, Rodrigo San Martín, Sylvia I Bohnenstengel, Grit Kirches, Martin Boettcher, et al. A 29-year time series of annual 300-metre resolution plant functional type maps for climate models. *Earth System Science Data Discussions*, 2022:1–37, 2022.
- Hans Hersbach, Bill Bell, Paul Berrisford, Gionata Biavati, András Horányi, Joaquín Muñoz Sabater, Julien Nicolas, Carole Peubey, Raluca Radu, Iryna

- Rozum, et al. Era5 hourly data on single levels from 1979 to present. *Copernicus climate change service (c3s) climate data store (cds)*, 10(10.24381), 2018.
- Hans Hersbach, Bill Bell, Paul Berrisford, Shoji Hirahara, András Horányi, Joaquín Muñoz-Sabater, Julien Nicolas, Carole Peubey, Raluca Radu, Dinand Schepers, et al. The era5 global reanalysis. *Quarterly Journal of the Royal Meteorological Society*, 146(730):1999–2049, 2020.
- Inc Hokkaido Electric Power. Electricity forecast for hokkaido area, 2023. URL <https://denkiyoho.hepco.co.jp/>.
- Inc Hokuriku Electric Power. Electricity forecast for hokuriku area, 2023. URL <https://www.rikuden.co.jp/nw/denki-yoho/>.
- Hitoshi Irie, Daichi Yonekawa, Alessandro Damiani, Hossain Mohammed Syedul Hoque, Kengo Sudo, and Syuichi Itahashi. Continuous multi-component maxdoas observations for the planetary boundary layer ozone variation analysis at chiba and tsukuba, japan, from 2013 to 2019. *Progress in Earth and Planetary Science*, 8(1):31, 2021.
- Syuichi Itahashi, Yuki Yamamura, Zhe Wang, and Itsushi Uno. Returning long-range pm2. 5 transport into the leeward of east asia in 2021 after chinese economic recovery from the covid-19 pandemic. *Scientific Reports*, 12(1):5539, 2022.
- Akihiko Ito. Disequilibrium of terrestrial ecosystem co 2 budget caused by disturbance-induced emissions and non-co 2 carbon export flows: a global model assessment. *Earth System Dynamics*, 10(4):685–709, 2019.
- Akihiko Ito. Output data of greenhouse gas budget and carbon cycle simulated by the visit terrestrial ecosystem model, ver.2021.1\_ch4wetl\_cao, 2021a. URL 10.17595/20210521.001.
- Akihiko Ito. Output data of greenhouse gas budget and carbon cycle simulated by the visit terrestrial ecosystem model, ver.2021.1\_ch4wetl\_wh, 2021b. URL 10.17595/20210521.001.

- Akihiko Ito and Kazuhito Ichii. Terrestrial ecosystem model studies and their contributions to asiaflux. *Journal of Agricultural Meteorology*, 77(1):81–95, 2021.
- Akihiko Ito, Yasunori Tohjima, Takuya Saito, Taku Umezawa, Tomohiro Hajima, Ryuichi Hirata, Makoto Saito, and Yukio Terao. Methane budget of east asia, 1990–2015: A bottom-up evaluation. *Science of the total environment*, 676: 40–52, 2019.
- Xiaomeng Jin, Arlene Fiore, K Folkert Boersma, Isabelle De Smedt, and Lukas Valin. Inferring changes in summertime surface ozone–no x–voc chemistry over us urban areas from two decades of satellite and ground-based observations. *Environmental science & technology*, 54(11):6518–6529, 2020.
- Martin Jung, Sujan Koirala, Ulrich Weber, Kazuhito Ichii, Fabian Gans, Gustau Camps-Valls, Dario Papale, Christopher Schwalm, Gianluca Tramontana, and Markus Reichstein. The fluxcom ensemble of global land-atmosphere energy fluxes. *Scientific data*, 6(1):74, 2019.
- Martin Jung, Christopher Schwalm, Mirco Migliavacca, Sophia Walther, Gustau Camps-Valls, Sujan Koirala, Peter Anthoni, Simon Besnard, Paul Bodesheim, Nuno Carvalhais, et al. Scaling carbon fluxes from eddy covariance sites to globe: synthesis and evaluation of the fluxcom approach. 2020.
- L. Júlia, M. Dylan, R. Danielle, and B Adrian. Nearly 3 million people have left ukraine, foreshadowing a massive humanitarian crisis, 2022. URL <https://www.washingtonpost.com/world/2022/02/27/ukraine-refugees-photos-videos/>.
- Inc Kansai Electric Power. Electricity forecast for kansai area, 2023. URL <https://www.kansai-td.co.jp/>.
- Céline Kauffmann, Cristina Tébar Less, and Dorothee Teichmann. Corporate greenhouse gas emission reporting: A stocktaking of government schemes. 2012.
- Guolin Ke, Qi Meng, Thomas Finley, Taifeng Wang, Wei Chen, Weidong Ma, Qiwei Ye, and Tie-Yan Liu. Lightgbm: A highly efficient gradient boosting decision tree. *Advances in neural information processing systems*, 30, 2017.

- Christine M Kendrick, Peter Koonce, and Linda A George. Diurnal and seasonal variations of no, no<sub>2</sub> and pm<sub>2.5</sub> mass as a function of traffic volumes alongside an urban arterial. *Atmospheric Environment*, 122:133–141, 2015.
- Diederik P Kingma and Jimmy Ba. Adam: A method for stochastic optimization. *arXiv preprint arXiv:1412.6980*, 2014.
- Philipp Köhler, Christian Frankenberg, Troy S Magney, Luis Guanter, Joanna Joiner, and Jochen Landgraf. Global retrievals of solar-induced chlorophyll fluorescence with tropomi: First results and intersensor comparison to oco-2. *Geophysical Research Letters*, 45(19):10–456, 2018.
- Inc Kyushu Electric Power. Electricity forecast for kyushu area, 2023. URL [https://www.kyuden.co.jp/td\\_power\\_usages/pc.html](https://www.kyuden.co.jp/td_power_usages/pc.html).
- Laura Elena Cué La Rosa, Camile Sothe, Raul Queiroz Feitosa, Cláudia Maria de Almeida, Marcos Benedito Schimalski, and Dário Augusto Borges Oliveira. Multi-task fully convolutional network for tree species mapping in dense forests using small training hyperspectral data. *ISPRS Journal of Photogrammetry and Remote Sensing*, 179:35–49, 2021.
- M. Lauri and G. Rosa. Health impacts of coal power plant emissions in ukraine, 2021. URL <https://energyandcleanair.org/publication/health-impacts-of-coal-power-plant-emissions-in-ukraine/>.
- Corinne Le Quéré, Robbie M Andrew, Pierre Friedlingstein, Stephen Sitch, Judith Hauck, Julia Pongratz, Penelope Pickers, Jan Ivar Korsbakken, Glen P Peters, Josep G Canadell, et al. Global carbon budget 2018. *Earth System Science Data Discussions*, 2018:1–3, 2018.
- Juheon Lee, Xiaohao Cai, Jan Lellmann, Michele Dalponte, Yadvinder Malhi, Nathalie Butt, Mike Morecroft, Carola-Bibiane Schönlieb, and David A Coomes. Individual tree species classification from airborne multisensor imagery using robust pca. *IEEE Journal of Selected Topics in Applied Earth Observations and Remote Sensing*, 9(6):2554–2567, 2016.

Shangrong Lin, Jing Li, Qinhuo Liu, Beniamino Gioli, Eugenie Paul-Limoges, Nina Buchmann, Mana Gharun, Lukas Hörtnagl, Lenka Foltynová, Jiří Dušek, et al. Improved global estimations of gross primary productivity of natural vegetation types by incorporating plant functional type. *International Journal of Applied Earth Observation and Geoinformation*, 100:102328, 2021.

Xinjie Liu, Liangyun Liu, Jiaochan Hu, Jian Guo, and Shanshan Du. Improving the potential of red sif for estimating gpp by downscaling from the canopy level to the photosystem level. *Agricultural and Forest Meteorology*, 281:107846, 2020.

Yiming Liu, Tao Wang, Trissevgeni Stavrakou, Nellie Elguindi, Thierno Doumbia, Claire Granier, Idir Bouarar, Benjamin Gaubert, and Guy P Brasseur. Diverse response of surface ozone to covid-19 lockdown in china. *Science of the Total Environment*, 789:147739, 2021.

Virginie Marécal, V-H Peuch, Camilla Andersson, Stefan Andersson, Joaquim Arteta, Matthias Beekmann, Anna Benedictow, Robert Bergström, Bertrand Bessagnet, Alberto Cansado, et al. A regional air quality forecasting system over europe: the macc-ii daily ensemble production. *Geoscientific Model Development*, 8(9):2777–2813, 2015.

Randall V Martin, Arlene M Fiore, and Aaron Van Donkelaar. Space-based diagnosis of surface ozone sensitivity to anthropogenic emissions. *Geophysical Research Letters*, 31(6), 2004.

Japan Ministry of the Environment. Current estimation of co2 emissions by sector, 2022. URL [https://www.env.go.jp/policy/local\\_keikaku/tools/suikei2.html](https://www.env.go.jp/policy/local_keikaku/tools/suikei2.html).

Japan Ministry of the Environment. 2050 zero carbon cities in japan, 2023. URL [https://www.env.go.jp/en/earth/cc/2050\\_zero\\_carbon\\_cities\\_in\\_japan.html](https://www.env.go.jp/en/earth/cc/2050_zero_carbon_cities_in_japan.html).

Kazuyuki Miyazaki and Kevin Bowman. Predictability of fossil fuel co2 from air quality emissions. *Nature communications*, 14(1):1604, 2023.

- Kazuyuki Miyazaki, Kevin Bowman, Takashi Sekiya, Masayuki Takigawa, Jessica L Neu, Kengo Sudo, Greg Osterman, and Henk Eskes. Global tropospheric ozone responses to reduced no x emissions linked to the covid-19 worldwide lockdowns. *Science Advances*, 7(24):eabf7460, 2021.
- Takashi Nakazawa, Keiichi Satoh, Gregory Trencher, Tomoyuki Tatsumi, and Koichi Hasegawa. Net-zero carbon declarations by japanese local governments: What caused the domino-like diffusion? *Review of Policy Research*, 2023.
- Juan Nathaniel, Jiangong Liu, and Pierre Gentine. Metaflux: Meta-learning global carbon fluxes from sparse spatiotemporal observations. *Scientific Data*, 10(1):440, 2023.
- G. Nichita and M Ana. War in ukraine one year on, nowhere safe, 2023. URL <https://acleddata.com/2023/03/01/war-in-ukraine-one-year-on-nowhere-safe/>.
- Nikkei. Map information, the cornerstone of administrative dx: Introduction of “integrated” 1099 local governments, 2023. URL <https://www.nikkei.com/article/DGXZQ0CC314EI0R30C23A1000000/>.
- Alexander J Norton, Peter J Rayner, Ernest N Koffi, Marko Scholze, Jeremy D Silver, and Ying-Ping Wang. Estimating global gross primary productivity using chlorophyll fluorescence and a data assimilation system with the bethy-scope model. *Biogeosciences*, 16(15):3069–3093, 2019.
- Yuko Ogawa-Onishi and Pam M Berry. Ecological impacts of climate change in japan: The importance of integrating local and international publications. *Biological Conservation*, 157:361–371, 2013.
- Inc Okinawa Electric Power. Electricity forecast for okinawa area, 2023. URL <https://www.okiden.co.jp/denki2/>.
- Carlos Ordóñez, Jose M Garrido-Perez, and Ricardo García-Herrera. Early spring near-surface ozone in europe during the covid-19 shutdown: Meteorological effects outweigh emission changes. *Science of the total environment*, 747:141322, 2020.

- Yude Pan, Richard A Birdsey, Jingyun Fang, Richard Houghton, Pekka E Kauppi, Werner A Kurz, Oliver L Phillips, Anatoly Shvidenko, Simon L Lewis, Josep G Canadell, et al. A large and persistent carbon sink in the world's forests. *Science*, 333(6045):988–993, 2011.
- Gilberto Pastorello, Carlo Trotta, Eleonora Canfora, Housen Chu, Danielle Christianson, You-Wei Cheah, Cristina Poindexter, Jiquan Chen, Abdelrahman El-bashandy, Marty Humphrey, et al. The fluxnet2015 dataset and the oneflux processing pipeline for eddy covariance data. *Scientific data*, 7(1):225, 2020.
- Shushi Peng, Xin Lin, Rona L Thompson, Yi Xi, Gang Liu, Didier Hauglustaine, Xin Lan, Benjamin Poulter, Michel Ramonet, Marielle Saunois, et al. Wetland emission and atmospheric sink changes explain methane growth in 2020. *Nature*, 612(7940):477–482, 2022.
- Paulo Pereira, Wenwu Zhao, Lyudmyla Symochko, Miguel Inacio, Igor Bogunovic, and Damia Barcelo. The russia-ukrainian armed conflict impact will push back the sustainable development goals, 2022.
- Hervé Petetin, Dene Bowdalo, Albert Soret, Marc Guevara, Oriol Jorba, Kim Serradell, and Carlos Pérez García-Pando. Meteorology-normalized impact of the covid-19 lockdown upon no<sub>2</sub> pollution in spain. *Atmospheric Chemistry and Physics*, 20(18):11119–11141, 2020.
- Shilong Piao, Xuhui Wang, Taejin Park, Chi Chen, XU Lian, Yue He, Jarle W Bjerke, Anping Chen, Philippe Ciais, Hans Tømmervik, et al. Characteristics, drivers and feedbacks of global greening. *Nature Reviews Earth & Environment*, 1(1):14–27, 2020.
- National Land Information Division National Spatial Planning and MLIT of Japan Regional Policy Bureau. Power generation facility, 2023. URL <https://nlftp.mlit.go.jp/ksj/gml/datalist/KsjTmplt-P03.html>.
- Benjamin Poulter, David Frank, Philippe Ciais, Ranga B Myneni, Niels Andela, Jian Bi, Gregoire Broquet, Josep G Canadell, Frederic Chevallier, Yi Y Liu, et al. Contribution of semi-arid ecosystems to interannual variability of the global carbon cycle. *Nature*, 509(7502):600–603, 2014.

- Richard B Primack, Hiroyoshi Higuchi, and Abraham J Miller-Rushing. The impact of climate change on cherry trees and other species in japan. *Biological Conservation*, 142(9):1943–1949, 2009.
- Zhen Qu, Daniel J Jacob, Yuzhong Zhang, Lu Shen, Daniel J Varon, Xiao Lu, Tia Scarpelli, Anthony Bloom, John Worden, and Robert J Parker. Attribution of the 2020 surge in atmospheric methane by inverse analysis of gosat observations. *Environmental Research Letters*, 17(9):094003, 2022.
- Clionadh Raleigh, rew Linke, Håvard Hegre, and Joakim Karlsen. Introducing acled: An armed conflict location and event dataset. *Journal of peace research*, 47(5):651–660, 2010.
- Jie Ren, Fangfang Guo, and Shaodong Xie. Diagnosing ozone–no x–voc sensitivity and revealing causes of ozone increases in china based on 2013–2021 satellite retrievals. *Atmospheric Chemistry and Physics*, 22(22):15035–15047, 2022.
- Caleb Robinson, Kolya Malkin, Nebojsa Jojic, Huijun Chen, Rongjun Qin, Changlin Xiao, Michael Schmitt, Pedram Ghamisi, Ronny Hänsch, and Naoto Yokoya. Global land-cover mapping with weak supervision: Outcome of the 2020 ieee grss data fusion contest. *IEEE Journal of Selected Topics in Applied Earth Observations and Remote Sensing*, 14:3185–3199, 2021.
- Olaf Ronneberger, Philipp Fischer, and Thomas Brox. U-net: Convolutional networks for biomedical image segmentation. In *Medical Image Computing and Computer-Assisted Intervention–MICCAI 2015: 18th International Conference, Munich, Germany, October 5–9, 2015, Proceedings, Part III* 18, pages 234–241. Springer, 2015.
- Abram FJ Sanders, Willem W Verstraeten, Maurits L Kooreman, Thomas C Van Leth, Jason Beringer, and Joanna Joiner. Spaceborne sun-induced vegetation fluorescence time series from 2007 to 2015 evaluated with australian flux tower measurements. *Remote Sensing*, 8(11):895, 2016.
- Mykhailo Savenets. Air pollution in ukraine: a view from the sentinel-5p satellite. *JOURNAL OF THE HUNGARIAN METEOROLOGICAL SERVICE*, 125(2):271–290, 2021.

- Felix Schiefer, Teja Kattenborn, Annett Frick, Julian Frey, Peter Schall, Barbara Koch, and Sebastian Schmidlein. Mapping forest tree species in high resolution uav-based rgb-imagery by means of convolutional neural networks. *ISPRS Journal of Photogrammetry and Remote Sensing*, 170:205–215, 2020.
- Quirin Schiermeier. Why pollution is falling in some cities—but not others. *Nature*, 580(7803):313, 2020.
- Jason R Schroeder, James H Crawford, Alan Fried, James Walega, Andrew Weinheimer, Armin Wisthaler, Markus Müller, Tomas Mikoviny, Gao Chen, Michael Shook, et al. New insights into the column ch<sub>2</sub>o/no<sub>2</sub> ratio as an indicator of near-surface ozone sensitivity. *Journal of Geophysical Research: Atmospheres*, 122(16):8885–8907, 2017.
- Wilfrid Schroeder, Patricia Oliva, Louis Giglio, and Ivan A Csiszar. The new viirs 375 m active fire detection data product: Algorithm description and initial assessment. *Remote Sensing of Environment*, 143:85–96, 2014.
- Andrii Shelestov, Hanna Yailymova, Bohdan Yailymov, and Nataliia Kussul. Air quality estimation in ukraine using sdg 11.6. 2 indicator assessment. *Remote Sensing*, 13(23):4769, 2021.
- Zongbo Shi, Congbo Song, Bowen Liu, Gongda Lu, Jingsha Xu, Tuan Van Vu, Robert JR Elliott, Weijun Li, William J Bloss, and Roy M Harrison. Abrupt but smaller than expected changes in surface air quality attributable to covid-19 lockdowns. *Science advances*, 7(3):eabd6696, 2021.
- Toshihiko Shibuya and Ben Croxford. The effect of climate change on office building energy consumption in japan. *Energy and Buildings*, 117:149–159, 2016.
- Inc Shikoku Electric Power. Electricity forecast for shikoku area, 2023. URL <https://www.yonden.co.jp/nw/denkiyoho/>.
- Stephen Sitch, Pierre Friedlingstein, Nicolas Gruber, Steve D Jones, Guillermo Murray-Tortarolo, Anders Ahlström, Scott C Doney, H Graven, Christoph Heinze, Chris Huntingford, et al. Recent trends and drivers of regional sources and sinks of carbon dioxide. *Biogeosciences*, 12(3):653–679, 2015.

- Amir H Souri, Matthew S Johnson, Glenn M Wolfe, James H Crawford, Alan Fried, Armin Wisthaler, William H Brune, Donald R Blake, Andrew J Weinheimer, Tijl Verhoelst, et al. Characterization of errors in satellite-based hcho/no<sub>2</sub> tropospheric column ratios with respect to chemistry, column-to-pbl translation, spatial representation, and retrieval uncertainties. *Atmospheric Chemistry and Physics*, 23(3):1963–1986, 2023.
- David S Stevenson, Richard G Derwent, Oliver Wild, and William J Collins. Covid-19 lockdown emission reductions have the potential to explain over half of the coincident increase in global atmospheric methane. *Atmospheric Chemistry and Physics*, 22(21):14243–14252, 2022.
- T.F. Stocker, G.-K. Plattner D. Qin, M. Tignor, S.K. Allen, J. Boschung, A. Nauels, Y. Xia, V. Bex, and P.M. Midgley. Ipcc, 2013: Climate change 2013: The physical science basis. contribution of working group i to the fifth assessment report of the intergovernmental panel on climate changes. Technical report, Cambridge University Press, Cambridge, United Kingdom and New York, NY, USA, 2013.
- Akira Tani and Tomoki MOCHIZUKI. Exchanges of volatile organic compounds between terrestrial ecosystems and the atmosphere. *Journal of Agricultural Meteorology*, 77(1):66–80, 2021.
- Inc Tohoku Electric Power. Electricity forecast for tohoku area, 2023. URL <https://setsuden.nw.tohoku-epco.co.jp/>.
- Toshihiko Nakata Laboratory Tohoku University. Regional energy supply and demand database (version 2.6), 2023. URL <https://energy-sustainability.jp>.
- Inc Tokyo Electric Power. Electricity forecast for tokyo area, 2023. URL <https://www.tepco.co.jp/forecast/>.
- Gianluca Tramontana, Martin Jung, Christopher R Schwalm, Kazuhito Ichii, Gustau Camps-Valls, Botond Ráduly, Markus Reichstein, M Altaf Arain, Alessandro Cescatti, Gerard Kiely, et al. Predicting carbon dioxide and energy

- fluxes across global fluxnet sites with regression algorithms. *Biogeosciences*, 13(14):4291–4313, 2016.
- Takeuchi Tsuneo, Takano Masao, Tanikawa Hiroki, and Sugiyama Noriko. Zero carbon regional scenario analysis tool provided in excel file format, 2023. URL <https://zerocarbon.jp/>.
- Alexander J Turner, Christian Frankenberg, and Eric A Kort. Interpreting contemporary trends in atmospheric methane. *Proceedings of the National Academy of Sciences*, 116(8):2805–2813, 2019.
- Jos Van Geffen, Henk Eskes, Steven Compernolle, Gaia Pinardi, Tijl Verhoelst, Jean-Christopher Lambert, Maarten Sneep, Mark Ter Linden, Antje Ludewig, K Folkert Boersma, et al. Sentinel-5p tropomi no 2 retrieval: impact of version v2. 2 improvements and comparisons with omi and ground-based data. *Atmospheric Measurement Techniques*, 15(7):2037–2060, 2022.
- Ashish Vaswani, Noam Shazeer, Niki Parmar, Jakob Uszkoreit, Llion Jones, Aidan N Gomez, Łukasz Kaiser, and Illia Polosukhin. Attention is all you need. *Advances in neural information processing systems*, 30, 2017.
- Aleixandre Verger, Frédéric Baret, and Marie Weiss. Near real-time vegetation monitoring at global scale. *IEEE Journal of Selected Topics in Applied Earth Observations and Remote Sensing*, 7(8):3473–3481, 2014.
- Julie Wallace and Pavlos Kanaroglou. The effect of temperature inversions on ground-level nitrogen dioxide (no2) and fine particulate matter (pm2. 5) using temperature profiles from the atmospheric infrared sounder (airs). *Science of the Total Environment*, 407(18):5085–5095, 2009.
- Bernadette P Walter and Martin Heimann. A process-based, climate-sensitive model to derive methane emissions from natural wetlands: Application to five wetland sites, sensitivity to model parameters, and climate. *Global Biogeochemical Cycles*, 14(3):745–765, 2000.
- Chi Wang, Qingyun Wu, Markus Weimer, and Erkang Zhu. Flaml: A fast and lightweight automl library. *Proceedings of Machine Learning and Systems*, 3:434–447, 2021.

- Tsugihiro Watanabe and Takashi Kume. A general adaptation strategy for climate change impacts on paddy cultivation: special reference to the Japanese context. *Paddy and Water Environment*, 7:313–320, 2009.
- Pu Yan, Nianpeng He, Kailiang Yu, Li Xu, and Koenraad Van Meerbeek. Integrating multiple plant functional traits to predict ecosystem productivity. *Communications Biology*, 6(1):239, 2023.
- Ruqi Yang, Jun Wang, Ning Zeng, Stephen Sitch, Wenhan Tang, Matthew Joseph McGrath, Qixiang Cai, Di Liu, Danica Lombardozzi, Hanqin Tian, et al. Divergent historical gpp trends among state-of-the-art multi-model simulations and satellite-based products. *Earth System Dynamics*, 13(2):833–849, 2022.
- Rasa Zalakeviciute, Danilo Mejia, Hermel Alvarez, Xavier Bermeo, Santiago Bonilla-Bedoya, Yves Rybarczyk, and Brian Lamb. War impact on air quality in Ukraine. *Sustainability*, 14(21):13832, 2022.
- Jiye Zeng, Tsuneo Matsunaga, Zheng-Hong Tan, Nobuko Saigusa, Tomoko Shirai, Yanhong Tang, Shushi Peng, and Yoko Fukuda. Global terrestrial carbon fluxes of 1999–2019 estimated by upscaling eddy covariance data with a random forest. *Scientific data*, 7(1):313, 2020.
- George Zerveas, Srideepika Jayaraman, Dhaval Patel, Anuradha Bhamidipaty, and Carsten Eickhoff. A transformer-based framework for multivariate time series representation learning. In *Proceedings of the 27th ACM SIGKDD conference on knowledge discovery & data mining*, pages 2114–2124, 2021.
- Yao Zhang, Joanna Joiner, Seyed Hamed Aleomohammad, Sha Zhou, and Pierre Gentine. A global spatially contiguous solar-induced fluorescence (csif) dataset using neural networks. *Biogeosciences*, 15(19):5779–5800, 2018.
- Zhen Zhang, Benjamin Poulter, Andrew F Feldman, Qing Ying, Philippe Ciais, Shushi Peng, and Xin Li. Recent intensification of wetland methane feedback. *Nature Climate Change*, 13(5):430–433, 2023.
- Maria A Zoran, Roxana S Savastru, Dan M Savastru, and Marina N Tautan. Peculiar weather patterns effects on air pollution and covid-19 spread in tokyo metropolis. *Environmental Research*, 228:115907, 2023.